Monolithic fiber guides for multi-channel fiber Fabry–Pérot cavity integration

Jana Blechmann

Masterarbeit in Physik
angefertigt im Institut für Angewandte Physik

vorgelegt der
Mathematisch-Naturwissenschaftlichen Fakultät
der
Rheinischen Friedrich-Wilhelms-Universität
Bonn

October 2026

I hereby declare that this thesis was formulated by myself and that no sources or tools other than those cited were used.

Bonn, ...
Date Signature

1. Gutachter: Prof. Dr. Sebastian Hofferberth
2. Gutachter: Prof. Dr. Stefan Linden

Statement on Digital Tools and AI Assistance

In the preparation of this thesis, digital tools—including AI-based assistance—were used for supporting tasks such as language polishing, code writing for data plotting and analysis, code debugging, code documentation and document formatting. All results were verified independently by the author.

Task / Purpose	**Tools Used**	**Role of the Tools**
Writing and Language Polishing	ChatGPT	Grammar correction, spelling checks, sentence restructuring for clarity, and text structuring.
LaTeX Formatting and Typesetting	ChatGPT, Zotero, TeX Live	Assistance with LaTeX syntax, table formatting, and reference styling.
Coding and Debugging	ChatGPT	Code writing for data plotting and analysis, code documentation, code debugging. Numerical models and simulations were designed and verified by the author.
Literature Search	ChatGPT, Google Scholar	Literature search.
Plotting of Data	MATLAB, Matplotlib (Python)	Plotting of data and simulations.
Designing of Models	Autodesk Inventor, Describe	Modeling of Printjobs/ Workshop instructions.

Contents

Statement on Digital Tools and AI Assistance iii

1 Introduction 1

2 Fiber Fabry–Pérot Cavity System 4
- 2.1 Fundamentals of Fabry–Pérot Cavities . . . 4
  - 2.1.1 Fiber-Based Fabry–Pérot Cavities . . . 6
- 2.2 Alignment of Fiber Fabry–Pérot Cavities . . . 6
  - 2.2.1 Impedance Matching . . . 7
  - 2.2.2 Optical Mode Matching . . . 8
  - 2.2.3 Polarization Splitting . . . 9

3 Fiber Mirror Fabrication & Characterization 10
- 3.1 Fiber Mirror Fabrication . . . 10
  - 3.1.1 Fiber Preparation . . . 10
  - 3.1.2 CO_2 Laser Ablation . . . 11
  - 3.1.3 Mirror Coating . . . 13
- 3.2 Fiber Cavity Characterization Setups . . . 13
  - 3.2.1 Fiber–Plane Mirror Cavity Characterization Setup . . . 14
  - 3.2.2 Fiber–Fiber Cavity Characterization Setup . . . 17

4 Design and Fabrication of the Assembly Platforms 19
- 4.1 Grooved Ceramic Holders . . . 20
  - 4.1.1 Holder Concepts and Design . . . 20
  - 4.1.2 Groove Fabrication . . . 22
  - 4.1.3 Additional Clamping . . . 25
- 4.2 3D-Printed Ferrules . . . 27
  - 4.2.1 Ferrule Concept and Design . . . 27
  - 4.2.2 Ferrule Fabrication . . . 29
  - 4.2.3 Post-Processing . . . 33
  - 4.2.4 Ferrule Shrinkage During Post-Processing . . . 35
- 4.3 Comparison of the Assembly Concepts . . . 36

5 Evaluation of the Assembly Platforms **38**
5.1 Alignment Characterization Methods . . . 38
5.1.1 Rotating Pillar Method . . . 39
5.1.2 Knife-Edge Method . . . 43
5.2 Grooved Ceramic Holder Assembly . . . 48
5.3 3D-Printed Ferrule Assembly . . . 50
5.3.1 Assessment of the Four-Channel Crossed Ferrule . . . 50
5.3.2 Assessment of the Three-Channel T-Shaped Ferrule . . . 52
5.3.3 Image-Based Assessment of the Three-Channel T-Shaped Ferrule . . . 53
5.4 Comparison of the Alignment Performance of the Assembly Platforms . . . 55

6 Implementation of Crossed Fiber Assemblies **59**
6.1 Three-Channel Pump–Cavity Assembly . . . 59
6.2 Crossed-Cavity Concept . . . 60
6.3 Crossed-Cavity Implementation . . . 63
6.4 Cavity-Mode Alignment Characterization . . . 64
6.4.1 Pinhole Method . . . 64
6.5 Current State and Remaining Challenges . . . 73

7 Conclusion and Outlook **74**
7.1 Outlook . . . 75

Bibliography **77**

A Appendix **83**
A.1 Optical Mode Matching . . . 83
A.2 Mirror Coating . . . 86
A.3 Additional Printing Images . . . 87
A.4 Engineering Drawings . . . 90
A.5 Beam Profile Centering . . . 94
A.6 Crossed FFPCs for CQED . . . 94

Acknowledgements **96**

CHAPTER 1

Introduction

Many experiments in atomic physics, quantum optics, and optical spectroscopy rely on the controlled spatial overlap of multiple optical fields within a common interaction region. Depending on the application, these fields may consist of freely propagating beams addressing different optical transitions or of resonant cavity modes used to enhance light–matter interactions. In either case, their relative spatial alignment directly affects the strength of the underlying interaction [1, 2].

Optical cavities provide a particularly strong spatial definition of the optical field while simultaneously enhancing the interaction of light with matter. In cavity quantum electrodynamics, this allows single atoms or other emitters to interact strongly with confined optical modes and enables applications such as state detection, photon generation, quantum gates, and quantum-network nodes [3–6]. More complex experiments can require several optical modes to overlap within the same interaction region. Crossed optical cavities have, for example, been used to couple a single atom to two distinct cavity modes, enabling the realization of a heralded quantum-network node [7].

Fiber Fabry–Pérot cavities (FFPCs) provide a compact implementation of optical resonators. FFPCs are typically formed by two concave, reflective mirrors fabricated directly on fiber end facets [8–10]. Their small mode volume, high achievable finesse, and direct fiber coupling make them attractive for experiments requiring strong light–matter interaction [9, 11, 12]. FFPCs have been used in cavity-QED experiments, cavity optomechanics, single-photon applications, and optical spectroscopy [13–19]. Compared with bulk-optical cavities, the fiber-based geometry with direct optical access through the fibers additionally offers the possibility of constructing compact and mechanically stable devices with an open mode volume.

For experiments involving more than one optical field, the relative alignment of the corresponding fiber axes becomes an additional challenge. Conventional FFPC assemblies primarily define a single cavity axis. Introducing an additional pump fiber or a second cavity requires the corresponding axes to intersect within a small interaction volume while maintaining sufficient alignment precision and mechanical stability. In crossed-cavity experiments based on individually positioned optical elements, such as the quantum-network architecture demonstrated in Ref. [7], the relative cavity geometry is established through external alignment of the individual components. While this provides a high degree of flexibility, the relative positions of the optical elements have to be adjusted and their alignment maintained during the experiment.

A monolithic or mechanically predefined assembly instead fixes the relative positions of the fiber axes directly through the geometry of the structure [11, 12, 20]. This reduces the number of independently

adjustable degrees of freedom and can therefore simplify the initial alignment, improve reproducibility between assemblies, and potentially reduce relative mechanical drift. Such passive alignment is particularly attractive for compact and integrated devices in which the relative positions of several optical fields should remain fixed over long measurement times.

Photothermal spectroscopy (PTS) is one optical-sensing application that may strongly benefit from such a crossed-fiber-cavity platform [21–23]. In photothermal gas spectroscopy, a pump laser is tuned to an absorption transition of the target gas. Absorption of the pump light locally heats the gas, which changes its density and therefore its refractive index [22, 24, 25]. By modulating the pump power, a periodic refractive-index modulation is generated in the illuminated region. This refractive-index modulation can be detected using a second optical field, referred to as the probe beam. When the probe beam propagates through the heated region, the change in refractive index alters the accumulated optical phase of the probe light. The photothermal signal can therefore be detected through the corresponding phase modulation of the probe beam, without relying on a direct measurement of the weak pump absorption [24, 25].

The sensitivity of the probe can be increased by integrating the interaction region into an optical cavity. The probe field then passes repeatedly through the heated region, increasing the effective interaction length, while the cavity resonance provides a sensitive measure of changes in optical path length [22, 26, 27]. This principle has already been applied successfully in photothermal gas sensing using Fabry–Pérot interferometers and, more recently, miniaturized fiber Fabry–Pérot cavities [28, 29]. The latter includes work by our collaborators from the laser-spectroscopy group at Wrocław University of Science and Technology.

In this configuration, the pump beam has to cross the probe cavity mode within the central interaction region. The achievable photothermal signal therefore depends not only on the optical properties of the cavity and the absorption of the gas, but also on the spatial overlap between the pump beam and the cavity field. In the previously demonstrated setup, the pump beam was introduced using free-space optics. This implementation required careful external alignment and clipping at the fiber structures limited the usable pump power within the interaction region [28]. Replacing the free-space pump path by an additional fiber guide offers the possibility of defining the relative pump and probe positions mechanically and in close proximity, while potentially reducing clipping losses and alignment complexity [23, 30] and improving the long-term stability of the sensor. Such properties are particularly relevant for field-deployable optical gas sensors, for example in industrial or mining environments as well as for atmospheric monitoring [31].

The goal of this thesis is therefore to develop a compact assembly platform for this photothermal sensing scheme in which the relative position of the probe cavity and an orthogonal pump axis is defined mechanically by the assembly itself. This work was carried out in close collaboration with the laser-spectroscopy group at Wrocław University of Science and Technology, for whose photothermal sensing experiments the resulting assemblies are intended.

The same platform can furthermore be extended from a single FFPC crossed by a propagating pump beam to two orthogonal cavities. In this configuration, the pump field can itself be resonantly enhanced in a second cavity. This would increase the pump intensity within the sensing volume and thereby increase the absorbed optical power for weakly absorbing gas species or low target-gas concentrations [29, 32].

The intended geometry imposes several requirements on the assembly. Based on the parameters of the intended photothermal sensing implementation, the probe cavity operates near a wavelength of 1 550 nm and consists of fiber mirrors with radii of curvature of approximately 300 µm. Cavity lengths around 120 µm are targeted as a compromise between a compact cavity geometry and sufficient optical access to the central interaction region for the pump field. A transverse cavity-mode radius on the scale of several

micrometers requires the relative positioning of the orthogonal axes to be controlled on the micrometer scale. At the same time, the cavity fibers have to remain movable along their optical axes to enable cavity-length tuning.

These requirements define the main technical challenge of this work: combining precise relative alignment of several fiber axes with the mechanical requirements of a tunable high-finesse cavity. After introducing the basic properties of fiber Fabry–Pérot cavities in Chapter 2 and the fabrication and characterization of fiber mirrors in Chapter 3, three different assembly concepts are presented and investigated with respect to their fabrication and practical implementation in Chapter 4. Their alignment precision and reproducibility, together with suitable methods for characterizing the relative alignment achieved by the different concepts, are evaluated in Chapter 5. Based on these results, the design and first implementation steps of a final platform for the realization of two crossed fiber Fabry–Pérot cavities are presented in Chapter 6. Finally, a conclusion and an outlook are given in Chapter 7.

CHAPTER 2

Fiber Fabry–Pérot Cavity System

2.1 Fundamentals of Fabry–Pérot Cavities

The principles of Fabry–Pérot cavities are well established and have been described extensively in the literature, e.g. in Ref. [33]. Therefore, only the concepts and formulas required for this work are summarized here. More detailed descriptions can be found in the aforementioned reference.

A Fabry–Pérot resonator consists of two reflective mirrors facing each other and separated by a distance L_{cav}. Depending on the mirror properties, light can be reflected multiple times between them. When the round-trip phase is an integer multiple of 2π, the circulating fields interfere constructively and a steady-state intracavity field can build up.

A resonator formed by two spherical mirrors supports a set of transverse eigenmodes whose spatial field distributions reproduce themselves after each round trip. The fundamental TEM_{00} mode generally experiences the lowest diffraction and clipping losses and is therefore the dominant mode considered in this work. Its intensity distribution can be approximated by a Gaussian transverse envelope modulated by a longitudinal standing-wave pattern [34],

$$I(x,y,z) = I_0 \left(\frac{w_0}{w(z)}\right)^2 \exp\left[-\frac{2\left(x^2+y^2\right)}{w^2(z)}\right] \sin^2(kz), \tag{2.1}$$

where the cavity axis is chosen as the z-axis, w_0 is the waist radius, and $w(z)$ is the beam radius at the position z, measured relative to the waist position. The beam radius $w(z)$ is given by [33]

$$w(z) = w_0 \sqrt{1 + \left(\frac{z}{z_{\mathrm{R}}}\right)^2}, \tag{2.2}$$

with the Rayleigh range z_{R}.

For a cavity consisting of two spherical mirrors, the waist radius is given by [33]

$$w_0^2 = \frac{\lambda}{\pi} \sqrt{\frac{L_{\mathrm{cav}}\left(R_1 - L_{\mathrm{cav}}\right)\left(R_2 - L_{\mathrm{cav}}\right)\left(R_1 + R_2 - L_{\mathrm{cav}}\right)}{\left(R_1 + R_2 - 2L_{\mathrm{cav}}\right)^2}}, \tag{2.3}$$

provided that the cavity lies within the stability range. A two-mirror cavity is geometrically stable

when $0 < g_1 g_2 < 1$, with $g_i = 1 - L_{\mathrm{cav}}/R_i$. Consequently, the spatial geometry of the Gaussian cavity mode is fully determined by the mirror radii of curvature, the cavity length, and the wavelength.

Within the Gaussian envelope, a longitudinal standing-wave pattern arises from the interference of the counterpropagating fields. The free spectral range (FSR) is given by [12]

$$\Delta\nu_{\mathrm{FSR}} = \frac{c}{2nL_{\mathrm{cav}}}, \tag{2.4}$$

and corresponds to the frequency spacing between adjacent longitudinal resonances. For an air-filled cavity, $n \approx 1$, such that the FSR reduces to $\Delta\nu_{\mathrm{FSR}} \approx c/(2L_{\mathrm{cav}})$.

The circulating field results from the coherent superposition of the field transmitted into the cavity and all fields remaining after successive round trips. During each round trip, part of the circulating field leaves the cavity through the mirrors. The field detected in reflection from the incoupling side is the coherent superposition of the promptly reflected field and the field leaking out of the cavity through the incoupling mirror. Assuming lossless propagation between the mirrors, the reflected field can be expressed as [11]

$$E_{\mathrm{r}} = E_{\mathrm{in}}\left[r_1 - \frac{t_1^2 r_2 \exp(\mathrm{i}\phi)}{1 - r_1 r_2 \exp(\mathrm{i}\phi)}\right], \tag{2.5}$$

where $\phi = 2kL_{\mathrm{cav}}$ is the round-trip propagation phase. The quantities r_i and t_i denote the amplitude reflection and transmission coefficients of mirror i, respectively, while $\mathcal{R}_i$ and T_i are the corresponding power coefficients. For an ideal lossless mirror, $|r_i| = \sqrt{\mathcal{R}_i}$ and $|t_i| = \sqrt{T_i}$. If the mirror additionally introduces a power loss $\mathcal{L}_i$, its amplitude reflectivity is given by

$$|r_i| = \sqrt{1 - T_i - \mathcal{L}_i}. \tag{2.6}$$

On resonance, destructive interference between the promptly reflected and cavity-leakage fields reduces the reflected intensity. Under ideal mode-matching and detection conditions, the reflected-intensity resonance is symmetric and can be described by a Lorentzian-like line shape close to resonance.

In the presence of imperfect mode matching, the promptly reflected field and the cavity-leakage field can have different spatial profiles. Consequently, they couple back into the guided fiber mode with different complex amplitudes, while the remaining optical power is coupled into cladding or radiation modes. Since the phase of the cavity-leakage field varies across the resonance, interference between the guided components introduces a dispersive contribution to the detected signal and produces an asymmetric reflection line shape [11].

The spectral width of an individual cavity resonance is described by its full width at half maximum (FWHM), denoted by $\Delta\nu_{\mathrm{FWHM}}$. For a reflection dip, the FWHM is measured between the two frequencies at which the reflected intensity reaches half of the resonance-dip depth relative to the off-resonant baseline.

The finesse $\mathcal{F}$ quantifies the spectral quality of the cavity and can be experimentally determined through [12]

$$\mathcal{F} = \frac{\Delta\nu_{\mathrm{FSR}}}{\Delta\nu_{\mathrm{FWHM}}}. \tag{2.7}$$

For a high-finesse cavity with small mirror transmissions and intracavity losses, the finesse can be approximated as [34]

$$\mathcal{F} \approx \frac{2\pi}{T_1 + T_2 + \mathcal{L}_{\mathrm{rt}}}, \tag{2.8}$$

where $\mathcal{L}_{\mathrm{rt}}$ denotes the total round-trip intracavity power loss. It includes absorption, scattering, diffraction, and clipping losses, but excludes the mirror transmissions T_1 and T_2, which are stated separately in the denominator.

For a given cavity length, a higher finesse therefore corresponds to narrower resonances, a longer photon lifetime, and a larger average number of round trips before the intracavity power is transmitted or lost.

2.1.1 Fiber-Based Fabry–Pérot Cavities

Compared with macroscopic free-space cavities, optical microcavities enable smaller cavity lengths, beam waists, and mode volumes. This is particularly advantageous for applications requiring strong light–matter interaction. In photothermal gas sensing, a compact cavity reduces the required sample volume and enables the construction of a small and transportable sensor system.

In a fiber-based Fabry–Pérot cavity, the optical field is guided directly to and from the cavity through an optical fiber. This reduces the amount of external free-space alignment required. However, the same fiber also acts as a spatial mode filter for the reflected field.

The characteristic geometry and target parameters of the fiber Fabry–Pérot cavities considered throughout this work are shown in Figure 2.1. Both mirror radii of curvature were chosen to be approximately 300 µm. The target cavity length throughout most of this work was approximately 120 µm, well within the stable range of the corresponding cavity geometry. In addition to the cavity geometry, the mirrors were designed for high-finesse operation, with target mirror transmissions below 10 ppm. The resulting transmission and reflection properties are discussed in Subsection 3.1.3.

2.2 Alignment of Fiber Fabry–Pérot Cavities

The relative alignment of the two fiber mirrors is particularly important for high-finesse cavities. Owing to the small dimensions and finite usable area of the fiber mirrors, lateral and angular misalignment can strongly affect the cavity performance.

The cavity alignment directly influences the strength and contrast of the measured resonance signal. In reflection measurements, the resonance appears as a reduction in reflected power caused by interference between the promptly reflected field and the field leaking out of the cavity. The relative depth of this resonance dip is referred to here as the incoupling efficiency η_{dip}. Assuming that the off-resonant reflected power corresponds to the incident power, it can be written as [11]

$$P_{\mathrm{refl,min}} = \left(1 - \eta_{\mathrm{dip}}\right) P_{\mathrm{in}}.$$

A value of $\eta_{\mathrm{dip}} = 1$ corresponds to complete extinction of the reflected signal on resonance.

The factors determining the resonance depth can be separated approximately into two contributions [34],

$$\eta_{\mathrm{dip}} \approx \eta_{\mathrm{MM}}\, \eta_{\mathrm{imp}},$$

where η_{MM} is the optical mode-matching efficiency and η_{imp} is the impedance-matching efficiency.

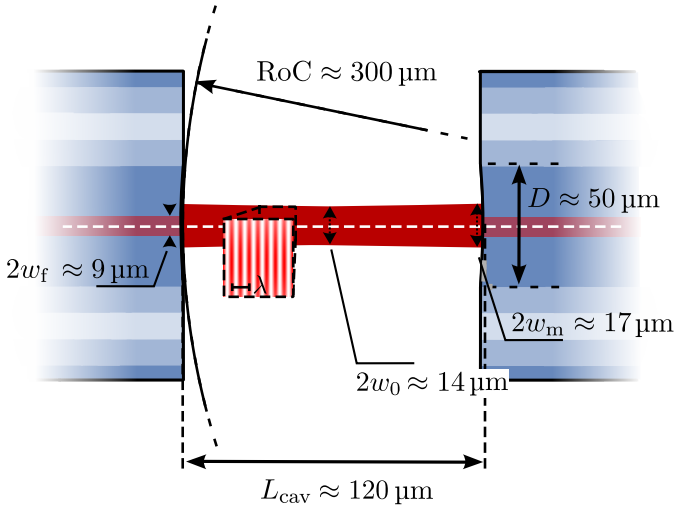


Figure 2.1: Schematic illustration of the Gaussian fundamental mode of a fiber Fabry–Pérot cavity with a cavity length of $L_{\mathrm{cav}} = 120\,\mu\mathrm{m}$. Both fiber mirrors have a radius of curvature of $\mathrm{RoC} = 300\,\mu\mathrm{m}$ and an effective mirror diameter of approximately $D = 50\,\mu\mathrm{m}$, representative of the fibers used in this work. The mode radius of the field emerging from the incoupling fiber is approximately $w_{\mathrm{f}} = 4.5\,\mu\mathrm{m}$, while the cavity-mode radius at the mirror surfaces is approximately $w_{\mathrm{m}} = 8.5\,\mu\mathrm{m}$. The cavity-mode waist is $w_0 = 7\,\mu\mathrm{m}$ for a wavelength of $\lambda = 1\,550\,\mathrm{nm}$. The enlarged region illustrates the longitudinal standing-wave intensity modulation, with adjacent intensity maxima separated by $\lambda/2$.

Mode matching describes the spatial overlap between the guided fiber mode and the cavity eigenmode, whereas impedance matching describes the balance between the transmission of the incoupling mirror and the remaining cavity losses. Although both contributions may change simultaneously during mechanical alignment, their separate treatment is useful for identifying the physical mechanisms that limit the measured resonance depth.

2.2.1 Impedance Matching

From Equation 2.5, the impedance-matching efficiency for the minimum reflected power on resonance can be written as [35]

$$\eta_{\mathrm{imp}} = 1 - \left(\frac{T_1 - T_2 - \mathcal{L}_{\mathrm{rt}}}{T_1 + T_2 + \mathcal{L}_{\mathrm{rt}}} \right)^2 . \tag{2.9}$$

The impedance-matching efficiency reaches its maximum value of $\eta_{\mathrm{imp}} = 1$ when

$$T_1 = T_2 + \mathcal{L}_{\mathrm{rt}}.$$

In this case, the transmission of the incoupling mirror exactly matches the sum of the transmission through the second mirror and the additional round-trip intracavity losses. The cavity is then critically coupled, or impedance matched, and the reflected field vanishes on resonance for perfect spatial mode matching.

If $T_1 > T_2 + \mathcal{L}_{\mathrm{rt}}$, the cavity is overcoupled, whereas for $T_1 < T_2 + \mathcal{L}_{\mathrm{rt}}$ it is undercoupled. In the cavities used in this work, both mirrors were designed to have a transmission of approximately 10 ppm.

Since additional intracavity losses are always present, the condition $T_1 = T_2 + \mathcal{L}_{\mathrm{rt}}$ cannot be fulfilled for identical mirror transmissions. The cavities are therefore expected to be undercoupled, with $\eta_{\mathrm{imp}} < 1$.

2.2.2 Optical Mode Matching

Another factor influencing the intensity of the detected reflection signal is the spatial overlap between the electric field emerging from the incoupling fiber and the cavity field. The degree to which both field distributions match can be quantified using the spatial mode-overlap integral [36, 37].

The spatial mode overlap depends on several properties of the fiber mode, the cavity mode, and their relative alignment. To estimate the influence of the individual contributions, the mode-matching efficiency can be approximated as the product of separate factors. This factorization is sufficient for the estimates presented here. However, the complete overlap integral in Equation A.1 must generally be evaluated when an exact description is required.

The approximate factorized mode-matching efficiency is written as [11, 37]

$$\eta_{\mathrm{MM}} \approx \eta_0 \, \eta_\theta \, \eta_d, \tag{2.10}$$

where η_0 describes the overlap for perfect lateral and angular alignment, η_d accounts for a lateral displacement between the fiber and cavity modes, and η_θ accounts for an angular mismatch between their propagation axes. The corresponding expressions are given in Appendix A.1. In the present system, a lateral mismatch can arise from an offset between the fiber core and the center of the laser-machined mirror depression, while an angular mismatch can result from a non-zero cleave angle and the corresponding tilt of the fabricated mirror surface. The remaining factor η_0 accounts for the intrinsic beam-shape mismatch between the fiber mode and cavity mode, caused by differences in their mode radii and wavefront curvatures.

Within the scope of this thesis, the magnitude of the individual contributions can be estimated for a representative cavity. The targeted cavity length was $L = 120\,\mu\mathrm{m}$ and the mirror radii of curvature varied between fibers but were typically close to $300\,\mu\mathrm{m}$, with deviations of up to approximately $50\,\mu\mathrm{m}$.

For the following estimate, radii of curvature of $R_1 = 290\,\mu\mathrm{m}$ and $R_2 = 310\,\mu\mathrm{m}$ are assumed. The incoupling fiber has a mode-field diameter specified by the manufacturer IVG Fiber [38] of $\mathrm{MFD} = 9\,\mu\mathrm{m}$. The average lateral offset between the center of the mirror depression and the fiber core was approximately $d = 2\,\mu\mathrm{m}$, while an angular mismatch of $\theta = 0.5^\circ$ is assumed.

Substitution of these values into the expressions included in Appendix A.1 gives

$$\eta_0 \approx 66\,\% \qquad \eta_d \approx 92\,\% \qquad \eta_\theta \approx 99\,\%.$$

The resulting total mode-matching efficiency is therefore

$$\eta_{\mathrm{MM}} \approx \eta_0 \eta_d \eta_\theta \approx 60\,\%.$$

For the assumed parameters, the dominant limitation is therefore the beam-shape mismatch, while the reductions caused by lateral and angular misalignment are smaller. Even for perfect impedance matching, only approximately 60 % of the incident power can therefore couple to the fundamental cavity mode under these assumptions.

Mechanical misalignment of the fiber mirrors can influence both the mode-matching and impedance-matching efficiencies. A lateral or angular offset between the fiber mode and the cavity mode reduces

their spatial overlap and therefore lowers η_{MM}. Misalignment can additionally increase the coupling to higher-order transverse cavity modes. For larger offsets, the cavity mode can also approach the finite edge of the mirror depression, increasing clipping and diffraction losses. These additional intracavity losses reduce the finesse and simultaneously alter the impedance-matching condition through $\mathcal{L}_{\mathrm{rt}}$. Thus, mechanical alignment affects the measured reflection signal through both spatial mode overlap and cavity loss.

2.2.3 Polarization Splitting

Imperfections in the fiber-mirror fabrication process can result in different radii of curvature along the two principal axes of a mirror, leading to an elliptical mirror profile. This ellipticity introduces a polarization-dependent phase shift during each cavity round trip and therefore lifts the degeneracy of the two orthogonal polarization eigenmodes. As a result, a single cavity resonance can split into two polarization resonances, with the frequency separation depending on the ellipticity of the cavity mirrors [39].

When two elliptical fiber mirrors form a cavity, their relative orientation also influences the resulting polarization splitting. Rotating one fiber mirror with respect to the other changes the combined differential phase shift introduced by the two mirrors. If the contributions of both mirrors are comparable, the polarization splitting can be reduced and, for equal differential phase shifts, can in principle be compensated completely.

Whether the two polarization resonances can be resolved experimentally depends on their frequency separation relative to the cavity linewidth. If the splitting is smaller than the linewidth, the resonance can appear approximately degenerate. For sufficiently narrow resonances, however, the two polarization modes become distinguishable. Owing to the high finesse and correspondingly narrow linewidths of the cavities investigated in this work, polarization splitting was therefore frequently observed. An example is shown in Figure 3.6, where polarization-mode splitting is visible in the EOM sidebands, while it is less pronounced in the main resonance.

The relative coupling strength to the two polarization eigenmodes depends on the polarization of the incoupling light. By adjusting the input polarization, the coupling to one polarization mode can be enhanced while the other is strongly suppressed. Since the polarization splitting did not significantly affect the cavity characterization or its intended application for gas sensing in this work, residual splitting was generally accepted.

CHAPTER 3

Fiber Mirror Fabrication & Characterization

The general fabrication and characterization procedures for fiber mirrors have been described extensively in previous work, e.g., in Refs. [12, 34, 40]. Since the mirrors used in this thesis were fabricated specifically for the present experiments, the relevant fabrication parameters, fabrication-specific challenges, and resulting mirror properties are summarized here. In addition, the high target finesse required modifications to the characterization procedure used to identify suitable mirror pairings.

3.1 Fiber Mirror Fabrication

The fiber mirrors used throughout this work were fabricated using the in-house laser-machining setup of the Bonn FiberLab [41]. The following section summarizes the fabrication procedure and the specific challenges encountered for the fiber mirrors used in this thesis. A detailed description and characterization of the laser-machining setup can be found in [34, 42].

The preparation of the fiber mirrors consists of three main steps. First, the fiber tip is prepared with a sufficiently flat surface to enable controlled laser ablation. Second, the surface is ablated using a CO_2 laser, producing a concave depression whose radius of curvature, depth, and ellipticity depend on the ablation parameters. Finally, the machined fiber tips are coated with a dielectric reflective coating. The individual steps are described in more detail below.

3.1.1 Fiber Preparation

The fiber mirrors were fabricated on 60 cm long pieces of copper-coated single-mode Cu1300 fiber manufactured by IVG Fiber [38]. The fibers consist of a pure-silica core with a diameter of approximately 5 µm and a surrounding cladding with a diameter of 125 µm. An additional carbon layer and an outer copper-alloy coating surround the cladding.

At one end of each fiber, the copper coating was removed by immersing the fiber in an $FeCl_3$ solution, leaving the inner carbon layer intact. This carbon layer was retained during the mirror-fabrication run used in this work, but can alternatively be removed by plasma ashing [40].

The stripped fiber end was subsequently cleaved to obtain a flat surface for laser machining. The autocleaver by Nyfors Teknologi AB was used with a tension setting of 190 g, which provided the best surface quality and cleave-angle results in preliminary tests performed for this work. Small cleave angles

are generally important for subsequent fiber-mirror fabrication [43]. With this setting, cleave angles below approximately 0.5° were typically obtained.

However, the performance of the cleaver varied over the course of a day, resulting in noticeable variations in the surface quality between individual fibers. Since imperfections of the cleaved surface directly influence the subsequent laser-ablation process, this also affected the achievable mirror quality.

The cleaved surfaces were inspected using the white-light/green-light interferometer integrated into the laser-machining setup. Surface irregularities can be identified through distortions of the interference pattern caused by nonparallel or uneven surface regions. The interferometer is described in more detail in [42].

Representative examples are shown in Figure 3.1. In Figure 3.1(a), pronounced surface artifacts are visible, making the fabrication of a well-defined concave mirror surface nearly impossible. Figure 3.1(b) shows a surface containing one dominant defect, which resulted in strongly elliptical ablation profiles. In contrast, Figure 3.1(c) shows a typical surface without pronounced interference-pattern distortions, which generally produced reproducible ablation profiles. Variations in cleave quality therefore reduced the number of fibers suitable for further mirror fabrication.

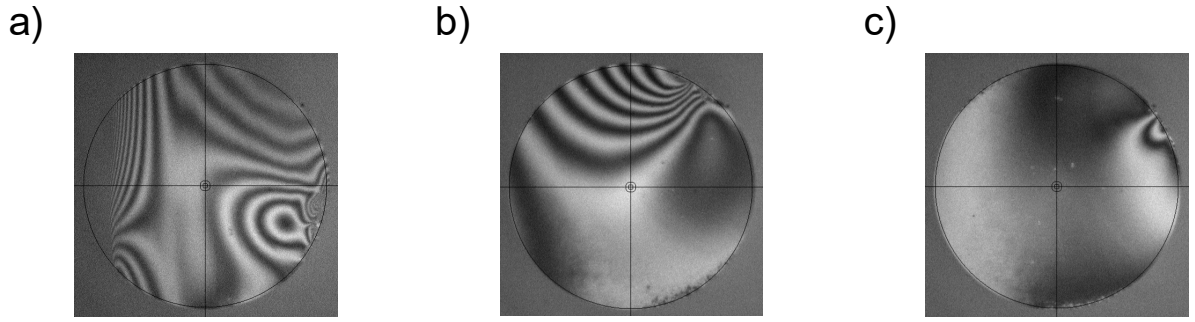


Figure 3.1: Examples of cleaved fiber surfaces observed with the green-light interferometer integrated into the laser-machining setup. (a) Poor cleave with pronounced surface artifacts. (b) Cleaved surface containing one large defect, likely introduced by the cleaver blade, resulting in an uneven surface. (c) Typical cleaved surface considered suitable for subsequent laser machining. The small artifact visible at the edge is generally present and corresponds to the entry point of the cleaver blade.

The fibers were then mounted in a fiber holder capable of clamping up to 26 fibers simultaneously, with the cleaved surfaces oriented towards the CO_2 laser for the subsequent ablation process.

3.1.2 CO_2 Laser Ablation

For the ablation process, a CO_2 laser operating at 9.3 µm is focused onto the fiber surface. Depending on the targeted radius of curvature, the pulse duration, number of pulses, and laser intensity are varied. These quantities are referred to as the shooting parameters throughout this work.

The fiber holder is mounted on a motorized translation stage, and the fiber surface can be observed using the integrated white-light or green-light interferometer. This allows tilted or uneven fiber surfaces to be identified, as illustrated in Figure 3.1. The tilt of the fiber surface can be adjusted using a rotation stage mounted on the translation stage. Since the interferometer is aligned parallel to the CO_2-laser beam path, optimizing the fiber-surface orientation with respect to the interferometer simultaneously aligns it with respect to the laser beam. For an optimally aligned fiber surface, no pronounced interference fringes

are visible, indicating that the fiber surface is approximately perpendicular to the beam propagation direction.

To center the laser ablation on the fiber core, the required translation-stage positions were calibrated before each shooting day using test shots on a glass substrate. This was necessary because the positioning of the stage showed a small drift between individual shooting sessions. In addition, the laser output itself varied over time. The shooting parameters therefore had to be adjusted during the fabrication run in order to obtain comparable mirror geometries for the individual fibers.

Even after optimizing the centering and shooting parameters, each laser-machined indentation differs slightly. The most important geometric parameters affecting the suitability of the resulting fiber mirror for cavity operation are illustrated in Figure 3.2. The first is the radius of curvature, shown in Figure 3.2(b), which, as discussed above, determines the cavity-mode geometry. The second is the position of the mirror depression relative to the center of the fiber core, shown in Figure 3.2(c). Such an offset reduces the spatial overlap between the guided fiber mode and the cavity mode. The third is the cleave angle and therefore the orientation of the mirror surface, illustrated in Figure 3.2(d), which can influence the orientation of the cavity mode. For the cavity geometries investigated in this work, the lateral offset and cleave angle should therefore be minimized, while the radius of curvature should be close to the targeted value of RoC = 300 µm.

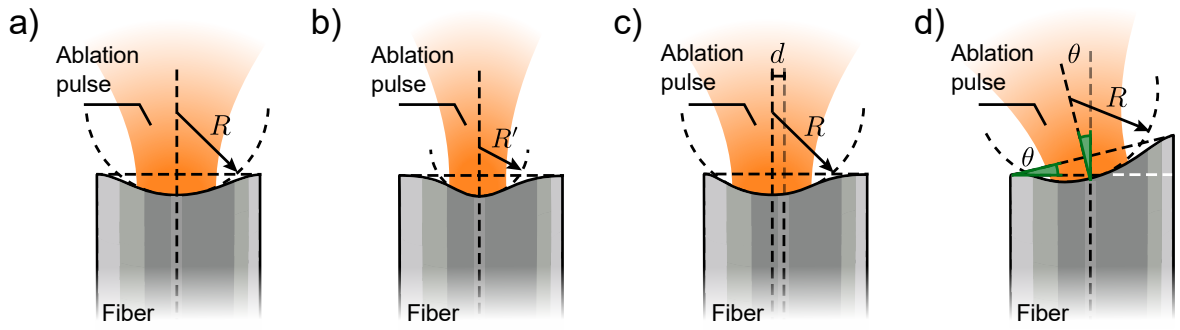


Figure 3.2: Illustration of important geometric parameters resulting from the laser-machining process that influence the properties and suitability of the fiber mirrors for cavity operation. (a) Ideally centered mirror depression with zero cleave angle and the targeted radius of curvature. (b) Centered mirror depression with zero cleave angle but a radius of curvature deviating from the targeted value. (c) Laterally offset mirror depression with zero cleave angle and the targeted radius of curvature. (d) Centered mirror depression with a non-zero cleave angle and the targeted radius of curvature.

After laser ablation, each fiber mirror was characterized using green-light phase-shifting interferometry. From the reconstructed surface profile, the radii of curvature along both principal axes, the indentation depth, useful mirror diameter, ellipticity, and lateral offset of the mirror depression relative to the fiber center were extracted. The resulting mirror profiles corresponding to the cleaved surfaces shown in Figure 3.1 are presented in Figure 3.3. These examples show that uneven cleave surfaces, as shown in Figure 3.3(a) and (b), can result in larger ellipticities and lateral offsets of the ablated mirror depressions, which may reduce the achievable mirror quality. The characterization results for all fiber mirrors used in this work are summarized in Figure 3.4. The radii of curvature are centered around the targeted value of approximately 300 µm, while the useful mirror diameters are mostly close to 52 µm. In contrast, the ellipticity and lateral offset of the mirror depression show a broader distribution. The larger spread in

these quantities may partly result from variations in the cleave angle and surface quality before laser machining.

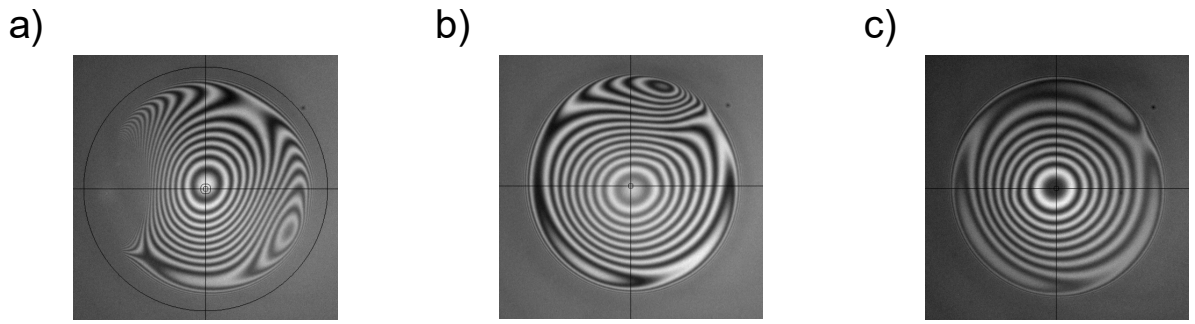


Figure 3.3: Examples of laser-ablated fiber surfaces corresponding to the cleaved surfaces shown in Figure 3.1, observed using the green-light interferometer integrated into the laser-machining setup. (a) The poor cleave with pronounced surface artifacts resulted in radii of curvature of $R_x = (329.89 \pm 0.44)$ µm and $R_y = (224.47 \pm 0.20)$ µm, an ellipticity of 1.47, an indentation depth of 5.49 µm, a useful diameter of 52.66 µm, and a lateral offset of 4.99 µm. (b) The cleaved surface containing one pronounced defect resulted in $R_x = (331.49 \pm 0.32)$ µm and $R_y = (259.23 \pm 0.20)$ µm, an ellipticity of 1.28, a depth of 1.55 µm, a useful diameter of 53.63 µm, and a lateral offset of 2.94 µm. (c) The typical cleaved surface resulted in $R_x = (280.29 \pm 0.17)$ µm and $R_y = (300.06 \pm 0.19)$ µm, an ellipticity of 0.93, a depth of 1.83 µm, a useful diameter of 48.68 µm, and a lateral offset of 0.48 µm.

3.1.3 Mirror Coating

After laser machining, the fiber mirrors were coated with dielectric mirror layers by Layertec GmbH [44]. The coating has a specified transmission of (10 ± 4) ppm at normal incidence within a wavelength range of 1 545 nm to 1 565 nm. The specified reflectivity is greater than 99.995 % between 1 530 nm and 1 577 nm and greater than 99.99 % between 1 648 nm and 1 654 nm, both at normal incidence. The corresponding manufacturer-specified reflection spectrum is shown in Figure A.1.

For two mirrors with a transmission of approximately 10 ppm and negligible additional losses, this corresponds to an idealized maximum finesse on the order of 3.1×10^5.

Overall, the fabrication process determines not only the radii of curvature and usable diameters of the fiber mirrors, but also their positions and orientations relative to the fiber cores. Deviations in these quantities can influence both the spatial overlap between the guided fiber mode and the cavity eigenmode and the optical losses of the resonator.

3.2 Fiber Cavity Characterization Setups

Two setups were used to evaluate the optical performance of the fabricated fiber mirrors. The first characterizes individual fiber mirrors in combination with a flat reference mirror, while the second assesses the performance of cavities formed by two fiber mirrors. Both setups are described in the following sections.

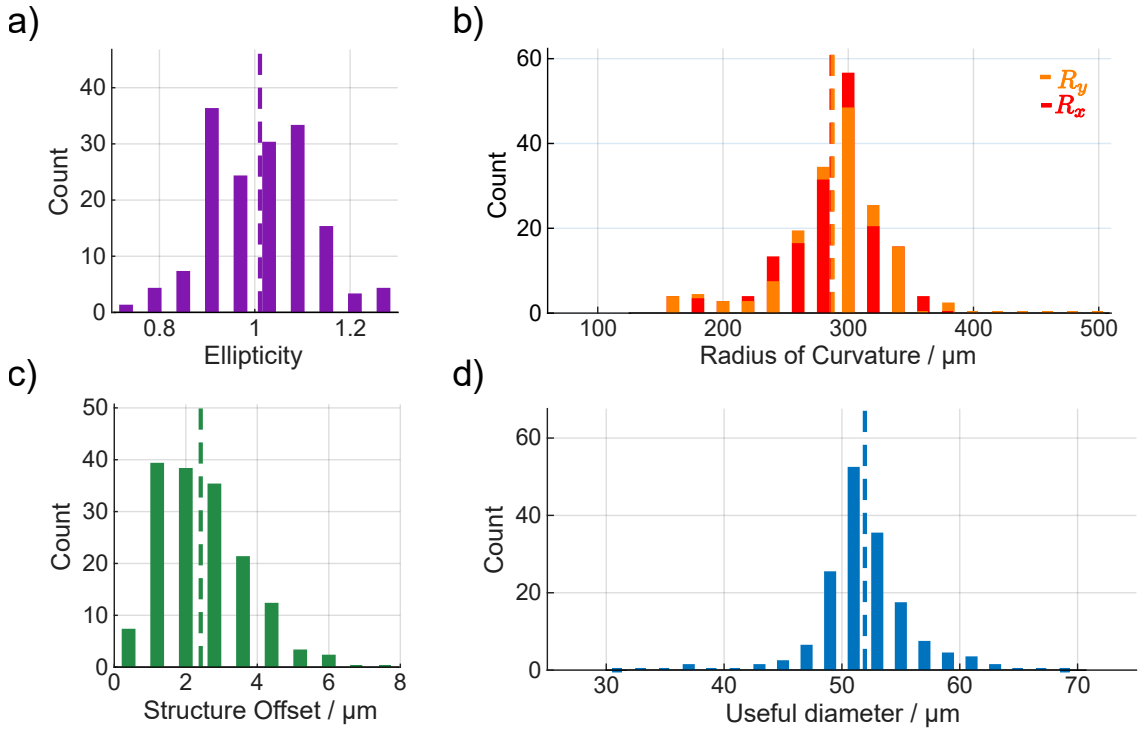


Figure 3.4: Histograms of the laser-machined fiber mirrors used in this work. (a) Distribution of the ellipticity, (b) radius of curvature, (c) lateral offset of the mirror depression relative to the fiber center, and (d) useful mirror diameter. The dashed lines indicate the mean value.

3.2.1 Fiber–Plane Mirror Cavity Characterization Setup

To estimate the quality of the fiber mirrors after the coating process, each fiber mirror was characterized in a hybrid cavity configuration. In this configuration, the fiber mirror is positioned opposite a flat DBR mirror, and the cavity resonance is observed in reflection through the fiber mirror. The flat reference mirror has the same nominal transmission of 10 ppm as the fiber mirrors. Its influence on the measured cavity properties therefore cannot be neglected. However, since the same reference mirror is used for all measurements, the extracted cavity characteristics provide a useful relative measure for comparing the quality of the individual fiber mirrors and their suitability for forming fiber–fiber cavities.

The general setup is shown in Figure 3.5. Light from a laser operating at 1 550 nm first passes through a 50/50 fiber-optical coupler, a polarization paddle, and an electro-optic modulator (EOM) before entering a fiber circulator. The circulator separates the reflected cavity signal from the incident light and minimizes back-reflections into the laser, while the polarization paddle controls the incoupling polarization into the EOM. Another polarization paddle positioned before the fiber mirror allows control over the polarization of the incoupling beam and thus over the excited polarization eigenmodes. The investigated fiber mirror is mounted on a piezo-driven translation stage, which allows the cavity length to be scanned across a resonance. The piezo stage is driven by a waveform generator through a 75× voltage amplifier. The orientation of the flat reference mirror can be adjusted to optimize the cavity alignment. The piezo-drive signal and the reflected cavity signal detected by a photodiode are recorded simultaneously on an oscilloscope.

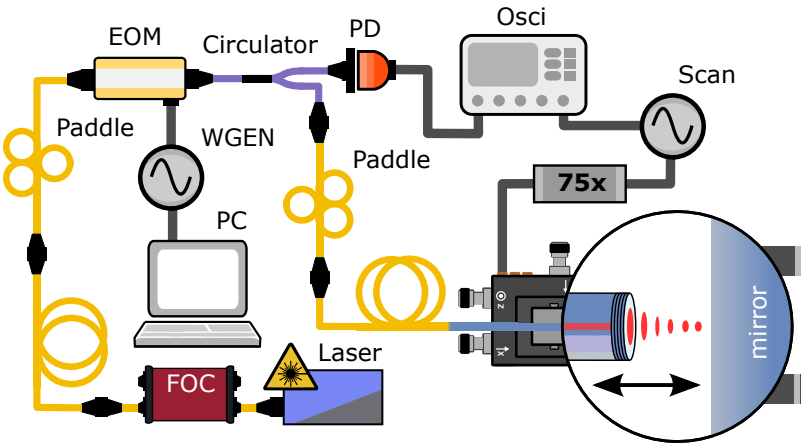


Figure 3.5: Setup for fiber-mirror characterization. Light from a laser operating at 1 550 nm is coupled into a 50/50 fiber-optical coupler (FOC) and subsequently passes through a polarization paddle and an electro-optic modulator (EOM). The EOM is driven by a waveform generator and is used to generate modulation sidebands for finesse calibration. A fiber circulator separates the light directed towards the measurement arm from the reflected signal. In the measurement arm, a second polarization paddle controls the polarization before the light is coupled into the fiber mirror under investigation. The fiber mirror is mounted on a piezo-driven translation stage and positioned opposite a flat reference mirror with the same nominal transmission of 10 ppm. The reflected cavity signal is detected with a photodiode and recorded on an oscilloscope together with the voltage driving the piezo stage. All optical elements are fiber coupled.

Due to the low mirror transmission and the correspondingly narrow cavity resonances expected for high-finesse operation, the setup is highly sensitive to mechanical vibrations. The complete setup was therefore mounted on a breadboard with vibration-damping feet, and the fiber was clamped as close as possible to the fiber end facet in order to reduce mechanical motion of the fiber mirror. In addition, the resonance dips could only be resolved reliably at sufficiently low scan speeds. At higher scan speeds, ringing effects became apparent and distorted the resonance lineshape [19]. This occurs because the intracavity field cannot decay instantaneously while the cavity is scanned through resonance, resulting in an oscillatory interference signal in reflection. For comparison, measurements with and without pronounced ringing are shown in Figure 3.6(a) and (b), respectively. When ringing is present, the modulated sideband resonances exhibit the same effect, as visible in Figure 3.6(a).

For the measurements presented here, the piezo stage was therefore driven with a triangular signal at 20 Hz and an amplitude of 80 $\mathrm{mV_{pp}}$. The offset voltage was adjusted to shift a cavity resonance into the accessible scan range.

Because of the narrow resonance linewidth and the limited cavity-length scan range, scanning across an entire free spectral range was not feasible. To nevertheless determine the resonance linewidth in frequency units, modulation sidebands were generated using an electro-optic modulator (EOM) positioned before the circulator. An additional polarization paddle placed before the EOM allows the polarization at the EOM input to be optimized and thereby controls the strength of the generated sidebands.

The frequency separation between the carrier and the modulation sidebands is set by the frequency applied to the EOM and is therefore known precisely [45]. The sideband resonances consequently provide a frequency reference within the cavity-length scan. This allows the time axis recorded by the oscilloscope to be converted into a relative frequency axis and thus enables the linewidth of the main

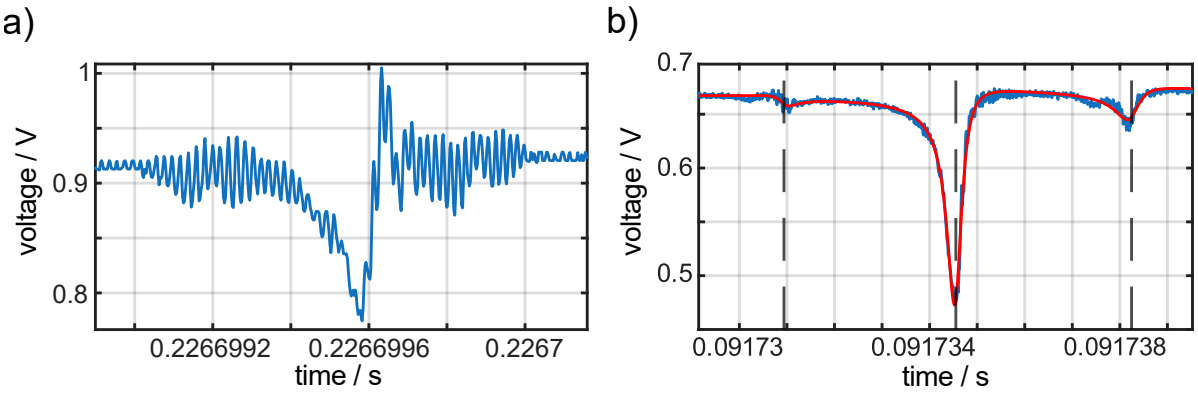


Figure 3.6: Example measurements using EOM sideband modulation for the finesse determination of the same cavity configuration. Polarization splitting is visible in the sideband resonances in both measurements. (a) Measurement at a comparatively high piezo scan speed using a triangular drive signal at 20 Hz and 1 V_{pp}. The main resonance exhibits an overshoot followed by an oscillatory structure, characteristic of cavity ringing caused by the rapid scan through resonance. The same effect is also visible in the sideband resonances. The sidebands were generated using a modulation frequency of $f_{mod} = 50$ MHz. (b) Measurement at a lower scan speed using a triangular drive signal at 20 Hz and 80 mV_{pp}. No pronounced ringing is visible, and the resonance follows the expected asymmetric Lorentzian-like lineshape. Sideband resonances can be identified on both sides of the main resonance, with their frequency separation from the carrier resonance determined by the EOM modulation frequency. The fitted resonance positions are indicated by vertical lines. The sidebands were generated using a modulation frequency of $f_{mod} = 100$ MHz.

cavity resonance to be determined. The FSR is subsequently estimated from the cavity length measured using the microscope image.

Finesse Extraction

To determine the resonance linewidth and position as accurately as possible, the measured reflection signal is fitted using a combination of a Lorentzian and a dispersive contribution [34],

$$y(x) = y_0 - \frac{A_L}{(x - x_0)^2 + w^2/4} + \frac{A_D(x - x_0)}{(x - x_0)^2 + w^2/4}, \tag{3.1}$$

where the first term describes the Lorentzian contribution to the resonance dip, while the second term accounts for the asymmetric dispersive contribution resulting from spatial mode filtering in the fiber. The parameter w corresponds to the FWHM of the Lorentzian contribution, while x_0 describes its center position. Owing to the dispersive contribution, the minimum of the complete fitted resonance does not necessarily coincide exactly with x_0. For the resonance shapes observed in this work, however, x_0 provides a sufficiently accurate estimate of the resonance position.

The sideband resonances have a known frequency separation from the main resonance given by the modulation frequency f_{mod}. The sideband positions are determined by applying the same fit function as in Equation 3.1. With t_- and t_+ denoting the positions of the two sideband resonances, the average temporal separation between the main resonance and either sideband is

$$\Delta t_{SB} = \frac{|t_+ - t_-|}{2}.$$

The conversion factor between the measured time axis and frequency is then

$$C_\nu = \frac{f_{\mathrm{mod}}}{\Delta t_{\mathrm{SB}}},$$

and the cavity linewidth in frequency units is obtained from

$$\Delta\nu_{\mathrm{FWHM}} = C_\nu \, \Delta t_{\mathrm{FWHM}}.$$

An example of a measured resonance with modulation sidebands and the corresponding fits is shown in Figure 3.6(b).

To determine the finesse, the FSR additionally has to be estimated. The cavity length is obtained from microscope images, using the known fiber diameter as a spatial calibration. The corresponding FSR is then calculated according to Equation 2.4. Finally, the finesse is determined using Equation 2.7.

3.2.2 Fiber–Fiber Cavity Characterization Setup

Since each fiber mirror has individual geometric characteristics, different mirror pairings have to be tested in order to assess the achievable cavity performance. Even if two individual fiber mirrors show promising coupling efficiencies and finesse values in the hybrid-cavity characterization, combining them does not necessarily result in a high-quality fiber–fiber cavity. Differences in lateral mirror offset, cleave angle, radius of curvature, and other geometric parameters can lead to additional losses and reduced mode-matching efficiency when the mirrors are paired.

For this reason, promising fiber mirrors were tested in combination with several other fiber mirrors in order to identify suitable pairings. For these measurements, the fiber pairs were inserted into a glass ferrule, which provided reproducible mechanical alignment of the two fibers during characterization. To further improve the coupling efficiency, one of the fiber mirrors was additionally mounted in a rotational holder, allowing the relative angular orientation of the two fiber mirrors to be adjusted. The cavity resonance was monitored in reflection through one of the fiber mirrors. The corresponding setup is shown in Figure 3.7. Apart from this modification, the measurement procedure was analogous to that used for the fiber–plane-mirror configuration described above. The best-performing mirror combinations were then selected for subsequent cavity assembly and application.

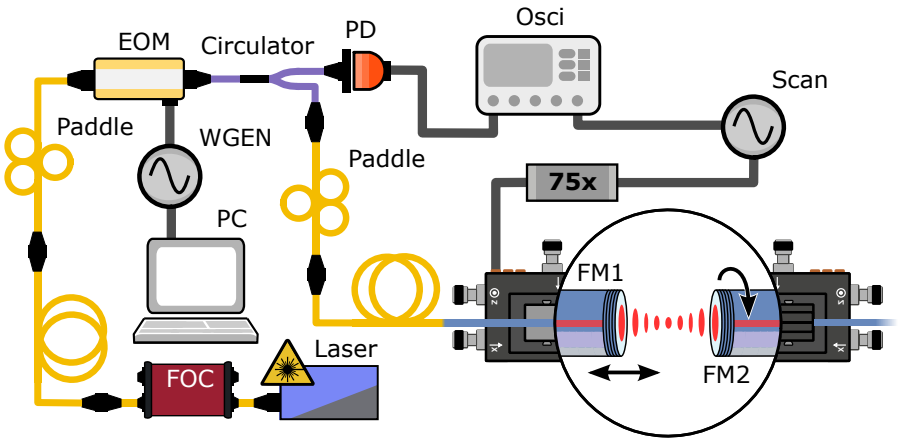


Figure 3.7: Setup for fiber–fiber cavity characterization. The optical components are arranged equivalently to the hybrid-cavity setup shown in Figure 3.5. In this configuration, however, the fiber mirror under investigation, FM1, is positioned opposite a second fiber mirror, FM2, instead of the flat reference mirror. FM2 is mounted in a rotatable fiber holder, allowing its orientation relative to FM1 to be adjusted in order to optimize the cavity alignment and coupling efficiency. This setup is used to determine the pairwise achievable finesse and coupling efficiency of two fiber mirrors.

CHAPTER 4

Design and Fabrication of the Assembly Platforms

Building on the fiber–fiber Fabry–Pérot cavities previously used for photothermal gas sensing by our collaborators [19], the aim of this work was to extend the concept towards mechanically predefined pump and probe axes. As introduced in Chapter 1, the photothermal signal depends on the spatial overlap between the pump field and the cavity probe mode. In the previously used configuration, the pump beam was focused into the cavity region using free-space optics, making its alignment relative to the cavity mode an additional experimental challenge.

This limitation, together with the aim of reducing the need for additional free-space optics, motivated the idea of guiding the pump beam through an additional optical fiber, hereafter referred to as the pump fiber, whose position can be controlled mechanically. As a first step, a three-channel 3D-printed ferrule had already been developed in previous work, with a geometry similar to that of a conventional glass ferrule but with an additional channel oriented orthogonally to the cavity axis [46]. This design allowed the pump fiber to be positioned close to the cavity region while reducing clipping by the surrounding ferrule structure. In that design, cavity lengths above approximately 100 µm were targeted in order to provide sufficient optical access between the fiber mirrors.

Building on the promising results of this approach, the concept was extended in this work to configurations with two opposing fibers positioned orthogonally to the probe-cavity axis. This configuration can either be used to introduce two different excitation beams into the interaction region, for example at different wavelengths, or, in a more advanced configuration, to form a second fiber cavity whose axis is orthogonal to that of the probe cavity.

A central requirement of such a crossed configuration is the spatial overlap of the two optical axes. Especially for photothermal gas sensing, the region excited by the pump beam has to overlap with the region probed by the cavity field in order to maximize the photothermal signal. For this reason, different assembly methods for aligning four fiber ends were developed and evaluated. The general configuration consists of two orthogonal optical axes, each defined by two opposing fiber ends. The two axes have to intersect within the free-space region between the fiber end facets.

From these considerations, the main design requirements can be summarized as follows:

- A mechanically stable structure that maintains the alignment of the fibers over extended periods of time.

- The ability to adjust the distance between opposing fiber ends, at least along the probe-cavity axis, in order to tune the cavity length and scan through resonance.
- Sufficient optical and physical access to the intersection region to enable interaction with the investigated sample or medium.
- Precise alignment of the two fiber axes such that they intersect within the intended interaction region.

Based on these requirements, two fabrication approaches were investigated. The first, described in Section 4.1, uses supporting grooves fabricated from Macor ceramic by the university workshop, while the second, described in Section 4.2, employs three- and four-channel ferrules produced by high-precision 3D printing using direct laser writing (DLW). The corresponding design, fabrication, implementation, and post-processing challenges are discussed in the respective sections.

4.1 Grooved Ceramic Holders

4.1.1 Holder Concepts and Design

The first assembly concepts were based on positioning the fiber tips in precisely machined grooves. A sufficiently precise groove constrains the lateral position of a fiber and can therefore provide reproducible alignment. To apply this concept to both optical axes, two orthogonally oriented grooves were machined into two different holder geometries fabricated from Macor, as shown in Figure 4.1 and Figure 4.2.

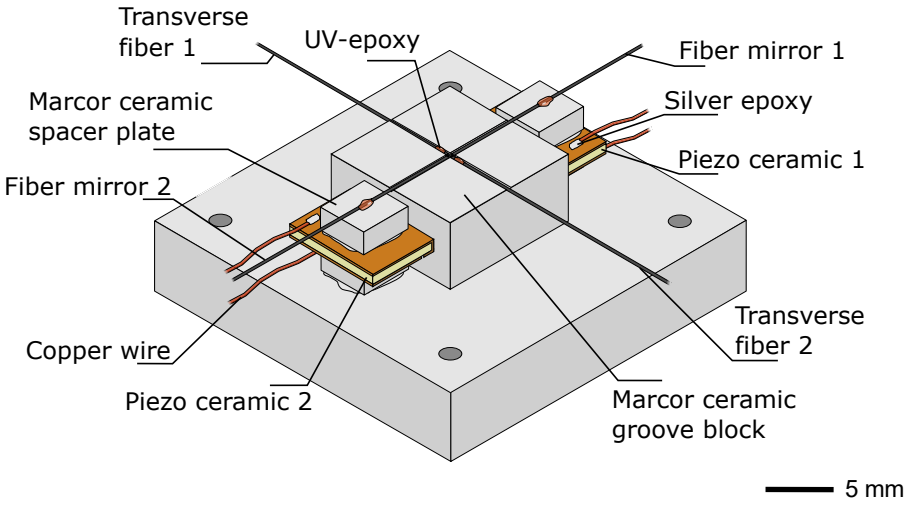


Figure 4.1: Sketch of the Macor block design. The central 10 mm × 10 mm and 5 mm high extrusion contains the two orthogonally oriented grooves. It is connected to a larger 30 mm × 30 mm and 5 mm high platform, providing space for additional components. Shear piezo elements mounted on the platform enable translation of the cavity fibers along the grooves when a voltage is applied. Additional Macor pieces are placed above and below the shear piezo elements to provide sufficient space for the electrical contacts and wires, while their combined height approximately matches that of the central extrusion. The components and electrical contacts are fixed using silver epoxy. The cavity fibers are attached to the upper Macor plates using UV-curable epoxy, while the pump fibers are fixed directly to the Macor block close to the cavity region. Detailed dimensions of the block design are provided in Figure A.4.

Macor was chosen as the base material due to its mechanical stiffness and electrically insulating properties. For the fabrication process used here, the Macor parts could additionally be fixed to a supporting surface by adhesive rather than by mechanical clamping, reducing the risk of stress-induced deformation during machining.

The fabrication nevertheless proved challenging for the university workshop. The required groove precision lies on the micrometer scale and is therefore considerably higher than for most components usually manufactured in the workshop. The specific fabrication challenges encountered are discussed in the following subsections.

The first concept is based on a monolithic block structure with a central square extrusion surrounded by a larger supporting platform, which can be seen in Figure 4.1. The two orthogonally oriented grooves are machined into the central extrusion, while the surrounding platform provides space for mounting additional components. Along the cavity axis, shear piezo elements are attached to the platform in order to translate the cavity fibers along the grooves and thereby vary the cavity length.

The piezo elements require electrical contacts on opposing surfaces in order to generate the intended shear motion. Additional Macor plates are therefore placed above and below the piezo elements, primarily to provide sufficient space for attaching the electrical contacts and wires. At the same time, their dimensions are chosen such that the combined height of the piezo element and Macor plates approximately matches the height of the central extrusion. The cavity fibers can then be positioned inside the grooves and attached to the upper Macor plates using UV-curable epoxy. The pump fibers, which are oriented orthogonally to the cavity axis, do not require longitudinal scanning and can instead be fixed directly to the Macor block close to the central interaction region.

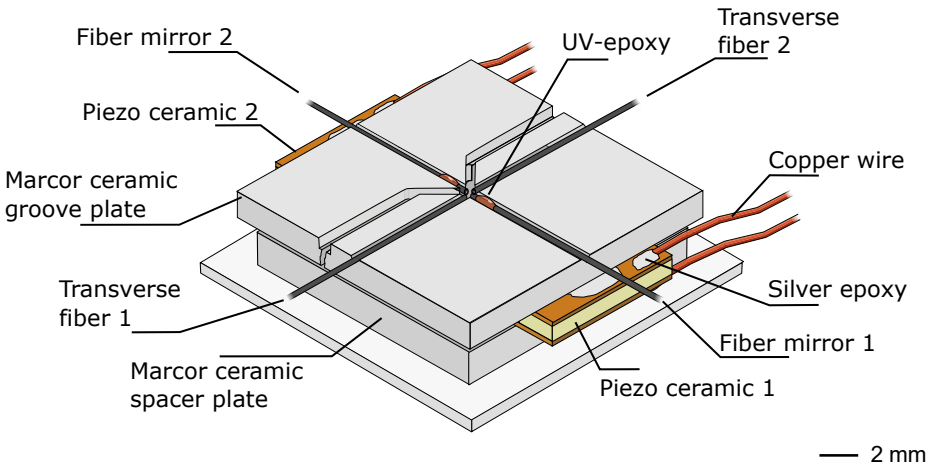


Figure 4.2: Sketch of the Macor plate design. The grooves are machined into a 10 mm × 10 mm and 2 mm high plate. Two shear piezo elements are attached to the underside of the plate on either side of the cavity region. An orthogonal cut separates the two sides of the cavity axis while leaving narrow connections at the outer edges to keep the plate mechanically intact during assembly. The piezo elements extend beyond the plate to provide access for the electrical contacts. The groove plate and piezo elements are subsequently mounted onto an additional Macor plate for mechanical support. After assembly, the remaining connections at the edges of the groove plate are cut, mechanically separating the two sides of the cavity axis. The cavity and pump fibers are then fixed inside their respective grooves using UV-curable epoxy. Detailed dimensions of the plate design are provided in Figure A.5.

The second concept is based on a considerably smaller Macor plate corresponding approximately to

the area of the central extrusion of the block design and can be seen in Figure 4.2. Again, two orthogonal grooves intersect at the center of the plate. In contrast to the block design, two shear piezo elements are attached directly to the underside of the groove plate on either side of the cavity region. Both piezo elements are subsequently mounted onto a common supporting Macor plate. The piezo elements extend beyond the edge of the groove plate to provide access for the electrical contacts. The corresponding fabricated Macor groove plate is shown in Figure 4.3, together with a close-up of the central groove intersection. Additional cuts are machined into the groove plate around the central cavity region, almost

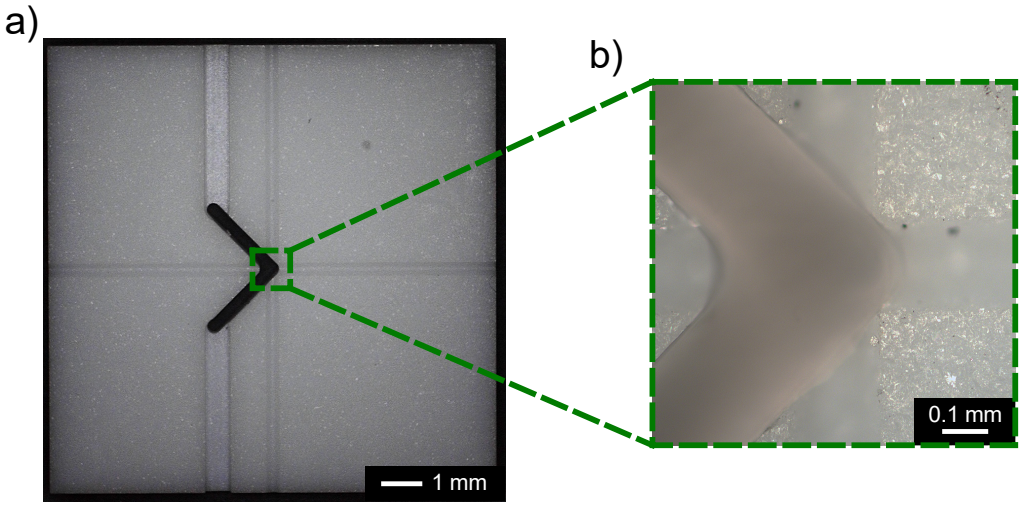


Figure 4.3: Microscope images of the fabricated Macor groove plate. (a) Overview of the complete groove plate with the two orthogonally oriented grooves. (b) Close-up of the central region where the two grooves intersect and define the intended position of the orthogonal fiber axes.

separating the two sides of the cavity axis. During assembly, narrow Macor connections at the outer edges keep the plate mechanically intact. After the piezo elements and supporting plate have been attached, these remaining connections can be cut through. The two sides of the cavity axis are thereby mechanically separated and can be displaced relative to each other by the shear piezo elements. In this design, both the cavity and pump fibers can be fixed inside their respective grooves close to the central interaction region.

Before evaluating the alignment performance of the two holder concepts, several practical limitations associated with the machined grooves themselves were identified. In particular, deviations from the specified groove dimensions and the mechanical behaviour of coated fibers inside the grooves had to be addressed. These aspects are discussed in the following subsections.

4.1.2 Groove Fabrication

The first generation of grooves was designed such that a fiber with a diameter of approximately 130 µm would lie completely inside the groove without protruding above the ceramic surface. The groove had an opening angle of 45°. A schematic illustration of the intended geometry is shown in the inset of Figure 4.4(a).

The fabricated grooves, however, deviated significantly from the intended geometry, as can be seen in the microscope image in Figure 4.4(a). This deviation resulted from the finite flat region at the bottom

of the milling tool. In principle, a small flat bottom would be feasible as long as its width remains sufficiently small compared with the fiber diameter. In that case, the fiber would still contact the inclined sidewalls of the groove and would therefore be laterally constrained when positioned at the lowest point.

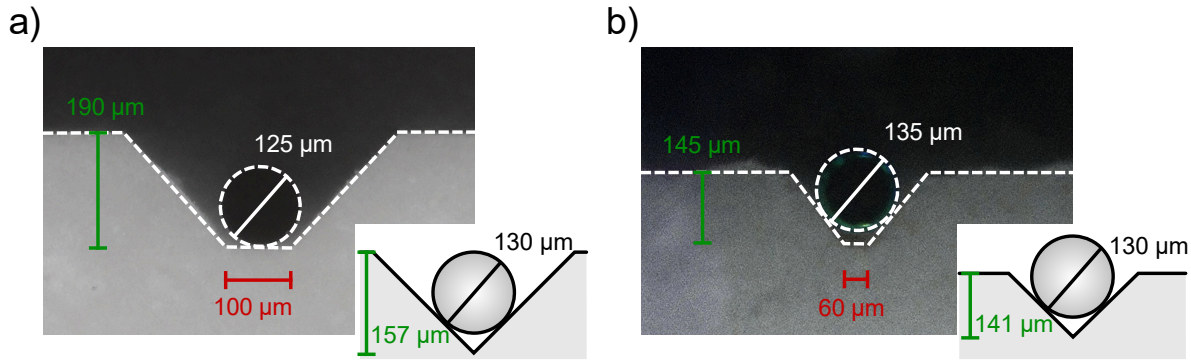


Figure 4.4: Images of the grooves manufactured by the university workshop. The inset in each panel shows the specified dimensions. (a) Result of the first groove design. According to the specified geometry, the top of a 130 µm-diameter fiber should align with the top surface of the ceramic when positioned at the deepest point of the groove. The fabricated groove, however, showed a flat bottom surface with a width of approximately 100 µm, allowing the fiber to move laterally even at the deepest position. In addition, a gap of approximately 75 µm remained between the top of the fiber and the ceramic surface. (b) Result of the final groove design. In the specified geometry, a 130 µm-diameter fiber protrudes above the ceramic surface when positioned at the deepest point of the groove. The fabricated groove still exhibits a flat bottom surface, but with a reduced width of approximately 60 µm. This allows the fiber to contact the inclined sidewalls, thereby constraining lateral movement. As intended, the fiber protrudes above the ceramic surface, allowing it to be pressed into the deepest position using a flat pressing element from above.

For the fabricated grooves, however, the flat bottom region was too wide, allowing the fiber to rest on the bottom surface without being tightly constrained by the sidewalls. Consequently, lateral motion of the fiber remained possible even when it was positioned at the deepest point of the groove. In addition, the fabricated grooves were deeper than specified. As a result, the upper surface of the fiber remained below the ceramic surface when inserted into the groove, making it more difficult to clamp the fiber in place.

The initial assumption was that the fiber would bend downwards under its own weight and therefore naturally settle into the groove. In practice, this was not always the case. In particular, fibers with excess coating material close to the end facet or residual copper coating beyond the clamping point exhibited a considerably higher stiffness and did not reliably conform to the groove geometry.

To keep the fibers in the lowest position of the grooves, several lid concepts were therefore designed and tested. Since the fibers were located below the ceramic surface, a flat lid alone was insufficient. Instead, protruding structures matching the groove positions were required to extend into the grooves and press the fibers down.

One attempted lid consisted of a conventionally 3D-printed part with corresponding protrusions. However, the printer resolution was insufficient to reproduce the required dimensions accurately. Another lid was fabricated from aluminium by the university workshop. In this case, the dimensions of the protruding structures differed considerably from the design and were therefore unable to reliably press the fibers into the grooves. The workshop subsequently concluded that the required geometry could not be manufactured with sufficient precision using the available equipment.

As a final approach, a lid was fabricated using a high-precision 3D printer. Owing to the long printing

time, only a small protrusion for a single groove was produced. Although the resulting geometry corresponded well to the design, the small dimensions and low mass of the polymer structure made it difficult to handle and insufficient for pressing the fiber into the groove without additional force.

Based on these tests, the groove geometry was redesigned. Instead of fully embedding the fiber below the ceramic surface, the groove depth was reduced such that part of the fiber protrudes above the surface even when positioned at the deepest point of the groove. This allows a simple flat lid to apply pressure directly to the fiber and hold it securely against the groove sidewalls.

After several iterations, the workshop succeeded in producing grooves suitable for further testing. The final geometry is shown in Figure 4.4(b). As intended, part of the fiber protrudes above the ceramic surface when positioned at the deepest point of the groove. Since the alignment concept relies directly on the groove geometry, the reproducibility of the fabrication process was additionally evaluated by comparing multiple nominally identical grooves.

For this comparison, an array of five nominally identical grooves with the specifications shown in Figure 4.4(b) was fabricated on a single Macor plate. Each groove was tested using the characterization setup described in Subsection 3.2.2, with the groove plate replacing the glass ferrule as the mechanical alignment structure. Two different fiber-mirror pairs were used, forming a low- and a high-finesse cavity, respectively, when sufficiently well aligned. During these measurements, the fibers were pressed into the grooves using pieces of a Sorbothane rod. The clamping procedure itself is discussed in Subsection 4.1.3.

For the low-finesse cavity, each groove was tested three times. Between individual measurements, the fiber mirrors were repositioned and reclamped in order to reproduce independent alignment conditions. As a reference, the same fiber pair was additionally characterized using a commercial glass ferrule with a specified channel diameter of 135 µm. The resulting coupling efficiencies are summarized in Table 4.1. The repeated measurements show that the obtained coupling efficiency depends noticeably on the exact

Table 4.1: Measured coupling efficiencies for a commercial glass ferrule with a specified channel diameter of 135 µm and five nominally identical grooves fabricated from Macor. Each groove was measured three times after repositioning and reclamping the fiber mirrors. GF denotes the glass ferrule and G1–G5 the five grooves.

Iteration	**GF**	**G1**	**G2**	**G3**	**G4**	**G5**
		Coupling efficiency / %				
1	41	42	26	36	31	29
2	35	26	27	27	28	31
3	–	38	36	28	30	35
Average	38.0	35.3	29.7	30.3	29.7	31.7

repositioning and clamping conditions. For example, the measured coupling efficiency of Groove 1 varies between 26 % and 42 %. The averages of the five grooves, however, range only from approximately 30 % to 35 %, compared with 38 % for the commercial ferrule. The differences between the individual groove averages and the ferrule reference are therefore approximately 3–8 percentage points. Considering the variation observed between repeated alignment measurements, no clear systematic reduction of the achievable coupling efficiency compared to the ferrule can be identified. The measurements therefore indicate that the grooves can provide an alignment comparable to that of the conventional glass ferrule.

In addition to the coupling efficiency, the cavity finesse was estimated for each groove and for the ferrule reference. The obtained values were all of the same order of magnitude. Since the finesse determination additionally depends on the linearity of the cavity-length scan and on the cavity length

estimated from the microscope image, the extracted values should primarily be used for comparison rather than interpreted as exact absolute finesse values. Similar finesse values therefore provide an additional indication that no strong additional intracavity losses are introduced by the individual grooves.

To further assess the performance of the grooves, a second test was performed using a fiber-mirror pair that forms a high-finesse cavity under good alignment. Such cavities are particularly sensitive to additional round-trip losses because their intrinsic loss budget is small. Misalignment of the fiber mirrors can introduce additional clipping or diffraction losses, which broaden the cavity resonance and thereby reduce the measured finesse. At the same time, imperfect mode matching between the fiber mode and the cavity mode reduces the observed resonance depth and therefore the measured coupling efficiency.

Comparing the coupling efficiencies and finesse values obtained under similar conditions for the different grooves therefore provides information on the reproducibility and precision of the alignment achieved by the groove structures. A comparison with the corresponding values obtained using a commercial glass ferrule under the same conditions additionally indicates how closely the groove-based alignment approaches the performance of the established ferrule geometry and how suitable the grooves are for high-finesse cavity formation. The measured coupling efficiencies and finesse values are summarized in Table 4.2. For this measurement, a commercial glass ferrule with a specified channel diameter of 142 µm was used as the reference, since the larger coating thickness of these fibers prevented their insertion into the 135 µm ferrule. The measured coupling efficiencies differ by at most 10 percentage

Table 4.2: Measured coupling efficiencies and corresponding cavity finesses for a commercial glass ferrule with a specified channel diameter of 142 µm and five nominally identical grooves fabricated from Macor. GF denotes the glass ferrule and G1–G5 the five grooves. The target cavity length was approximately 100 µm for all measurements.

	GF	**G1**	**G2**	**G3**	**G4**	**G5**
Coupling efficiency / %	~ 30	~ 25	~ 25	~ 25	~ 30	~ 28
Finesse	1.03×10^5	1.14×10^5	1.06×10^5	1.21×10^5	1.69×10^5	1.12×10^5

points from the ferrule reference. At the same time, all five grooves allow finesse values above 10^5 to be reached, with the measured finesse exceeding the ferrule reference for each groove. Both quantities therefore indicate that no substantial degradation of the achievable cavity performance due to the groove geometry is apparent within these measurements. Groove 4 in particular combines a coupling efficiency comparable to the ferrule reference with the highest measured finesse. The results therefore demonstrate that the Macor grooves are compatible with high-finesse cavity operation.

Based on these measurements for a single optical axis, the groove concept therefore appears promising. However, the measurements also showed that reproducible alignment requires the fibers to be held reliably at the deepest position of the grooves. The implementation of a suitable clamping mechanism was therefore a central requirement when extending the concept to the complete crossed-fiber assembly.

4.1.3 Additional Clamping

As discussed above, coated fibers in particular can exhibit sufficient stiffness that additional clamping is required to keep them positioned at the deepest point of the groove. An example of the best achievable alignment without additional clamping, recorded from the side using a USB microscope, is shown in Figure 4.5(a). The clamping material has to be sufficiently soft to avoid damaging the fibers, which are

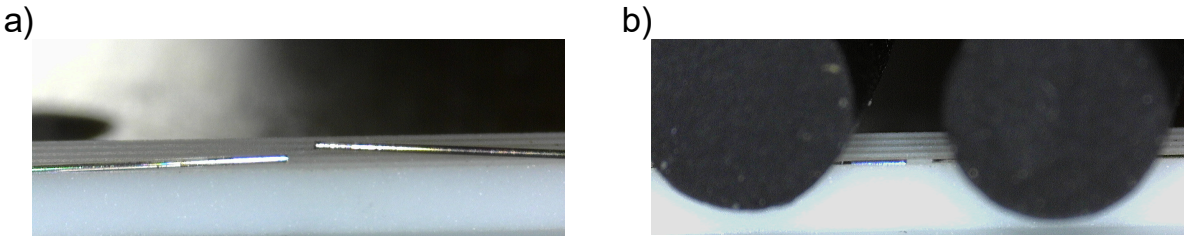


Figure 4.5: Microscope images of cavity fibers inserted into one of the grooves from the groove array used to evaluate the fabrication accuracy. (a) Side view of the best achievable fiber position without additional clamping. The fibers bend upwards due to their intrinsic stiffness, since no external pressure is applied. Further vertical adjustment of the fiber holders only increases the displacement of the fiber tips from the deepest position of the groove. This configuration therefore does not provide sufficiently stable positioning for cavity formation. (b) Side view of the cavity fibers while being pressed into the groove using Sorbothane rods attached to a clamp normally used for securing polarization cubes. The fibers are partially obscured by the groove, indicating that they are positioned deeper within it. With this additional clamping, the alignment was sufficient to form a stable cavity.

sensitive to lateral pressure and can break easily. At the same time, the fibers should be clamped as close as possible to the fiber tips to reliably keep them in the lowest position of the groove. However, a sufficient distance from the end facets has to be maintained, since the fibers were intended to be permanently fixed inside the grooves using UV-curable epoxy. Any epoxy leaking into the cavity region could contaminate the fiber mirrors and degrade the cavity performance.

The first clamping method was tested on a single optical axis using small pieces of a Sorbothane rod, which was also used for clamping the fibers in the holders employed during fiber-mirror fabrication, as described in Subsection 3.1.2. This successfully pressed the fibers into the grooves, as shown in Figure 4.5(b). However, Sorbothane exhibits comparatively high friction, which made it difficult to translate the fibers along the grooves without risking damage. Such translation is required to adjust the fiber-tip separation and scan the cavity length through resonance.

For this reason, the clamping material was changed to Teflon owing to its lower friction. For a single optical axis, this provided the desired combination of downward pressure and longitudinal mobility. A separate side-view image is not included, since the resulting fiber position is visually comparable to that obtained using Sorbothane. When extending the concept to two orthogonal optical axes, however, additional challenges became apparent.

First, the clamping structure restricted lateral optical access to the cavity region. A new clamping device was therefore fabricated with a central opening that provides optical access from above. Pieces of Teflon rod were attached to the underside of the structure and used to press the individual fibers into their corresponding grooves. The clamping device is shown in Figure 4.6. Panel (a) shows the top view, where the central opening allows the interaction region to be observed from above. Panel (b) shows a side view, where the Teflon rods attached to the underside of the clamping device are visible. A second difficulty was that the plane defined by the lower contact surfaces of the Teflon pieces was not perfectly parallel to the ceramic surface. As a result, different clamping forces were applied to the individual fibers. Although the softness of Teflon provides some tolerance against this misalignment, excessive pressure caused bending of the clamping structure. It therefore proved difficult to apply sufficient pressure to reliably position all fibers while avoiding deformation of the holder.

The identified clamping problem particularly affected the block design, since this concept relied on the fibers remaining positioned at the deepest point of the grooves while being fixed to the upper Macor

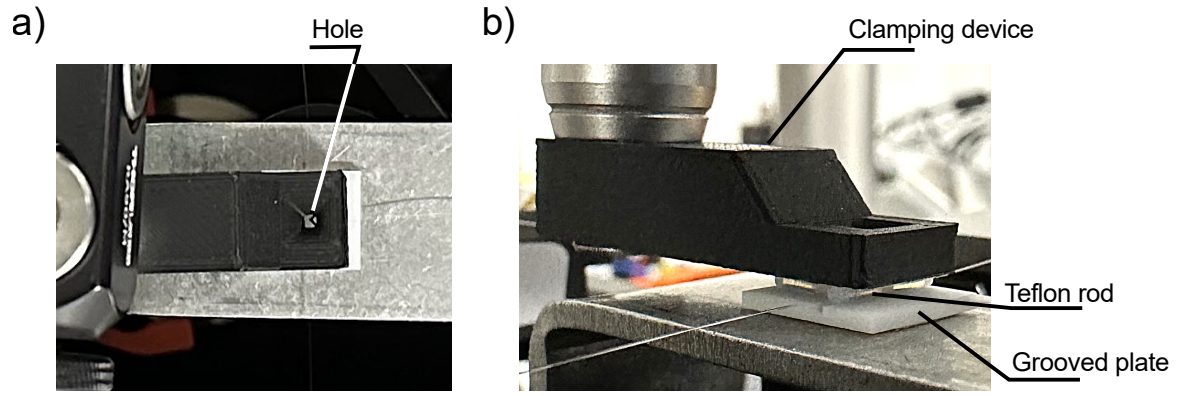


Figure 4.6: Microscope images of the clamping device mounted on the groove plate. (a) Top view showing the central opening, through which the interaction region can be observed using a USB microscope. (b) Side view showing the Teflon rods attached to the underside of the clamping device, which press the fibers into the corresponding grooves.

plates. As this could not be achieved reliably without an additional clamping structure, the block design was not investigated further.

The plate design, however, allowed the fibers to be pressed into the grooves during fixation and was therefore retained for subsequent alignment characterization described in Section 5.2. For this purpose, the plate was evaluated in its basic mechanical configuration without attached piezo elements, since the primary objective was to assess the achievable fiber alignment provided by the groove geometry itself.

Overall, the Macor-groove approach demonstrated that the lateral position of the fibers can be constrained mechanically using precisely fabricated grooves. However, the required machining accuracy, the need for an additional clamping structure, and the difficulty of applying a uniform clamping force to the fibers increased the complexity of the assembly. In addition, the achievable alignment depends directly on the fabrication tolerances of the individual grooves. These limitations motivated the investigation of a more integrated alignment concept based on 3D-printed ferrules, which is discussed in the following section.

4.2 3D-Printed Ferrules

4.2.1 Ferrule Concept and Design

In addition to the ceramic assembly concepts, 3D-printed ferrules were investigated as an alternative approach. Their design was inspired by conventional glass ferrules [20] and further developed from printed-ferrule concepts investigated in previous work [46].

The main purpose of the printed ferrules is to simplify and stabilize the alignment of the fiber tips. In the groove-based assembly concepts, additional clamping components are required to hold the fibers in position. In the printed ferrules, this additional clamping is avoided by guiding the fibers through enclosed channels, as illustrated in Figure 4.7. These channels constrain the lateral motion of the fibers and therefore define their relative positions and orientations within the central cavity region.

For the crossed-ferrule design, the centers of all four channels lie within the same plane and intersect at the center of the cavity region. The two optical axes are arranged orthogonally, similar to the

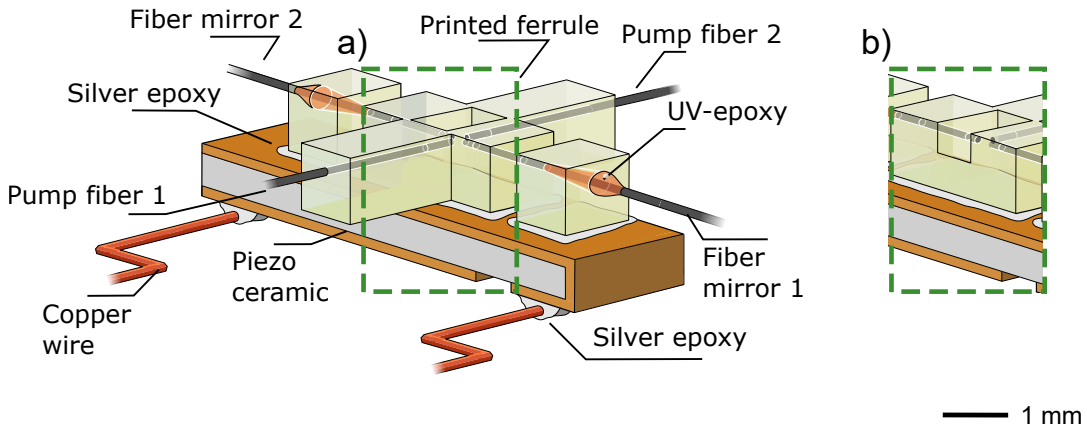


Figure 4.7: Sketch of the four-channel crossed-ferrule design. Each channel extends 4 mm from the central cavity region and is supported by a printed arm with a cross section of 1 mm × 1 mm. The plane containing the channel centers is shifted by 0.2 mm relative to the central plane of the ferrule. The central cavity region contains an opening with a cross section of 0.4 mm × 0.4 mm, providing optical access from above. Along the cavity axis, weakened connection regions are introduced into both arms. The ferrule is mounted using silver epoxy on a longitudinal piezo element, which changes its length when a voltage is applied. After cutting the weakened connection regions, the two sides of the cavity axis are mechanically separated. The cavity fibers are fixed only in the outer sections of the channels using UV-curable epoxy, allowing them to slide within the inner channel sections during piezo actuation. The outlined central regions show (a) the four-channel crossed ferrule and (b) the corresponding three-channel T-shaped ferrule, which omits one pump-fiber channel and thereby provides lateral optical access to the cavity region. Detailed dimensions of the ferrules are provided in Figure A.6 and Figure A.7 for the crossed and T-shaped ferrule, respectively.

groove-based design. Ideally, the geometry therefore aligns all four inserted fibers directly at the intended interaction region.

An additional opening in the central cavity region provides optical access from above. The plane containing the channel centers is positioned slightly above the central plane of the ferrule. This improves the visibility of the inserted fiber tips from above, similar to the geometry of conventional glass ferrules.

To enable tuning of the cavity length, the same basic principle as in [20] is applied, but using a printed ferrule instead of a glass ferrule. Weakened connection regions are introduced into the two arms defining the cavity axis. The ferrule is mounted along this axis onto a longitudinal piezo element with a length of 8 mm and a width of 2 mm. The ferrule is fixed to the piezo at three positions using silver epoxy, with one attachment point on each outer arm and one in the central region. Electrical connections are made by attaching wires to the piezo element.

After mounting, the weakened connection regions are cut through, mechanically separating the two outer arms of the cavity axis from the central region. The cavity fibers are fixed only in the outer sections of the channels using UV-curable epoxy, while the inner channel sections remain free. The cavity fibers can therefore slide within the channels when the piezo element expands or contracts. This relative displacement changes the separation of the two fiber mirrors and allows the cavity length to be scanned through resonance. The pump fibers are also fixed in the outer sections of their corresponding channels using UV-curable epoxy.

In addition to the four-channel crossed ferrule, a three-channel T-shaped ferrule, designed in previous work [46], was also investigated and further optimized with respect to its fabrication parameters. This

configuration accommodates only one pump fiber but provides additional lateral optical access to the cavity region, as indicated in Figure 4.7(b), making it particularly useful for evaluating the alignment accuracy and fabrication precision of the printed structures. As for the crossed ferrule, the centers of all three channels lie within the same plane and intersect at the intended interaction region. If fabricated with sufficient precision, both the crossed-ferrule and T-shaped-ferrule geometries should therefore provide the required alignment of the inserted fibers. Examples of a printed three-channel T-shaped ferrule and a four-channel crossed ferrule fabricated using optimized design and printing parameters are shown in Figure 4.8(a) and (b), respectively. A close-up of the central channel intersection of the four-channel crossed ferrule is shown in Figure 4.8(c).

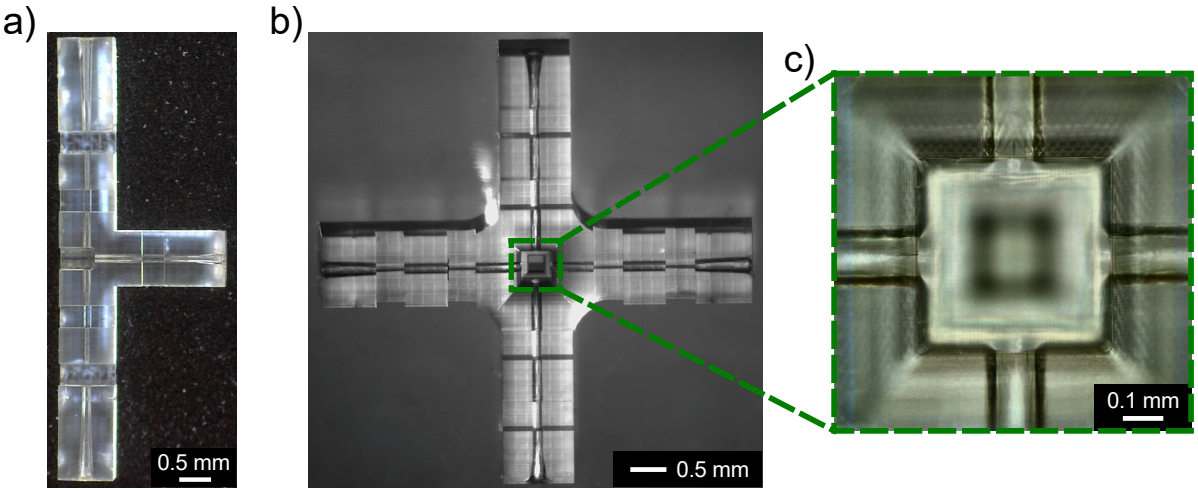


Figure 4.8: Microscope images of fabricated printed ferrules. (a) Overview of the complete three-channel T-shaped ferrule. (b) Overview of the complete four-channel crossed ferrule. (c) Close-up of the central region of the four-channel crossed ferrule, showing the intersection of the fiber channels and the intended interaction region.

One of the key advantages of fabricating the ferrules in-house is the flexibility to adapt their geometry to the specific requirements of the cavity, while remaining independent of external manufacturing services. The high-precision PPGT+ 3D printer, manufactured by Nanoscribe GmbH & Co. KG [47], enables the fabrication of structures with feature sizes down to a few hundred nanometers. This resolution is, in principle, sufficient for the ferrules developed in this work. However, their comparatively large dimensions on the millimeter scale require careful optimization of several printing parameters and design features. These considerations are discussed in the following sections.

4.2.2 Ferrule Fabrication

Unless stated otherwise, the specifications and technical descriptions of the DLW process using the PPGT+ system presented in this section are based on Ref. [48].

Direct Laser Writing with the PPGT+ System

The PPGT+ is a 3D printer based on direct laser writing (DLW). DLW utilizes two-photon polymerization (2PP), a nonlinear absorption process in a photosensitive resin. Polymerization is induced by a tightly focused femtosecond near-infrared laser, whose high peak intensity enables the simultaneous absorption

of two photons. The two-photon absorption rate scales quadratically with the laser intensity, while the total exposure at a given position additionally depends on the local exposure time. Together with oxygen-induced quenching effects, polymerization occurs only above a threshold intensity [49]. The corresponding iso-intensity surface of the polymerization threshold within the focal region defines the size and shape of the polymerized volume, commonly referred to as a voxel. Since the surrounding resin remains transparent at lower intensities, material polymerization is confined to this ellipsoidal volume. The two-photon absorption process and the dependence of the voxel size on the laser power are illustrated in Figure 4.9(b) and (c), respectively.

The PPGT+ System

The PPGT+ system consists of several components that are essential for understanding its operating principle. The laser beam is generated by a commercial femtosecond laser operating at a wavelength of 780 nm. It subsequently passes through two rotatable galvanometric mirrors, referred to as galvo mirrors, which control the propagation direction of the beam.

The beam is then focused into the photoresist, hereafter referred to as resin, using an interchangeable microscope objective. IP-S, provided by the manufacturer, was used as the resin throughout this work. The available objectives include a 63× objective with NA = 1.4, a 25× objective with NA = 0.8, a 20× objective with NA = 0.5, and a 10× objective with NA = 0.3. In this work, only the 25× objective was used, as its working range and resolution were best suited to the fabrication requirements. The following discussion therefore refers specifically to this objective.

An indium tin oxide (ITO)-coated substrate, or another suitable printing substrate covered with resin, is mounted upside down above the objective. The substrate holder can be translated relative to the objective, enabling the laser focus to be positioned within the resin. An additional piezoelectric stage, referred to as the piezo stage, provides high-precision positioning over a working range of 300 µm × 300 µm × 300 µm. Furthermore, a separate z-drive translates the objective holder relative to the substrate, enabling the fabrication of structures with heights of up to 8 mm. A schematic illustration of the system is shown in Figure 4.9 (a), in which only the piezo stage is indicated for simplicity. Due to the limited size of a single voxel, more complex structures are formed by connecting adjacent voxels into written lines and stacking successive layers. The lateral distance between adjacent written lines is referred to as the hatching distance (HD), while the vertical distance between successive layers is referred to as the slicing distance (SD). Both parameters are indicated in the enlarged section of Figure 4.9(a). Sufficient overlap in both directions is required to form a continuous structure. The values recommended in [48] are an HD of 0.5 µm and an SD of 0.6 µm. These values provided satisfactory printing results and were therefore used throughout this work.

Additionally, the PPGT+ can be operated in piezo mode, where the laser focus is positioned solely by movement of the piezo stage, or in galvo mode, where fast beam deflection by the galvo mirrors enables substantially shorter printing times at the cost of reduced precision at large deflection angles. Since the required accuracy for the structures fabricated in this work was still achieved in galvo mode, this faster operating mode was used throughout this work.

Shell-and-Scaffold Structures

Because the ferrules have millimeter-scale dimensions, printing them as fully solid structures would result in prohibitively long fabrication times. The shell-and-scaffold option was therefore investigated to

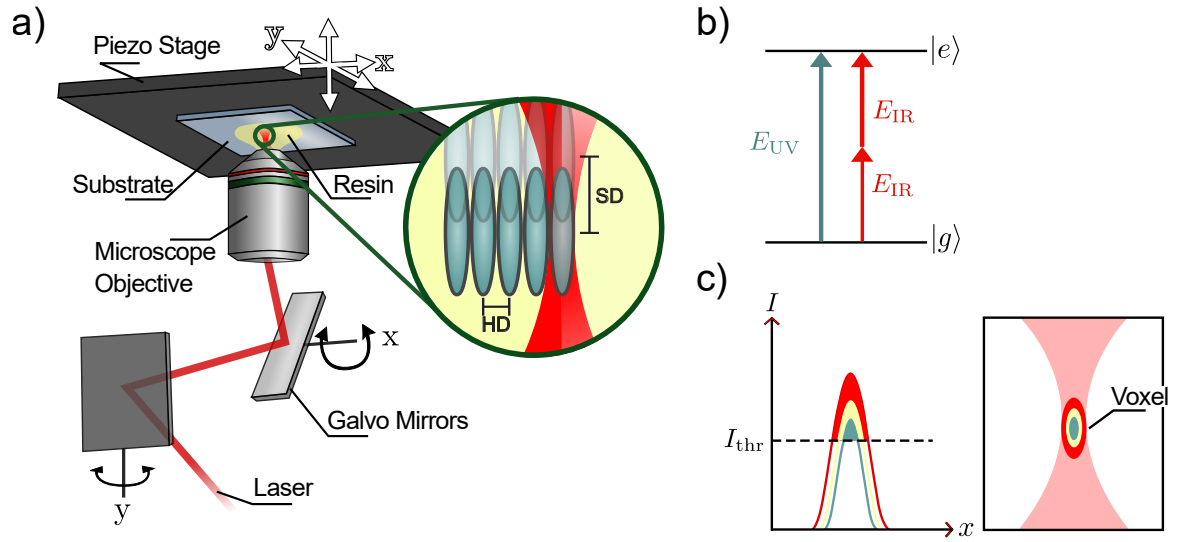


Figure 4.9: Schematic illustrations of the PPGT+ system and the physical principles underlying direct laser writing. (a) Sketch of the PPGT+ setup. The enlarged section which is adapted from [50] illustrates the hatching distance (HD) and slicing distance (SD), which define the lateral spacing between adjacent written lines and the vertical spacing between successive layers, respectively. (b) Simplified energy-level diagram comparing single-photon and two-photon polymerization. Here, E_{UV} denotes the photon energy required to induce polymerization by single-photon absorption, whereas E_{IR} corresponds to half this energy. Thus, the simultaneous absorption of two infrared photons provides the required excitation energy. (c) Laser intensity distribution at the focal region and the resulting polymerized voxel. The voxel boundary is defined by the iso-intensity surface at the polymerization threshold I_{thr}. Panels (b) and (c) are adapted from [48].

reduce the printing time while maintaining sufficient mechanical stability. Here, only the outer shell of the structure and an internal supporting lattice are polymerized, while the remaining volume is left unpolymerized. The spacing of the internal lattice, as well as the number of layers used for the lattice lines and the outer shell, can be adjusted. A denser lattice and a larger number of layers increase the printing time but also improve the mechanical stability of the structure.

To determine suitable lattice parameters, a sweep over different settings was performed, as shown in Figure 4.10. In all printed structures, the hexagonal pattern resulting from block splitting is visible. This effect is independent of the selected lattice parameters and will be discussed in the following section. An overview of the complete combined scaffold- and block-size sweep is provided in Figure A.2.

For the smallest lattice spacing, approximately 2 µm, shown in Figure 4.10(a), no individual lattice lines are visible, and the print appears as a homogeneous, fully polymerized structure. The polymer also appears slightly more yellow than in the other samples. Although the same laser power and scan speed were applied to all structures, the small spacing between adjacent lines results in a higher local exposure dose.

In Figure 4.10(b), where the lattice spacing is approximately 20 µm, the individual lattice lines can be clearly distinguished while still forming a dense supporting structure. For lattice spacings of approximately 200 µm, as shown in Figure 4.10(c), the lattice becomes mechanically unstable, with visible bending and partial collapse of the supporting lines.

Based on these results, a spacing of 20 µm was selected for the lateral lattice lines, referred to as walls, and a spacing of 25 µm for the vertical lattice lines, referred to as floors. With these values, the printed

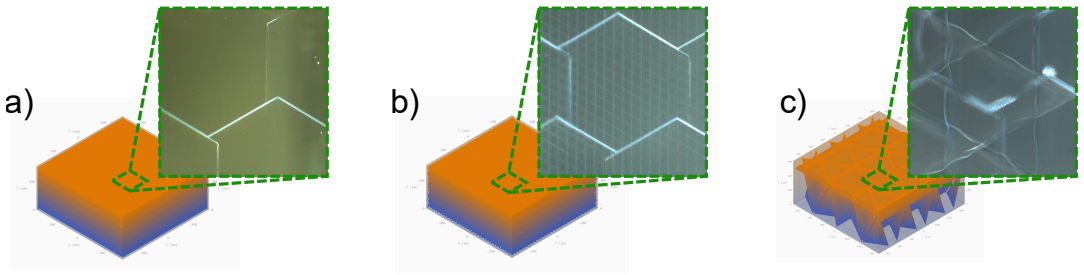


Figure 4.10: Comparison of different scaffold settings defined by the wall and floor spacing, corresponding to the lateral and vertical spacing of the scaffold, respectively. Each panel shows the corresponding STL model and an enlarged view of an approximately equal-sized region of the printed structure: (a) wall spacing of 2 µm and floor spacing of 2.5 µm, (b) wall spacing of 20 µm and floor spacing of 25 µm, and (c) wall spacing of 200 µm and floor spacing of 250 µm.

structures retained their intended shape while limiting the printing time of a typical four-channel crossed ferrule to approximately 30 h.

Block Splitting

For structures exceeding the writing field of the galvo mode, the geometry must be divided into individual printing blocks. Between adjacent blocks, the sample is repositioned using the piezo stage. Since repositioning with the piezo stage is considerably slower than beam deflection by the galvo mirrors, larger printing blocks reduce the overall printing time. However, increasing the block size also requires larger galvo deflection angles and can therefore reduce the fabrication quality.

To quantify the influence of large beam-deflection angles, a series of structures with different printing block sizes, hereafter referred to as block sizes, was fabricated, as shown in Figure 4.11. For comparison, each enlarged section displays an area of approximately the same size. The corresponding complete sweep is shown in Figure A.2.

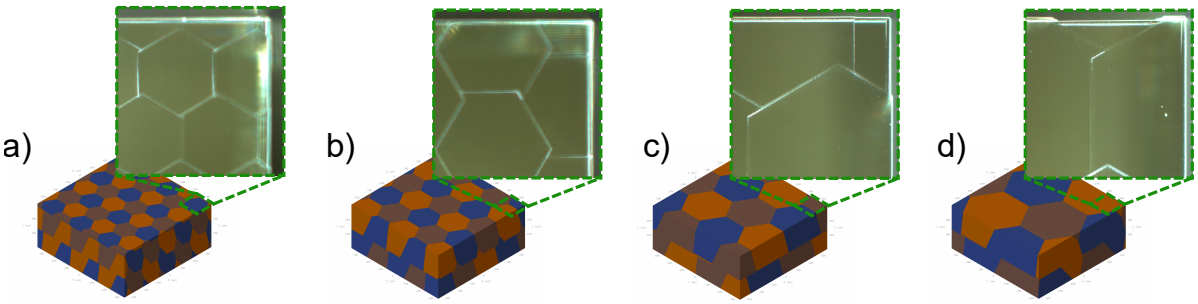


Figure 4.11: Comparison of different hexagonal block-size settings for a 700 µm × 700 µm × 380 µm test structure. Each panel shows the corresponding STL model and an enlarged view of an approximately equal-sized region of the printed structure. The block dimensions are specified as length × width × height: (a) 150 µm × 150 µm × 150 µm, (b) 200 µm × 200 µm × 200 µm, (c) 300 µm × 300 µm × 300 µm, and (d) 400 µm × 400 µm × 300 µm.

A slight stitching effect is visible at the boundaries between adjacent blocks, where material accumulates within the overlapping regions. For block sizes of up to 200 µm × 200 µm × 200 µm, shown in Figure 4.11(a) and (b), this effect remains comparatively small. For larger block sizes, shown in

Figure 4.11(c) and (d), the boundaries become increasingly irregular, and the edges of the printed structures appear less smooth and less uniform.

When a block is printed next to an already polymerized block, the incident laser beam may be partially obstructed or attenuated by the previously printed material. This is referred to as the shadowing effect. A schematic illustration is shown in Figure 4.12. To reduce this effect, the blocks are designed with a shear angle, which helps to keep the beam path unobstructed. A shear angle of 15° was selected and provided satisfactory results.

For the same reason, the structure is printed layer by layer, such that vertical repositioning occurs only between successive block layers. This movement can be performed using either the piezo stage or the z-drive. The z-drive is generally recommended because it reduces stitching errors between vertically adjacent layers. However, its lower translation speed leads to a considerable increase in printing time. Therefore, the vertical position was adjusted using the piezo stage in this work. The block offsets were chosen such that stitching boundaries did not occur in regions requiring particularly high precision, especially within the fiber channels of the ferrule. Based on these considerations, a block size of 160 µm × 160 µm × 160 µm was selected.

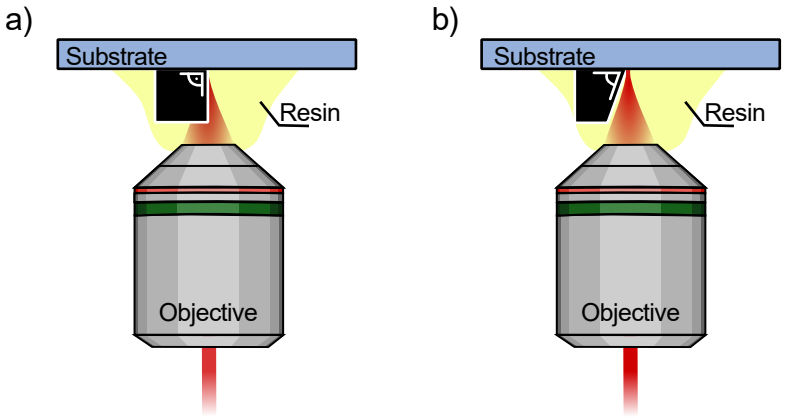


Figure 4.12: Schematic illustration of the shadowing effect for a block-shaped structure. For vertical sidewalls in (a), previously polymerized material partially obstructs the incident laser beam, reducing the intensity in lower regions of the structure. Introducing a shear angle in (b), such that the sidewall angle is smaller than 90°, reduces or prevents this effect.

Again, sufficient overlap between adjacent blocks and successive block layers must be ensured to prevent separation at their interfaces and to form a continuous structure. In both directions, the overlap was set to 2 µm.

4.2.3 Post-Processing

After printing, the structure remains covered with residual unpolymerized resin. To remove this material, development in propylene glycol monomethyl ether acetate (PGMEA) for approximately 20 minutes is recommended. While this duration is sufficient for less complex structures, previous work already indicated that it was not sufficient to completely remove the residual resin from the narrow fiber channels of the ferrules [46]. Increasing the development time to approximately 1 hour initially appeared to resolve this issue.

During the present work, however, a more detailed investigation of the printed ferrules showed that residual resin could still remain inside the channels even after this extended development time. This is illustrated in Figure 4.13(b), which shows a channel after a development time of 2 hours, while Figure 4.13(a) shows a fully flushed channel for comparison. The post-processing procedure and ferrule design were therefore further modified within this thesis in order to improve developer access and enable more complete flushing of the channels.

To increase the flow rate into the fiber channels, continuous stirring of the PGMEA during the development process was also tested. In a first attempt, the print was placed in a large beaker, leaving enough space to position the stirring device next to the print. However, this did not result in complete flushing of the channel after 2 hours, as can be seen in Figure 4.13(c). In a second attempt, a similar setup was used, but this time inside a smaller beaker, in which the print was suspended above the stirring device. In principle, this should have increased the flow around the printed structure. However, this approach also did not improve the flushing process, as shown in Figure 4.13(d).

For this reason, additional cuts extending towards the channels were introduced into the ferrule design in order to increase the accessibility of the developer. This enabled complete flushing of the channels in the case of the two-channel ferrule. However, for the three-channel and four-channel ferrules, this was still not sufficient. After various tests, a development time of 24 hours was found to be required for the four-channel crossed-ferrule design to show no visible residual unpolymerized resin, while 12 hours were sufficient for the three-channel T-shaped ferrule design. Complete flushing was assessed by microscope inspection after the subsequent curing step, during which any residual resin polymerizes and therefore becomes visible as uneven or partially blocked channel regions, as shown in Figure 4.13(b)–(d).

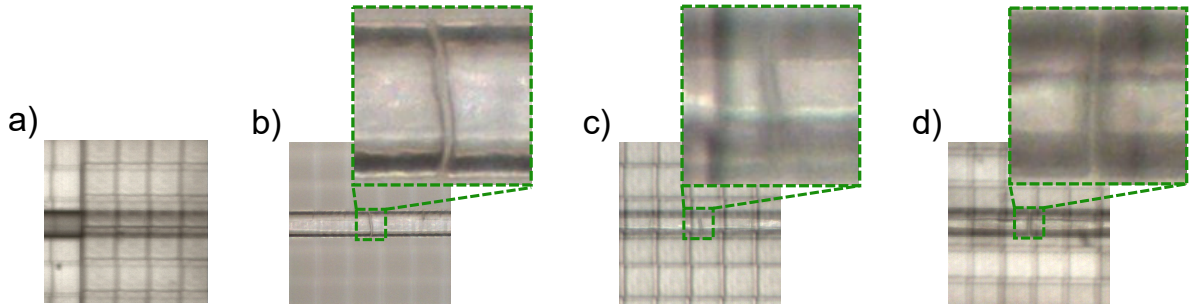


Figure 4.13: Results of different flushing approaches. For incompletely flushed channels, an enlarged view of the blockage is shown. (a) Fully flushed channel of a ferrule design with additional cuts. (b) Incompletely flushed channel after 2 hours in PGMEA without stirring. (c) Incompletely flushed channel after 2 hours in PGMEA with a stirring device placed next to the print (see Figure A.3(a)). (d) Incompletely flushed channel after 2 hours in PGMEA with a stirring device placed beneath the print (see Figure A.3(b)).

After the printed structure has remained in the developer long enough to remove the residual unpolymerized resin, the remaining PGMEA must also be removed because of its associated health and environmental hazards [51] and the potential risk of contaminating the fiber mirrors. For this purpose, the manufacturer recommends immersing the print in 2-propanol (IPA) for 15 minutes. With a viscosity of approximately 2.43 mPa s at 20 °C [51], IPA can be removed more easily from the channels than the unpolymerized resin, which has a viscosity of approximately (13 600 ± 200) mPa s [48] at the same temperature. For the ferrule structures investigated in this work, an immersion time of approximately one hour in IPA was required to remove the remaining PGMEA from the channels.

Finally, the printed structure is exposed to ultraviolet light while still immersed in IPA in order to

further cure the polymerized material and any residual resin enclosed within the scaffold.

4.2.4 Ferrule Shrinkage During Post-Processing

In addition to the challenges associated with flushing the channels, shrinkage of the printed structures must be considered during fabrication and development. Depending on the printing conditions and geometry, the structures can shrink by up to 12 % [48]. During polymerization, this shrinkage is mainly attributed to the increase in material density as the liquid resin is converted into the solid polymer. The structure may therefore continue to contract as the degree of polymerization increases.

Additional deformation can occur during development. The polymerized material may swell in the developer, while capillary forces during the subsequent drying process can cause further shrinkage or distortion [52]. To reduce these effects, the printed structures were UV-cured while still immersed in IPA, thereby postponing the drying process until the degree of polymerization had been increased. The structures were therefore exposed to UV light in IPA for one hour before being removed and dried. After being left to dry for one day, they were subsequently placed in an oven to promote further outgassing and drying of the structures, thereby reducing the risk of additional dimensional changes during subsequent testing and integration into the platforms.

In principle, shrinkage does not have to be isotropic. In particular, structures that remain attached to the substrate during development may exhibit anisotropic deformation. However, the ferrules investigated in this work generally detached from the substrate after approximately one to two hours in the developer. Since the total development time ranged from 12 to 24 hours, no pronounced anisotropic deformation was observed by microscope inspection after development, and the subsequent shrinkage therefore appeared to be approximately isotropic.

Suitable channel diameters were identified through a series of test prints with different nominal channel dimensions. A channel that is too narrow can be identified directly because the fiber cannot be inserted. Excessive clearance within the channel is more difficult to detect. To evaluate this, the fibers were inserted to their intended positions within the cavity region, and their lateral positions were varied slightly using the translation stages. If this did not produce visible lateral displacement of the fiber tips, but instead resulted mainly in a small pushing or pulling motion along the cavity axis, the channels were considered sufficiently tight to provide the required alignment.

Through this process, the nominal channel diameters were optimized to 144 µm for bare fibers and 154 µm for coated fibers. The bare fibers had a diameter of approximately 125 µm, while the coating increased the fiber diameter to an average of approximately 134 µm. The channel dimensions therefore had to be designed larger than the corresponding fiber diameters to allow reliable insertion while still sufficiently restricting lateral motion. In addition to shrinkage of the structure, the required difference between the nominal channel and fiber diameters is likely influenced by deviations of the printed channel surface from the ideal CAD geometry. The structure is formed from overlapping finite-sized voxels rather than from an ideally continuous boundary, which can introduce surface roughness and local dimensional variations. Variations in the local exposure dose due to overlapping written lines and layers may additionally contribute to these deviations. For fibers with substantially different tip diameters, the channel dimensions must be adjusted accordingly.

With the optimized printing parameters, the alignment provided by the printed ferrules could be evaluated with respect to their suitability for high-finesse fiber Fabry–Pérot cavities. Low-finesse cavities using printed ferrules had already been demonstrated in previous work [46], while their performance with high-finesse cavity fibers still required verification.

For this purpose, and similar to the assessment of the groove performance described in Subsection 4.1.2, several high-finesse fiber pairs were tested in printed two-, three-, and four-channel ferrules using the characterization setup described in Subsection 3.2.2, with the printed channels replacing the glass ferrule as the mechanical alignment structure. In all configurations, finesse values comparable to those obtained with conventional glass ferrules could be achieved. Since the cavity fibers were frequently damaged during the measurements and different fiber pairs therefore had to be used for several tests, a direct quantitative comparison between all ferrule geometries is not possible.

For a more direct comparison, the result obtained using a printed two-channel ferrule with the same fiber pair as used for the groove-array measurements is included in Table 4.3. This allows the influence of the different alignment structures to be compared under otherwise similar cavity conditions. As can be seen from the results, the printed ferrule reaches a finesse comparable to that obtained with the glass ferrule and the Macor grooves, while providing a higher coupling efficiency. This demonstrates that printed ferrules can support high-finesse fiber cavities with performance comparable to that obtained using glass ferrules or Macor grooves under the investigated conditions.

Table 4.3: Measured coupling efficiencies and corresponding cavity finesses obtained using the same fiber-mirror pair with different alignment structures. GF denotes the commercial glass ferrule with a specified channel diameter of 142 µm, G1–G5 denote the five nominally identical grooves fabricated from Macor, and PF denotes the printed two-channel ferrule. The target cavity length was approximately 100 µm for all measurements.

	GF	**G1**	**G2**	**G3**	**G4**	**G5**	**PF**
Coupling efficiency / %	~ 30	~ 25	~ 25	~ 25	~ 30	~ 28	~ 38
Finesse	1.03×10^5	1.14×10^5	1.06×10^5	1.21×10^5	1.69×10^5	1.12×10^5	1.14×10^5

4.3 Comparison of the Assembly Concepts

Overall, all investigated concepts demonstrated that mechanically predefined fiber alignment can support the formation of high-finesse cavities, but they differed considerably in their practical implementation. The initial Macor-based block concept was limited by the need to clamp the fibers while still allowing axial movement and was therefore not pursued further. The Macor-based groove plate avoided this problem by allowing sections of the supporting structure itself to be translated, but still required additional clamping of the fibers. For a final tunable crossed-cavity implementation, the sections supporting the opposing cavity fibers would additionally have to be separated mechanically to allow independent cavity-length adjustment.

With the fabrication and post-processing parameters optimized, the printed ferrules provided a more compact alternative in which the fiber positions are defined directly by enclosed channels, removing the need for an additional clamping structure in the central interaction region. The printed geometry can furthermore be adapted directly during the design process to include optical access, fiber movement, and interfaces for piezoelectric actuation. Together with the comparable finesse and higher coupling efficiency obtained in the direct comparison, this made the printed ferrule the most promising approach for the final implementation.

The remaining question for both the groove plate and the printed ferrules was whether the relative positions of the orthogonal fiber axes were sufficiently precise and reproducible to provide the intended

spatial overlap within the central interaction region. This was investigated experimentally using the alignment characterization methods introduced in the following chapter.

CHAPTER 5

Evaluation of the Assembly Platforms

To compare the alignment performance of the remaining assembly platforms, namely the Macor-based groove plate and the printed ferrules, suitable methods for determining the relative positions of the orthogonal fiber axes were required. The characterization methods developed for this purpose are introduced first in Section 5.1. The first method, discussed in Subsection 5.1.1, employs a rotating pillar inserted into the interaction region, for which both the working principle and the development of the method are described. The second method, presented in Subsection 5.1.2, is based on a conventional knife-edge measurement applied simultaneously to two orthogonally propagating beams.

After introducing the characterization methods, the predefined alignment achieved with the groove plate and the DLW-fabricated ferrules is evaluated in Section 5.2 and Section 5.3, respectively. The results of both assembly approaches are then compared at the end of the chapter.

5.1 Alignment Characterization Methods

While the alignment of two opposing grooves or channels along a single axis can be assessed comparatively easily by testing whether they support the formation of a high-finesse cavity, determining the relative alignment of two orthogonal axes, each defined by a pair of opposing grooves or channels, is more challenging.

For this characterization, fiber mirrors were not used, since the resulting cavity-mode position does not depend solely on the alignment provided by the grooves or channels, but also on the individual properties of the fiber mirrors. In particular, lateral or angular offsets of the laser-machined mirror depressions relative to the fiber axes can shift or tilt the cavity mode independently of the mechanical alignment imposed by the assembly structure.

Since these mirror-dependent contributions vary from one fabricated fiber mirror to another, the relative position of two cavity modes would contain contributions from both the assembly structure and the cavity geometry defined by the individual fiber mirrors. This would make it difficult to determine how accurately the crossed geometry is predefined by the assembly structure itself.

The aim was therefore to evaluate the alignment provided solely by the grooves or channels using freely propagating beams emitted from cleaved single-mode fibers. In previous work, a method was developed to evaluate the alignment of the pump-fiber channel relative to the probe-cavity axis in a three-channel T-shaped ferrule [46]. This method is briefly introduced in the following.

5.1.1 Rotating Pillar Method

The original method used to assess the alignment of the three-channel T-shaped ferrule employs a cylindrical pillar that is inserted into the optical beam path through the orthogonal pump-fiber channel. The method is described in detail in [46] and is therefore only summarized here.

A cleaved single-mode (SM) fiber is inserted into one of the two cavity-fiber channels. The fundamental fiber mode can be well approximated by a Gaussian field distribution and therefore propagates as an expanding Gaussian beam after leaving the fiber facet [53]. A multimode (MM) fiber is positioned in the opposing channel and collects the transmitted light. The core diameter of the MM fiber is chosen sufficiently large to collect most of the optical power at the selected separation from the SM fiber.

A cylindrical pillar with a diameter of approximately 50 µm is inserted into the beam path through the orthogonal pump-fiber channel. Depending on its rotational orientation, different parts of the transverse Gaussian intensity distribution are blocked, resulting in a corresponding variation of the optical power detected by the MM fiber. To relate this measured power variation to the relative position of the pillar and the optical axis, the expected transmission was calculated for different pillar positions and rotational orientations. For this purpose, the emitted field was modeled as a freely propagating Gaussian beam. The beam radius at a propagation distance of approximately 120 µm was determined from Equation 2.2. The pillar is represented as an opaque mask, and the transmitted power is obtained by integrating the remaining intensity distribution over the transverse plane.

Two rotational orientations of the pillar, illustrated in Figure 5.2(a) and (b), produce local maxima in the transmitted power that are equal in amplitude under ideal alignment. In these configurations, the pillar blocks approximately either the upper or the lower part of the Gaussian beam. The corresponding normalized peak intensities are denoted by I_1 and I_2.

The theoretical values of I_1 and I_2 depend mainly on two geometrical parameters. The first is the lateral offset d_l between the orthogonal pump-fiber axis and the cavity axis. The second is the offset d_p of the printed pillar relative to the center of the supporting fiber end facet. The latter has to be considered because the DLW fabrication process does not necessarily position the pillar perfectly concentrically on the fiber.

To separate the contributions of these two offsets, additional independent quantities are required. For this purpose, the sum and the absolute difference of the two peak intensities are evaluated,

$$I_+ = I_1 + I_2,$$

and

$$I_- = \left|I_1 - I_2\right|.$$

The quantities I_+ and I_- are calculated theoretically over a range of values for d_l and d_p. The experimentally obtained values are then compared with these calculated values. The combination of d_l and d_p giving the closest agreement provides an estimate of the lateral offset between the orthogonal pump-fiber channel and the cavity axis, while simultaneously accounting for an imperfectly centered pillar.

Pillar Fabrication

The pillar was designed to be fabricated by DLW directly on the end facet of a cleaved optical fiber. During the alignment measurement, the fiber carrying the pillar is inserted into the orthogonal pump-fiber channel. Provided that the pillar is printed concentrically on a sufficiently flat and well-cleaved fiber end facet, its position therefore represents the position of a fiber inserted into the orthogonal channel relative to the cavity axis.

Since the printed polymer transmits more than 90 % of the light at the operating wavelength of 1 550 nm [48], an additional coating was required to sufficiently block the probe beam. Two coating approaches were therefore tested: a thin metallic silver coating and a carbon-black coating. The resulting pillars are shown in Figure 5.1. An uncoated pillar is shown in (a) for comparison, while (b) and (c) show pillars coated with silver and carbon-black, respectively.

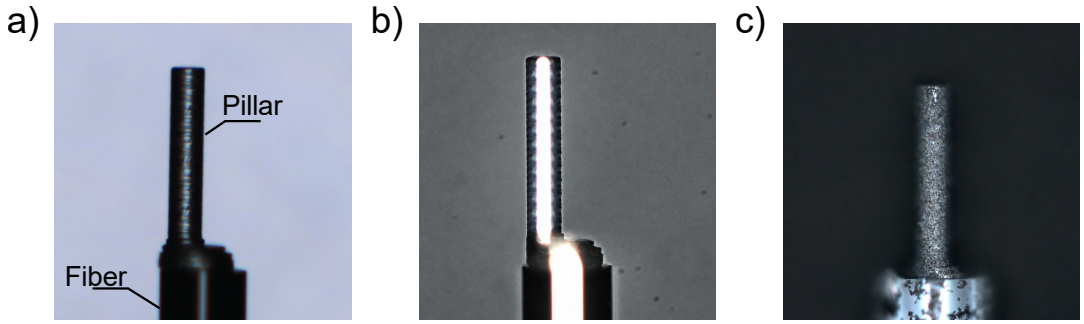


Figure 5.1: Microscope images of printed pillars on cleaved fiber end facets. (a) Uncoated pillar after development. (b) Pillar with a thin metallic silver coating. (c) A different pillar coated with a carbon-black dispersion.

Silver was selected because of its high reflectivity at the operating wavelength [54], while carbon-black was investigated because of its strong optical absorption [55] and small particle size of 10 to 20 nm [56], which allowed a comparatively uniform surface to be obtained after application. The silver coating was deposited using a physical vapor deposition system. A copper adhesion layer with a target thickness of approximately 1 nm was deposited first, followed by a silver layer with a target thickness of approximately 100 nm. Similar Cu adhesion layers are employed for the deposition of silver films in nanophotonic structures [57]. The deposition was performed using the evaporation system of the Nanophotonics group of Prof. Stefan Linden at the Physikalisches Institut, University of Bonn. An improvised holder allowed several pillar fibers to be coated simultaneously. No pronounced inhomogeneity of the coating was observed during microscope inspection, as shown in Figure 5.1(b).

For the carbon-black coating, a dispersion containing approximately 1 wt% carbon-black and 0.5 wt% PMMA in IPA was prepared. PMMA was used as a polymeric binder for the carbon-black particles, as commonly employed in carbon-black/polymer composite coatings [58]. The dispersion was mixed in an ultrasonic bath for 60 min at 40 °C to promote dispersion of the carbon-black particles and reduce agglomeration [59].

The individual pillar fibers were subsequently coated using a spin coater of the Nanophotonics group of Prof. Stefan Linden at the Physikalisches Institut, University of Bonn. A custom 3D-printed holder was fabricated to keep the fibers in position during the coating process. After applying a droplet of the carbon-black dispersion, the spin coater was operated at 500 rpm for 5 s, followed by 6 000 rpm for 90 s to distribute the dispersion across the pillar surface [60]. These parameters were selected based on

several preliminary coating tests.

A practical limitation became apparent for the carbon-black coating. Although the coating adhered to the pillar under normal handling, it could be rubbed off easily upon contact with another surface. This is particularly problematic for the intended cavity measurements, since accidental contact between the coated pillar and a fiber mirror could transfer carbon-black particles onto the mirror surface. Depending on their position, such contamination could introduce additional optical losses or even prevent the formation of a stable high-finesse cavity. For this reason, carbon-black-coated pillars were not used for the subsequent alignment measurements.

Measurement Procedure

The setup used for the rotating-pillar measurement is shown in Figure 5.2. A cleaved SM fiber and an MM fiber are inserted into the two opposing cavity-fiber channels. The SM fiber emits the probe beam into the interaction region, while the MM fiber collects the transmitted light. The fiber carrying the silver-coated pillar is inserted into the orthogonal pump-fiber channel and mounted in a rotational holder. A close-up of the interaction region during the measurement is shown in Figure 5.3(a). The

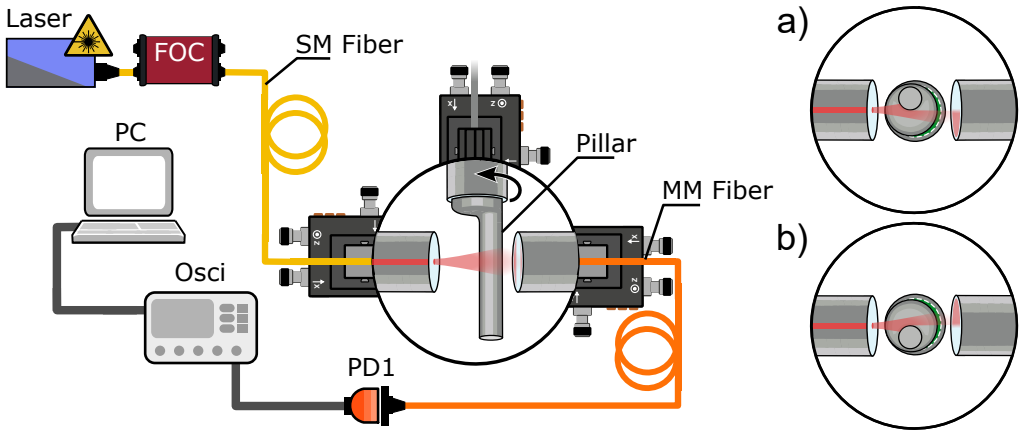


Figure 5.2: Setup for alignment evaluation using a rotatable pillar. Light from a laser operating at 1 550 nm is coupled through a 50/50 fiber-optical coupler (FOC) into a cleaved single-mode (SM) fiber inserted into one of the cavity-fiber channels. A multimode (MM) fiber positioned in the opposing channel collects the transmitted light and guides it to a photodiode, whose signal is recorded with an oscilloscope. A fiber carrying the fabricated pillar is inserted into the orthogonal pump-fiber channel and mounted in a rotational holder. Panels (a) and (b) illustrate the two pillar orientations corresponding approximately to local transmission maxima for ideal alignment. The green area outlined in white on the fiber surface carrying the pillar indicates the region that would be covered by a centrally positioned pillar. Since the fabricated pillar is not perfectly centered on the fiber surface, the actual pillar position is shifted relative to this reference region.

separation between the SM-fiber end facet and the center of the pillar fiber is adjusted to approximately 120 µm. The pillar fiber is then rotated through a full angular range while the optical power detected by the MM fiber is recorded. Measurements are taken in steps of 5°. The measured power is normalized to the transmitted power obtained without the pillar. The two local transmission maxima, corresponding approximately to the orientations shown in Figure 5.2(a) and (b), are determined by fitting the data in the vicinity of each maximum with a Gaussian function. This functional form provides a suitable empirical description of the measured transmitted power close to the maxima [61],

$$I(\theta) = I_{\text{off}} + A \exp\left[-\frac{(\theta - \theta_0)^2}{2\sigma^2}\right], \tag{5.1}$$

where θ_0 denotes the angular position of the maximum. The fitted peak values are used to determine I_1 and I_2. Examples of the measured angular dependence and the corresponding fits are shown in Figure 5.3(b) and (c).

The normalized maximum intensities I_1 and I_2 are subsequently used to calculate the experimental values of I_+ and I_-. These values are compared with the theoretical model described above in order to estimate the lateral alignment offset d_l and the pillar-center offset d_p.

The measurements shown in Figure 5.3(b) and (c) were performed using the same groove plate and the same groove positions for the fibers and the pillar in both measurements. To obtain approximately independent alignment conditions, the SM and MM fibers were recleaved and reinserted between the measurements, while the pillar fiber was also removed and repositioned. Despite the nominally identical geometry, the two measurements differ considerably.

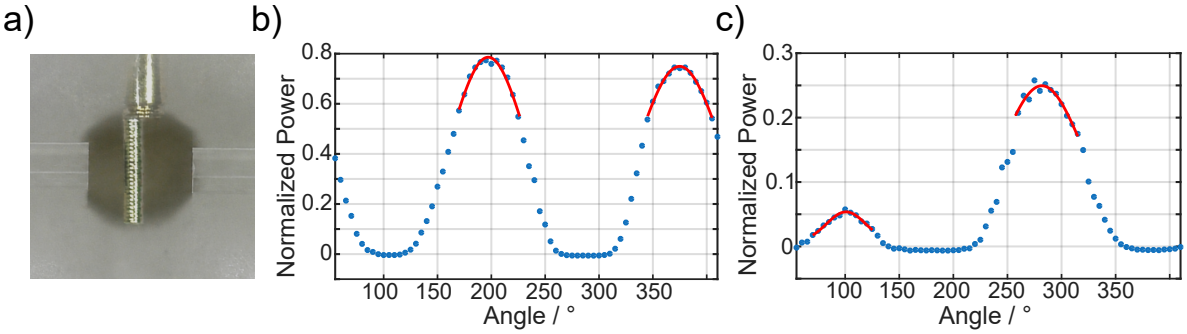


Figure 5.3: Image and measurement data obtained using the rotating-pillar method. (a) Microscope image of the interaction region, with an SM fiber inserted into the left groove and an MM fiber into the right groove. The silver-coated pillar is inserted into the upper orthogonal groove. The distance between the SM-fiber end facet and the center of the pillar fiber is approximately 120 µm. (b) Measured transmitted optical power as a function of the pillar rotation angle in steps of 5°. The power is normalized to the transmitted power measured without the pillar and is shown by the blue data points. A relative measurement uncertainty of 2 % was assumed for the measured power values but is not shown in the plot. The local transmission maxima are determined by fitting the data in the vicinity of each maximum using the Gaussian function given in Equation 5.1. The corresponding fits are shown as red lines. (c) Repeated measurement with the same procedure as (b) after recleaving and reinserting the SM and MM fibers and repositioning the pillar fiber.

For the first measurement, shown in Figure 5.3(b), the extracted offsets were approximately $d_l \approx 0.1$ µm and $d_p \approx 8$ µm. For the second measurement, shown in Figure 5.3(c), values of approximately $d_l \approx 0.3$ µm and $d_p \approx 72$ µm were obtained. While the estimated lateral alignment offsets are of a similar order of magnitude, the second value obtained for d_p is clearly unphysical. An offset of approximately 72 µm would place the center of the pillar outside the fiber end facet.

The inconsistency indicates that the rotating-pillar method did not provide reproducible alignment estimates under the conditions investigated here. One possible source of error is a persistent bending or curvature of the pillar fiber, potentially influenced by the additional metallic coating. In this case, the pillar is displaced from the mechanical rotation axis and therefore follows a circular trajectory during rotation rather than rotating approximately around the fiber axis fixed by the groove plate or ferrule. The

resulting apparent displacement depends on the magnitude and direction of the fiber-tip bending and is not included in the theoretical model.

Because this additional uncertainty could not be quantified reliably, the rotating-pillar method was not used for the subsequent alignment evaluation. Instead, further work focused on developing alternative characterization methods with improved reproducibility.

5.1.2 Knife-Edge Method

After the rotating-pillar method was found to be insufficiently reproducible, an alternative approach based on the well-established knife-edge method for characterizing Gaussian beams was investigated [62–64]. Again, a cleaved single-mode (SM) fiber is used to generate an expanding Gaussian beam [53], while a multimode (MM) fiber positioned opposite to it collects the transmitted light.

In contrast to the rotating-pillar method, an SM–MM fiber pair is positioned along each of the two orthogonal optical axes. The two SM fibers therefore generate two orthogonally propagating Gaussian beams whose centers within the interaction region are determined by the alignment provided by the grooves or ferrule. The transmitted optical power along both axes is measured simultaneously while an opaque blocking element is translated vertically into the interaction region, perpendicular to the plane spanned by the two optical axes.

As the blocking element passes through the two beams, the transmitted power decreases according to the transverse intensity distribution of each beam [62, 65]. The center positions of the corresponding transitions therefore provide estimates of the beam-center positions along the scanning direction. Comparing these positions for the two orthogonal beams allows their relative lateral alignment, and consequently the alignment provided by the corresponding grooves or channels, to be assessed.

For a Gaussian beam, the resulting knife-edge signal corresponds to the integrated transverse intensity distribution and exhibits an error-function-shaped transition [66],

$$I(x) = I_{\mathrm{off}} + \frac{A}{2}\left[1 \pm \operatorname{erf}\left(\frac{x - x_0}{\sqrt{2}\sigma}\right)\right], \tag{5.2}$$

where the sign is chosen according to the scanning direction and orientation of the blocking edge. The parameter x_0 corresponds to the beam-center position along the scanning direction, while the Gaussian beam radius is given by $w = 2\sigma$ for the intensity convention used in this work.

Knife-Edge Device

Finding a suitable blocking element for the knife-edge measurement proved more challenging than initially expected. The main limitation was the small available interaction region. The blocking element had to fit between all four SM and MM fiber tips and should therefore occupy an area of no more than approximately 125 µm × 125 µm when inserted into the central region. At the same time, the separation between the opposing SM and MM fibers should remain comparable to the cavity lengths targeted for the final assembly, such that larger distances between the fiber tips were avoided.

The blocking element therefore had to combine a small size with a nearly straight edge and high opacity at the operating wavelength of 1 550 nm. A well-defined, sharp edge is particularly important because deviations from an ideal knife-edge geometry can introduce artifacts in the measured beam profile and alter the expected error-function dependence of the transmitted power [67].

When searching for a suitable commercially available knife edge, no appropriate and readily available component could be found. Most commercially available knife edges were either too large for the limited interaction region or already integrated into beam-characterization devices. This motivated the search for a suitable object whose original purpose was different but which could be adapted for use as a knife edge.

The first object considered was a cleaved fiber end. However, because the fiber end facet provides a comparatively large surface, the use of a reflective coating, such as silver, could lead to parts of the incident beam being reflected from the fiber surface. These reflections would introduce additional effects that are not accounted for by the simple knife-edge model and could therefore require a more complex theoretical description. An absorbing coating was consequently considered more suitable. As a first test, a cleaved fiber end coated with the previously described carbon-black dispersion was therefore used as the blocking element. In contrast to the rotating pillar, the cleaved fiber does not, in principle, need to come into contact with the alignment structure or the fiber surfaces during the measurement.

In practice, however, positioning the blocking element within the interaction region proved difficult, and occasional contact with the alignment structure during insertion could not be avoided. This mechanical contact caused parts of the carbon-black coating to be removed, as had already been observed for the carbon-black-coated pillars.

An example is shown in Figure 5.4(a). While most of the fiber surface remains covered by the visibly grainy carbon-black layer, part of the surface became transparent after the fiber scraped against the ceramic plate while testing the coated fiber tip as a knife edge on the grooved ceramic plate. Consequently, light could pass through these uncoated regions during the knife-edge scan.

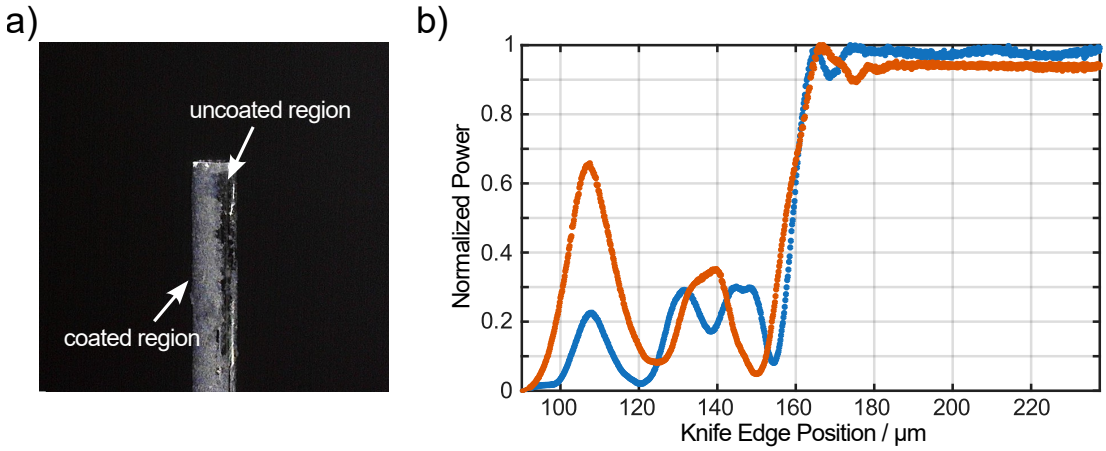


Figure 5.4: Image and measurement data obtained using the knife-edge method with a partially carbon-black-coated fiber. (a) Microscope image of the coated fiber end. Most of the surface remains covered by the carbon-black coating, while one side became partially transparent after mechanical contact with the ceramic plate during insertion. (b) Simultaneously measured transmitted power along the two orthogonal optical axes, shown in blue and orange, as a function of the knife-edge position. The transmitted powers of both optical axes are normalized by the maximum power measured across both data sets. The scan proceeds from a predominantly blocked towards an unblocked configuration. Pronounced fluctuations that are inconsistent with the expected error-function dependence are visible, particularly within the nominally blocked region.

The resulting measurement is shown in Figure 5.4(b), where the two color-coded data sets correspond to the two orthogonal optical axes. The blocking element was scanned from a predominantly blocking position towards an unblocked configuration. For an ideal opaque knife edge, the transmitted power

should remain close to zero while the beam is completely blocked and subsequently increase smoothly according to Equation 5.2. Instead, pronounced fluctuations were observed in the nominally blocked region. These are attributed to light transmitted through the partially uncoated areas of the fiber. Additional fluctuations are visible as the fiber leaves the beam path, which may result from reflections at exposed regions of the cleaved fiber end facet.

Because of this unstable optical behavior and the unavoidable risk of contact between the fiber tip and the alignment structure, which could additionally contaminate the assembly with carbon-black particles, the coated fiber was not considered suitable for further knife-edge measurements.

Following this test, an additional requirement for the blocking element became apparent. Positioning takes place on the micrometer scale, and inaccurate insertion can easily result in contact with a fiber, the groove plate, or the ferrule. The blocking element should therefore be mechanically robust and readily available or replaceable in case of damage.

This requirement also excluded the possibility of printing a knife-edge-like structure onto a fiber end facet and subsequently coating it with silver, since the fabrication and coating procedure requires several days to complete.

Based on these requirements, a commercially available tungsten cleaning wire from Thorlabs was investigated as an alternative blocking element. The wire, normally intended for cleaning fiber ferrules, has a manufacturer-specified diameter of approximately 110 µm [68] and is therefore sufficiently small to be inserted into the interaction region. Since the optical penetration depth of tungsten at the operating wavelength is only on the order of several tens of nanometers, the thickness of the tungsten blocking element is sufficiently large for it to be considered effectively opaque [54]. Consequently, no additional absorbing coating is required.

Microscope inspection additionally showed that the individual wire pieces are cut at an angle, producing an approximately straight edge suitable for a knife-edge measurement, as shown in Figure 5.5(b). The resulting flat region has a width of approximately 90 µm. By orienting this edge at approximately 45° relative to the two SM-fiber axes, it can be translated through both Gaussian beams during the scan. Initial measurements showed the expected smooth transition between blocked and transmitted optical power, as shown in Figure 5.6, indicating that the tungsten wire is substantially better suited to the knife-edge measurement than the carbon-black-coated fiber.

Measurement Procedure

The setup used for the knife-edge measurement is shown in Figure 5.5(a). One SM–MM fiber pair is inserted along each of the two orthogonal optical axes. Light from the same laser source is split using a 50/50 fiber-optical coupler and coupled into the two SM fibers, which emit orthogonally propagating Gaussian beams into the interaction region. The corresponding MM fibers positioned on the opposite sides collect the transmitted light.

The tungsten wire is mounted on a rotational holder, allowing the orientation of its flat edge relative to the two SM fibers to be adjusted. The holder is mounted on a motorized translation stage (8MT167M-25LS) from STANDA [69] with a minimum step size of 0.156 µm. The wire is inserted perpendicular to the plane spanned by the two optical axes, with its edge positioned approximately 30 µm from each SM-fiber end facet at the center of the interaction region. During the measurement, the wire is translated through the two beams in steps of 0.156 µm while the transmitted power along both optical axes is recorded simultaneously. This corresponds to the smallest possible step size of the motorized translation stage and was chosen to provide the highest available spatial resolution for resolving the expected

error-function dependence. The transmitted powers of both optical axes are normalized by the maximum power measured across both data sets, thereby preserving their relative amplitudes while leaving the extracted values of x_0 and w unaffected. Each color-coded data set, shown in blue or orange, therefore corresponds to one optical axis.

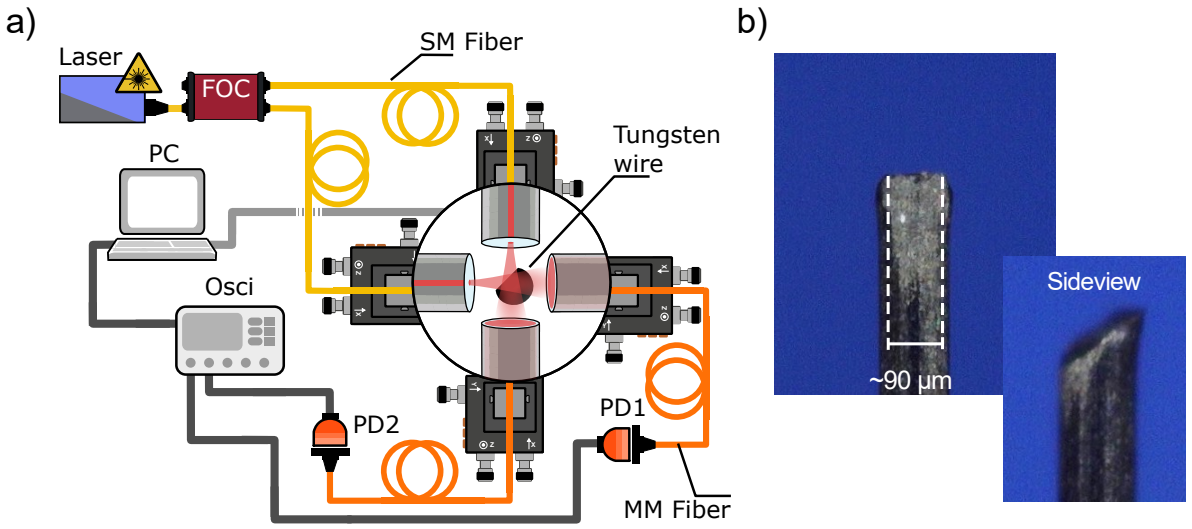


Figure 5.5: (a) Setup for alignment evaluation using the knife-edge method. Light from a laser operating at 1 550 nm is divided by a 50/50 fiber-optical coupler (FOC) and coupled into two SM fibers inserted along the two orthogonal optical axes. Opposing MM fibers collect the transmitted light, which is detected and recorded with an oscilloscope. A tungsten wire is inserted perpendicular to the plane spanned by the two optical axes. Its flat edge is oriented at approximately 45° relative to both SM-fiber axes and translated through the interaction region in steps of 0.156 µm while the transmitted power along both axes is monitored simultaneously. (b) Microscope image of a tungsten cleaning wire tip. The angled cut produces an approximately flat edge with a width of about 90 µm, which is used as the knife edge.

Using the known displacement of 0.156 µm between successive measurement points, Equation 5.2 is fitted independently to the data obtained along both optical axes. At each knife-edge position, the detector signal was averaged over a fixed acquisition interval. The uncertainty in the transmitted power was estimated for each trace from the standard deviation of the measured values within the plateau region of the knife-edge scan, where the transmitted power is expected to remain constant [70, 71].

For the example shown in Figure 5.6(a), reduced chi-squared values of approximately $\chi^2_{\mathrm{red}} = 2.9$ and $\chi^2_{\mathrm{red}} = 5.0$ were obtained for the two fits. As these values are above unity, this indicates that the deviations between the measured data and the ideal error-function model are larger than expected from the assigned uncertainties alone [61]. One possible contribution is the comparatively long measurement duration of more than one hour, during which slow variations of the laser power and additional low-frequency noise can occur. Since these effects are not fully represented by the uncertainty estimated from the plateau fluctuations, the experimental uncertainties may be underestimated. Nevertheless, the measured data follow the expected error-function dependence sufficiently well, and the fits were therefore considered suitable for extracting the beam-center positions.

The fits yield estimates of the two beam-center positions $x_{0,1}$ and $x_{0,2}$. Their relative displacement along the scanning direction is then given by

$$d = \left|x_{0,1} - x_{0,2}\right|,$$

with the corresponding uncertainty obtained by Gaussian error propagation

$$\Delta d = \sqrt{(\Delta x_{0,1})^2 + (\Delta x_{0,2})^2}.$$

The absolute positions of the two beams are not calibrated, since only their relative displacement is relevant for evaluating the alignment of the two optical axes. The fitted beam radii are additionally used as a consistency check. Since the beam radius at the knife-edge position depends on the propagation distance from the corresponding SM-fiber end facet, which can only be estimated from microscope images with limited resolution, the extracted radii are not used as the primary alignment quantity.

An additional contribution to the measured beam displacement results from non-zero cleave angles of the SM fibers. The knife-edge measurement determines the positions of the propagating beam centers rather than directly measuring the geometrical positions of the fiber cores. A tilted fiber end facet can refract the emerging beam and thereby shift its center at the position of the knife edge.

For a fiber with refractive index n and a cleave angle α, Snell's law gives [72] $n \sin(\alpha) = \sin(\theta_t)$, where θ_t is the transmitted angle relative to the surface normal. The resulting propagation angle relative to the original fiber axis is therefore

$$\theta_{out} = \theta_t - \alpha = \arcsin(n \sin \alpha) - \alpha.$$

For small cleave angles, this can be approximated by $\theta_{out} \approx (n - 1)\,\alpha$.

After a free-space propagation distance L, the corresponding lateral displacement of the beam center is

$$\Delta x = L \tan(\theta_{out}).$$

As a worst-case estimate, a cleave angle of $\alpha = 0.9^\circ$ is considered, corresponding to the upper end of the average cleave-angle range specified for the Fujikura CT50 fiber cleaver [73]. Using $n \approx 1.45$ and a propagation distance of $L = 30\,\mu\text{m}$ gives

$$\Delta x \approx 0.21\,\mu\text{m}.$$

If both SM fibers exhibit cleave angles of 0.9° that deflect the beams in opposite directions along the knife-edge scanning axis, the resulting contribution to their measured relative displacement can therefore reach approximately $0.42\,\mu\text{m}$. This value represents a worst-case estimate; for smaller cleave angles or for deflections that are not fully oriented along the scanning direction, the resulting contribution is correspondingly smaller.

As an additional consistency check, knife-edge scans were performed in both translation directions. A representative comparison is shown in Figure 5.6. For the forward scan, a relative beam-center displacement of $d = (0.49 \pm 0.03)\,\mu\text{m}$ was obtained, while the backward scan yielded $d = (0.47 \pm 0.03)\,\mu\text{m}$. The two values therefore agree within their experimental uncertainties.

The fitted beam radii were also compared between the two scan directions. For the optical axis represented by the blue data points and the corresponding red fit, beam radii of $(7.12 \pm 0.05)\,\mu\text{m}$ and $(7.07 \pm 0.05)\,\mu\text{m}$ were obtained for the forward and backward scans, respectively. For the orthogonal optical axis, represented by the orange data points and the corresponding green fit, the respective radii

were (5.50 ± 0.04) µm and (5.52 ± 0.03) µm. The difference in beam radius between the two optical axes is consistent with the slightly different distances between the respective SM-fiber end facets and the knife edge. Within each optical axis, however, the radii obtained for the two scan directions agree within their experimental uncertainties.

The agreement of both the relative beam-center displacement and the individual beam radii indicates that no pronounced scan-direction-dependent bias affects the knife-edge measurement.

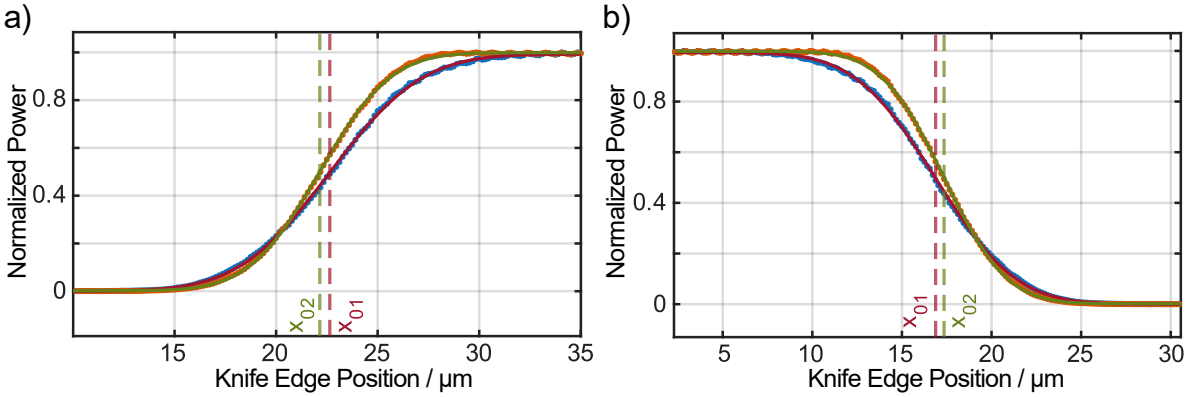


Figure 5.6: Representative forward and backward knife-edge measurements obtained using the four-channel crossed ferrule. The transmitted power along the two orthogonal optical axes, shown in blue and orange, is fitted according to Equation 5.2. (a) Forward scan from a fully blocked towards an unblocked configuration, yielding a relative beam-center displacement of $d = (0.49 \pm 0.03)$ µm. The fitted beam radii are (7.12 ± 0.05) µm and (5.50 ± 0.04) µm for the blue and orange data, respectively. (b) Backward scan from an unblocked towards a fully blocked configuration, yielding $d = (0.47 \pm 0.03)$ µm. The corresponding fitted beam radii are (7.07 ± 0.05) µm and (5.52 ± 0.03) µm. No fibers or optical components were repositioned between the two measurements. The absolute knife-edge positions are referenced to the starting position of each scan and are therefore not directly comparable between panels.

Based on the promising results of these test measurements, the alignment achieved with the individual assembly platforms was subsequently assessed using the knife-edge method with the tungsten wire.

5.2 Grooved Ceramic Holder Assembly

For the evaluation of the grooved ceramic holder, the SM and MM fibers were inserted into the corresponding grooves and pressed into position using pieces of Teflon rod attached to a 3D-printed clamping device. An opening in the clamping device provided optical access to the central interaction region from above, shown in the enlarged region of Figure 5.7(a). The tungsten wire was inserted from below through the central V-shaped opening of the groove plate, visible in Figure 4.3(a) and (b).

During insertion and throughout the measurement, the position and orientation of the tungsten wire were monitored from above using a microscope camera. This allowed the flat edge of the wire to be aligned relative to the two optical axes. Top and side views of the resulting setup are shown in Figure 5.7(a) and (b), respectively.

To assess the reproducibility of the alignment produced through the groove plate, six independent measurements were performed. Between successive measurements, the SM and MM fibers were recleaved, repositioned, and reclamped, while the tungsten wire was also removed and repositioned.

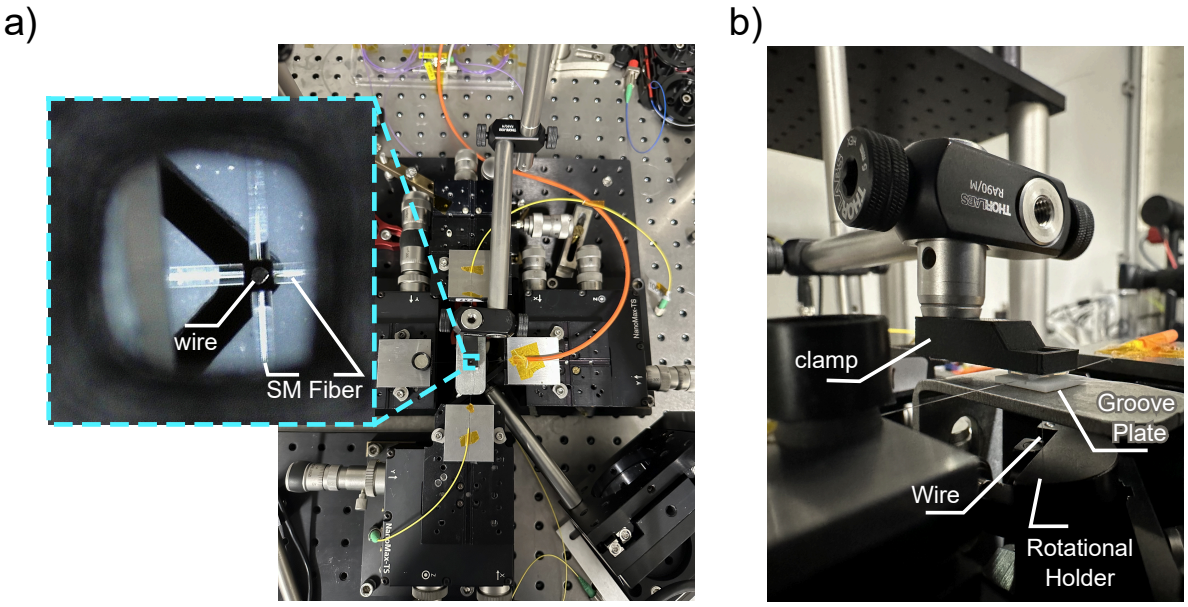


Figure 5.7: Images of the setup described in Figure 5.5 as employed for evaluating the grooved ceramic holder. (a) Top view of the setup. The enlarged region shows the central interaction area observed through the opening in the clamping device. The straight edge of the tungsten cleaning wire is visible as a bright line and was positioned approximately 30 µm from the SM-fiber end facets. (b) Side view of the setup. The tungsten wire is inserted from below and mounted in a rotational holder. The clamping device and the Teflon rods pressing the fibers into the ceramic grooves from above are also visible.

The extracted displacements between the two beam-center positions are summarized in Table 5.1.

Table 5.1: Relative beam-center displacements determined for the grooved ceramic holder using the knife-edge method. Six independent measurements were performed, with the fibers recleaved, repositioned, and reclamped between successive measurements.

	It. 1	**It. 2**	**It. 3**	**It. 4**	**It. 5**	**It. 6**
Displacement / µm	(2.76 ± 0.04)	(2.61 ± 0.05)	(3.09 ± 0.06)	(1.97 ± 0.09)	(0.78 ± 0.05)	(0.09 ± 0.05)

The measured values range from approximately 0.09 µm to 3.09 µm, with an average displacement of approximately 1.88 µm over the six measurements.

The observed variation is considerably larger than the contribution expected from the cleave angles of the SM fibers. As discussed previously, even cleave angles of 0.9° in opposite directions would contribute only approximately 0.42 µm to the relative beam displacement for the propagation distance used here. The variation between repeated measurements is therefore more likely associated with the positioning and clamping of the fibers within the grooves.

For each iteration, the fibers were recleaved, repositioned, and reclamped. The clamping pressure was adjusted experimentally until a high transmitted power was obtained along both optical axes in the absence of the knife edge. However, this procedure does not provide direct information about whether all four fibers are positioned at the deepest point of their respective grooves. Small differences in the

applied clamping force can therefore result in different fiber positions and consequently different relative beam-center positions.

The smallest measured displacement of (0.09 ± 0.05) µm shows that the groove geometry can, in principle, support very precise relative alignment of the two optical axes. However, displacements of up to approximately 3 µm were obtained under nominally identical assembly conditions. The limiting factor of the groove-plate approach is therefore not primarily the achievable alignment itself, but its reproducibility when the fibers have to be positioned and clamped manually. Representative measurements yielding displacements of (0.09 ± 0.05) µm and (3.09 ± 0.06) µm are shown in Figure 5.8.

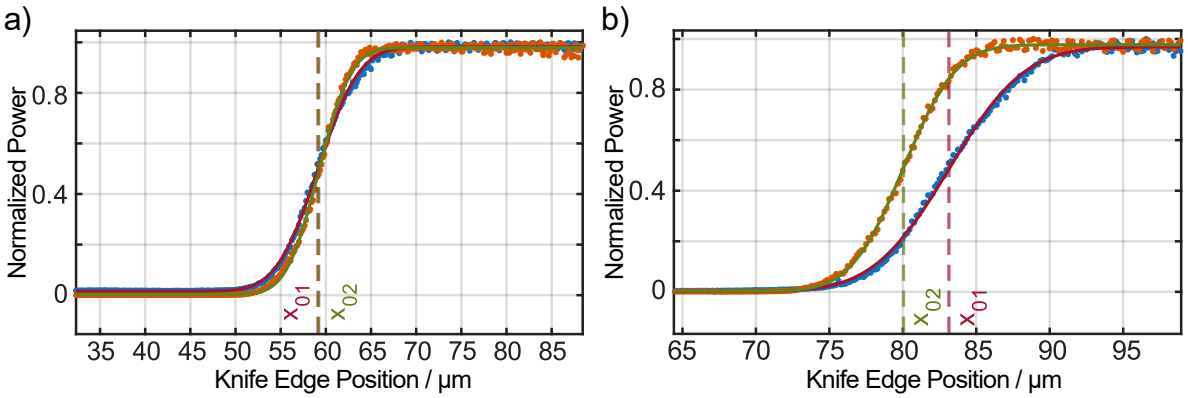


Figure 5.8: Example knife-edge measurements obtained for the grooved ceramic holder. The transmitted power along the two orthogonal optical axes, shown in blue and orange, is fitted according to Equation 5.2. (a) Measurement yielding a relative beam-center displacement of $d = (0.09 \pm 0.05)$ µm. At maximum transmission, a slight drift in the laser power is visible. (b) Measurement yielding $d = (3.09 \pm 0.06)$ µm. Both measurements were performed using the same groove plate, with the fibers recleaved, repositioned, and reclamped between the measurements.

5.3 3D-Printed Ferrule Assembly

After evaluating the grooved ceramic holder, the same knife-edge method was applied to the 3D-printed ferrules to assess how precisely the printed channels define the relative positions of the orthogonal fiber axes. In contrast to the groove plate, the fibers are laterally constrained directly by the printed channels and therefore do not require an additional clamping structure within the interaction region. Here, the tungsten wire was inserted from above, while the orientation of its flat edge was adjusted before lowering it between the fiber tips. An image of the setup is shown in Figure 5.9. The enlarged regions show close-up views of the interaction regions of the four-channel crossed ferrule and the three-channel T-shaped ferrule.

5.3.1 Assessment of the Four-Channel Crossed Ferrule

First, the four-channel crossed ferrule was evaluated using the knife-edge method. Similar to the groove-plate assessment, six independent measurements were performed. Between successive measurements, the SM and MM fibers were recleaved, removed, and reinserted, while the tungsten wire was also removed and repositioned.

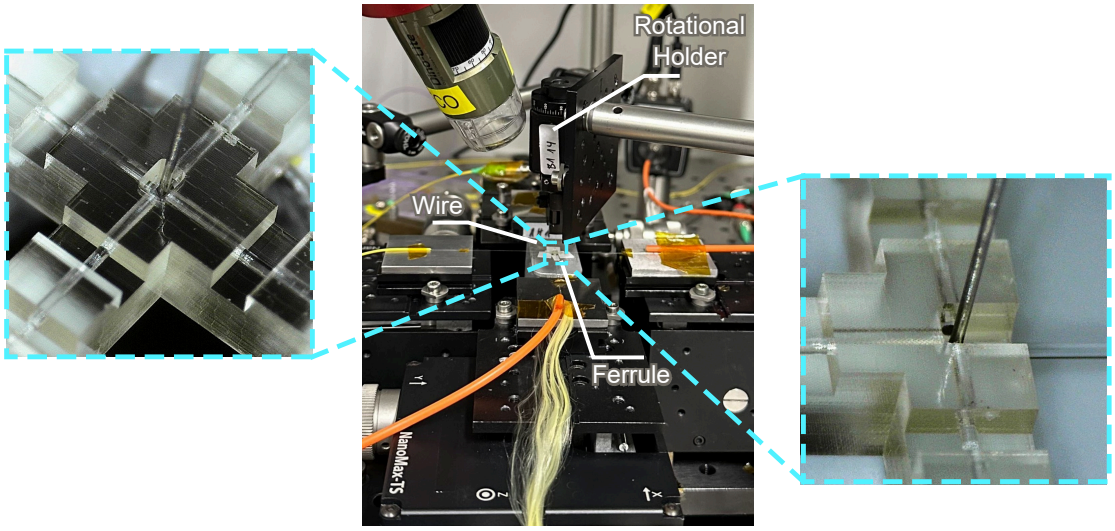


Figure 5.9: Images of the knife-edge setup used to evaluate the four-channel crossed ferrule and the three-channel T-shaped ferrule. In contrast to the groove-plate measurement, the tungsten wire is inserted from above. Its flat edge is oriented before being lowered into the interaction region, since the wire cannot be observed directly at its final position because of the restricted viewing angle. The enlarged region on the left shows the interaction region of the four-channel crossed ferrule. The enlarged region on the right shows the interaction region of the three-channel T-shaped ferrule, where an MM fiber is aligned in free space from the open side to collect the light emitted by the SM fiber inserted into the orthogonal channel.

The extracted displacements between the two beam-center positions are summarized in Table 5.2. The measured values range from approximately 0.49 µm to 0.60 µm, with an average displacement of approximately 0.54 µm over the six measurements. The maximum deviation from this average is only approximately 0.06 µm, which is considerably smaller than the variation of more than 1 µm observed for the groove plate. This supports the interpretation that the comparatively large variation obtained with the groove plate is primarily associated with the additional clamping procedure, whereas the enclosed channels of the printed ferrule provide a substantially more reproducible positioning of the fibers.

Table 5.2: Relative beam-center displacements determined for the four-channel crossed ferrule using the knife-edge method. Six independent measurements were performed, with the fibers recleaved, removed, and reinserted between successive measurements.

	It. 1	**It. 2**	**It. 3**	**It. 4**	**It. 5**	**It. 6**
Displacement / µm	(0.49 ± 0.03)	(0.60 ± 0.04)	(0.54 ± 0.04)	(0.53 ± 0.03)	(0.52 ± 0.08)	(0.54 ± 0.04)

In addition, the measured displacements consistently cluster around approximately 0.54 µm, indicating a systematic contribution to the relative beam-center offset. This is consistent with a small systematic displacement between the two orthogonal channel axes. However, since the measured beam positions can also be influenced by effects such as non-zero cleave angles of the SM fibers, the measured displacement cannot be attributed exclusively to the printed channel geometry. Nevertheless, the consistently observed sub-micrometer displacement indicates that the four-channel ferrule provides a high degree of relative

alignment precision between the two orthogonal fiber axes. The observed displacement is also compatible with the specified sub-micrometer fabrication accuracy of the PPGT+ system for IP-S [48].

Iteration 5 exhibits a noticeably larger fit uncertainty than the other measurements. During this measurement, stronger fluctuations of the laser power were observed, increasing the scatter of the measured transmitted power. The laser operating current was subsequently adjusted, which reduced these fluctuations for the remaining measurements.

As for the groove-plate evaluation, two representative measurements are shown in Figure 5.10. Panel (a) shows the measurement yielding a displacement of $d = (0.49 \pm 0.03)$ µm, while panel (b) shows a measurement yielding $d = (0.54 \pm 0.04)$ µm.

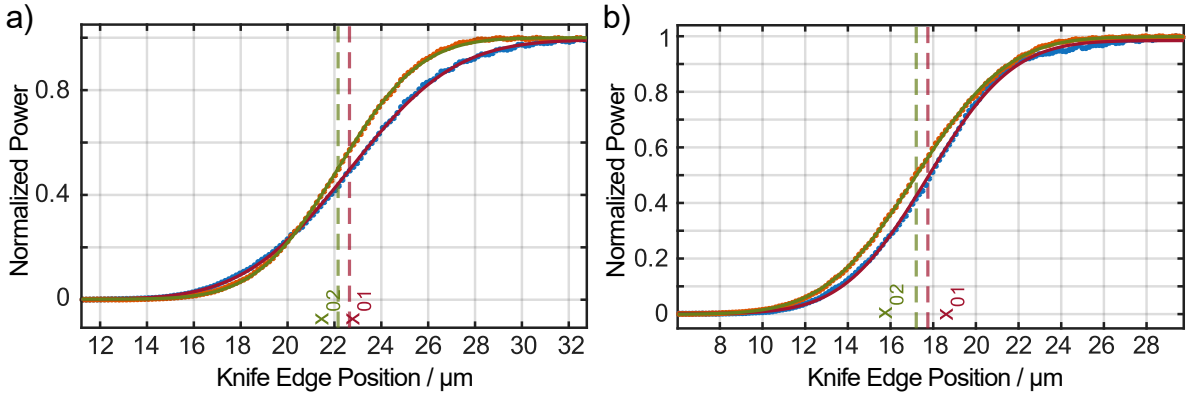


Figure 5.10: Representative knife-edge measurements obtained for the four-channel crossed ferrule. The transmitted power along the two orthogonal optical axes, shown in blue and orange, is fitted according to Equation 5.2. (a) Measurement yielding a relative beam-center displacement of $d = (0.49 \pm 0.03)$ µm. (b) Measurement yielding $d = (0.54 \pm 0.04)$ µm. Both measurements were performed using the same four-channel crossed ferrule, with the fibers recleaved, removed, and reinserted between the measurements.

5.3.2 Assessment of the Three-Channel T-Shaped Ferrule

To compare the three-channel T-shaped ferrule with the other alignment approaches, the same knife-edge method was applied. However, since the T-shaped ferrule provides only three channels, the transmitted light from the SM fiber inserted into the orthogonal channel had to be collected from the open side of the interaction region. For this purpose, an MM fiber tip was aligned in free space until the transmitted power was maximized. This configuration is shown in the enlarged region on the right in Figure 5.9. The remaining measurement procedure followed the same principle as for the four-channel crossed ferrule. The tungsten wire was oriented with its flat edge towards the SM-fiber tips and subsequently inserted into the interaction region.

The free-space alignment of the MM fiber introduced an additional experimental limitation. Because of the restricted available space, the MM fiber could only be clamped at a comparatively large distance from its tip. As a result, small positional drifts of the fiber tip occurred over the long measurement duration and affected the collected optical power. To reduce this effect, the number of acquired data points was substantially reduced, thereby shortening the measurement time. Owing to additional contamination of the fiber end facets during the measurements, only five independent representative measurements were obtained.

As can be seen from the extracted displacement values listed in Table 5.3, the measured values range from approximately 0.58 µm to 1.67 µm, with an average displacement of approximately 1.02 µm over the five measurements. The variation between repeated measurements is larger than for the four-channel crossed ferrule and also exceeds the contribution expected from cleave-angle effects alone.

Table 5.3: Relative beam-center displacements determined for the three-channel T-shaped ferrule using the knife-edge method. Five independent measurements were performed, with the fibers recleaved and repositioned between successive measurements. One MM fiber was aligned in free space from the open side of the ferrule.

	It. 1	**It. 2**	**It. 3**	**It. 4**	**It. 5**
Displacement / µm	(1.45 ± 0.11)	(0.59 ± 0.11)	(1.67 ± 0.09)	(1.00 ± 0.17)	(0.58 ± 0.16)

Two representative measurements are shown in Figure 5.11. Panel (a) shows the measurement yielding a displacement of $d = (1.67 \pm 0.09)$ µm, while panel (b) shows a measurement yielding $d = (0.59 \pm 0.11)$ µm. The measurement conditions for the T-shaped ferrule were less favorable than for

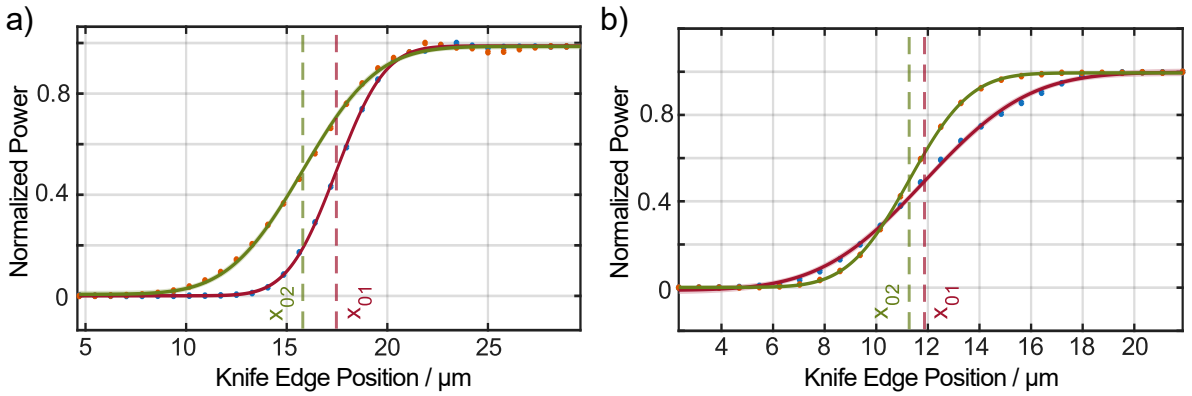


Figure 5.11: Representative knife-edge measurements obtained for the three-channel T-shaped ferrule. The transmitted power along the two orthogonal optical axes, shown in blue and orange, is fitted according to Equation 5.2. (a) Measurement yielding a relative beam-center displacement of $d = (1.67 \pm 0.09)$ µm. (b) Measurement yielding $d = (0.59 \pm 0.11)$ µm. Both measurements were performed using the same T-shaped ferrule, with the fibers recleaved and repositioned between the measurements. Owing to the reduced number of measurement points and the required free-space alignment of one MM fiber, the resulting uncertainties are larger than those obtained for the four-channel crossed ferrule.

the four-channel crossed ferrule. The positional drift of the freely aligned MM fiber, together with the reduced number of acquired data points, increased the uncertainty of the fitted beam-center positions. The resulting displacement values should therefore be interpreted primarily as an indication of the achievable alignment rather than as a precise quantitative measure of the channel offset.

5.3.3 Image-Based Assessment of the Three-Channel T-Shaped Ferrule

The T-shaped ferrule additionally allowed the relative positions of the fiber axes to be assessed directly by microscope imaging. This was possible because the omitted fourth channel provides lateral optical access to the central interaction region. Neither the four-channel crossed ferrule nor the groove plate provides

equivalent visibility, and neither could therefore be evaluated using this method. The image-based assessment therefore provides an independent consistency check of the alignment achieved by the printed ferrule geometry.

For this purpose, an existing beam-profiler setup was used. The setup and its working principle are described in detail in Refs. [74, 75] and are therefore only summarized briefly here.

The beam profiler enables the transverse intensity distribution of a propagating beam to be recorded at different positions along its propagation axis. The setup was originally developed for characterizing the beam emitted from fiber end facets. A three-axis motorized translation system, combined with a tip–tilt stage, enables precise alignment of the investigated structure with respect to the optical axis of the beam profiler as well as automated scanning along this axis. The emitted beam is imaged by a microscope objective onto a monochrome camera [75].

For the alignment assessment of the three-channel T-shaped ferrule, the ferrule was mounted on the translation stage with its open side facing the microscope objective. Two cleaved SM fibers were inserted into the opposing cavity-axis channels, while a third cleaved SM fiber was inserted into the orthogonal pump channel. The latter was spliced to a patch cable connected to a laser operating at 780 nm, making the emitted beam visible to the camera. The two fibers defining the cavity axis were positioned with an end-facet separation of approximately 50 µm.

The relative alignment was assessed by monitoring the propagation of the beam emitted from the SM fiber in the pump channel with respect to the two fibers defining the cavity axis. To make the edges of these fibers visible in the camera image, an external white-light source was focused onto the fiber end facets from above. The camera exposure time was increased while the optical power coupled into the pump fiber was reduced until sufficient contrast was obtained between the propagating beam and the illuminated fiber surfaces.

The beam-profiler software [75] was used to determine the transverse beam-center position from Gaussian fits to the intensity distribution along both lateral directions. Since the measured beam-center trajectory depends on the relative tilt between the emitting fiber and the optical axis of the beam profiler, this tilt was optimized before the alignment measurement. Several tip–tilt settings were tested, and the residual propagation angle of the beam center relative to the beam-profiler axis was estimated from the first and last measured center positions. Through successive adjustment, this relative angle was reduced from approximately $(1.588 \pm 0.004)^\circ$ to $(-0.171 \pm 0.004)^\circ$. A visualization of the beam-center trajectory along the propagation direction for the initial and optimized tilt settings is shown in Figure A.8.

After optimizing the tilt, the beam propagation from the SM-fiber facet was recorded continuously for different propagation distances. By using sufficiently small scan steps, the beam-center position could be tracked across the interaction region. The position of the cavity axis was identified from the image plane in which the upper and lower edges of the two opposing cavity fibers appeared sharpest, corresponding approximately to the plane through their fiber cores. The measured intensity distribution at this position is shown in Figure 5.12.

For the determination of the cavity-axis position, the centers of the two opposing cavity fibers were estimated from the sharp transitions between the fiber surfaces and the background. To improve the accuracy of this estimate, the corresponding grayscale profiles were evaluated along the vertical lines indicated in Figure 5.12. The fiber edges were identified from the transition between the low-intensity background and the increased grayscale intensity associated with the illuminated fiber surfaces. From the identified edge positions, the central position of the cavity axis was determined to be 543.54 ± 5 pixels, where the uncertainty reflects the estimated precision with which the edge positions could be identified.

Using the known image calibration factor of 5.4 µm per 20 pixels [74, 75], this corresponds to a

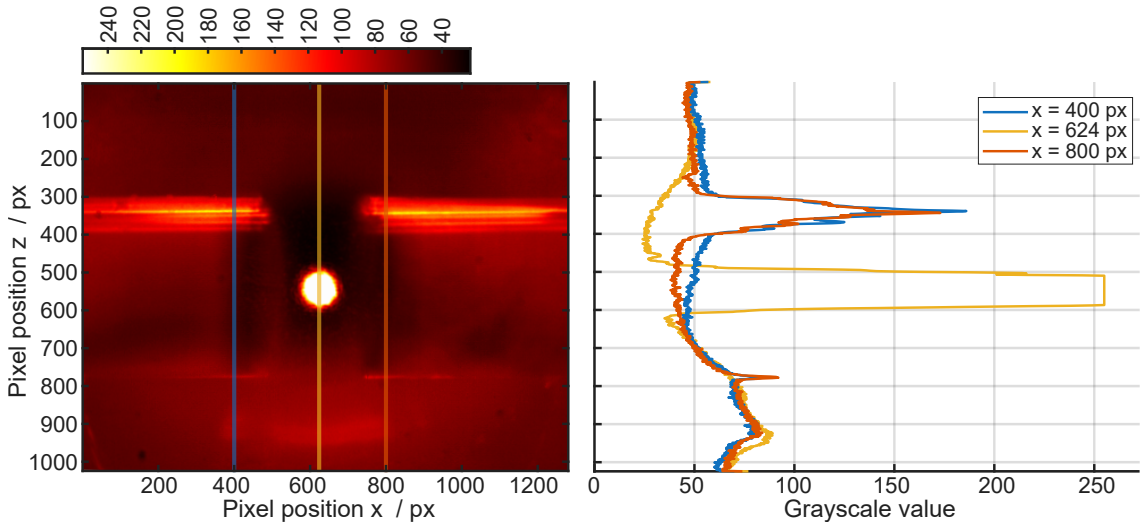


Figure 5.12: Beam-profiler image used for the image-based alignment assessment of the three-channel T-shaped ferrule. The image shows the intensity distribution of the beam emitted from the cleaved SM fiber inserted into the pump channel while the two opposing SM-fiber tips defining the cavity axis are simultaneously illuminated from above. The beam is generated using a laser operating at 780 nm. For selected vertical image columns, the corresponding grayscale values are plotted using the same vertical pixel coordinate as in the camera image, allowing the positions of the fiber edges and the beam center to be compared directly.

cavity-axis position of (146.76 ± 1.35) µm. The beam-center position obtained from the Gaussian fit implemented in the beam-profiler software was (147.24 ± 0.02) µm. The resulting displacement between the beam center and the cavity axis is therefore

$$d_b = (0.49 \pm 1.36)\ \mu\text{m}.$$

Within its comparatively large uncertainty, the image-based displacement is consistent with the average displacement of approximately 1.02 µm obtained from the knife-edge measurements of the T-shaped ferrule. The image-based assessment therefore provides an independent consistency check and supports the micrometer-scale alignment indicated by the knife-edge measurements.

5.4 Comparison of the Alignment Performance of the Assembly Platforms

Before comparing the alignment achieved by the different assembly platforms, the performance of the investigated characterization methods is summarized. The rotating-pillar method provided a first approach for determining the relative displacement of two orthogonal fiber axes, but repeated measurements showed strongly inconsistent results. The method was particularly sensitive to deviations from an ideal rotation of the pillar around the fiber axis, which could not be separated reliably from the actual alignment offset. It was therefore not used for the subsequent quantitative comparison.

The knife-edge method provided a considerably more reproducible alternative for evaluating the relative positions of the freely propagating beams, representing the alignment of the two orthogonal axes predefined by the grooves or channels. By translating the same edge through both orthogonal beams,

the relative beam-center positions could be extracted directly from the fitted error-function dependence. Measurements performed in opposite scan directions yielded consistent center positions, indicating that no pronounced scan-direction-dependent effect was introduced by the translation stage. The knife-edge method was therefore used for the quantitative comparison of the groove plate and printed ferrules.

Overall, both assembly platforms were found to be capable of providing sufficiently precise alignment of orthogonal fiber axes for the intended crossed-fiber configuration. However, the repeated knife-edge measurements revealed a clear difference in reproducibility. For the groove plate, the measured relative beam-center displacements ranged from approximately 0.09 µm to 3.09 µm after repeated repositioning and clamping. In contrast, the four-channel printed crossed ferrule consistently yielded sub-micrometer displacements around 0.54 µm. Even under the less favorable measurement conditions of the three-channel T-shaped ferrule, the extracted displacements remained within a narrower range of approximately 0.58 µm to 1.67 µm.

The image-based assessment of the T-shaped ferrule provided an additional consistency check. The extracted displacement was found to be on the same order of magnitude as the values obtained from the knife-edge measurements. The knife-edge evaluation of this geometry was subject to less favorable experimental conditions, since one MM fiber had to be aligned in free space and could drift during the comparatively long measurement. The resulting displacement values therefore carry larger uncertainties than those obtained for the four-channel ferrule. Since the three-channel T-shaped ferrule and the four-channel crossed ferrule were fabricated using identical printing parameters and very similar post-processing conditions, the agreement between the different measurements nevertheless supports the conclusion that the printed channels provide reproducible alignment of the orthogonal fiber axes. The remaining differences between the two ferrule designs may originate from the different experimental conditions as well as from differences in the design geometry and the resulting shrinkage behavior.

It should be noted that the knife-edge measurement determines the relative positions of the propagating beam centers rather than the geometrical positions of the fiber cores themselves. The extracted displacement can therefore additionally contain contributions from effects such as non-zero cleave angles of the SM fibers. Although the estimated magnitude of this contribution is small compared with the variation observed for the groove plate, the measured displacement should not be interpreted as a direct measurement of the mechanical channel alignment alone.

The comparison therefore indicates that the enclosed channels of the printed ferrules provide a more reproducible positioning of the fibers, whereas the groove-plate result is more strongly influenced by the manual clamping procedure. Although the groove plate was shown to be capable of achieving very small relative displacements, this alignment could not be reproduced reliably after repeated repositioning and clamping.

To assess the influence of geometrical misalignment on the intended photothermal gas spectroscopy application, the crossed-fiber geometry was modeled and the interaction of the two optical fields was quantified by their spatial intensity overlap rather than by a coherent optical mode overlap [76]. The corresponding relative intensity overlap was then calculated for different lateral displacements Δy between the two optical axes. For a given displacement, the overlap was determined from

$$J(\Delta y) = \iiint I_1(x, y, z) I_2(x, y, z, \Delta y)\, \mathrm{d}x\, \mathrm{d}y\, \mathrm{d}z. \tag{5.3}$$

The calculated overlap was normalized to the value obtained for perfectly aligned optical axes,

$$\eta_{\mathrm{rel}}(\Delta y) = \frac{J(\Delta y)}{J(0)}, \tag{5.4}$$

such that perfect lateral alignment corresponds to a relative intensity overlap of 100 %.

For the pump-beam–cavity configuration, I_1 describes the Gaussian cavity-mode intensity, while I_2 represents the freely propagating Gaussian beam emitted from the orthogonal pump fiber, whose end facet is positioned at a distance of 80 µm from the center of the cavity axis. The pump-beam radius is calculated as a function of the propagation distance from the fiber end facet using Equation 2.2. The longitudinal standing-wave modulation of the cavity field is neglected, such that the calculation describes the geometric overlap of the Gaussian intensity envelopes.

A visualization of the calculated intensity distributions for lateral pump-beam offsets of 0 µm, 0.5 µm, and 3.1 µm is shown in Figure 5.13. These values represent perfect alignment, the displacement typically obtained for the printed ferrule, and approximately the largest displacement measured for the groove plate, respectively. The corresponding dependence of the relative intensity overlap on the lateral offset is shown below the field distributions. The calculated overlap remains above 90 % for the full range of

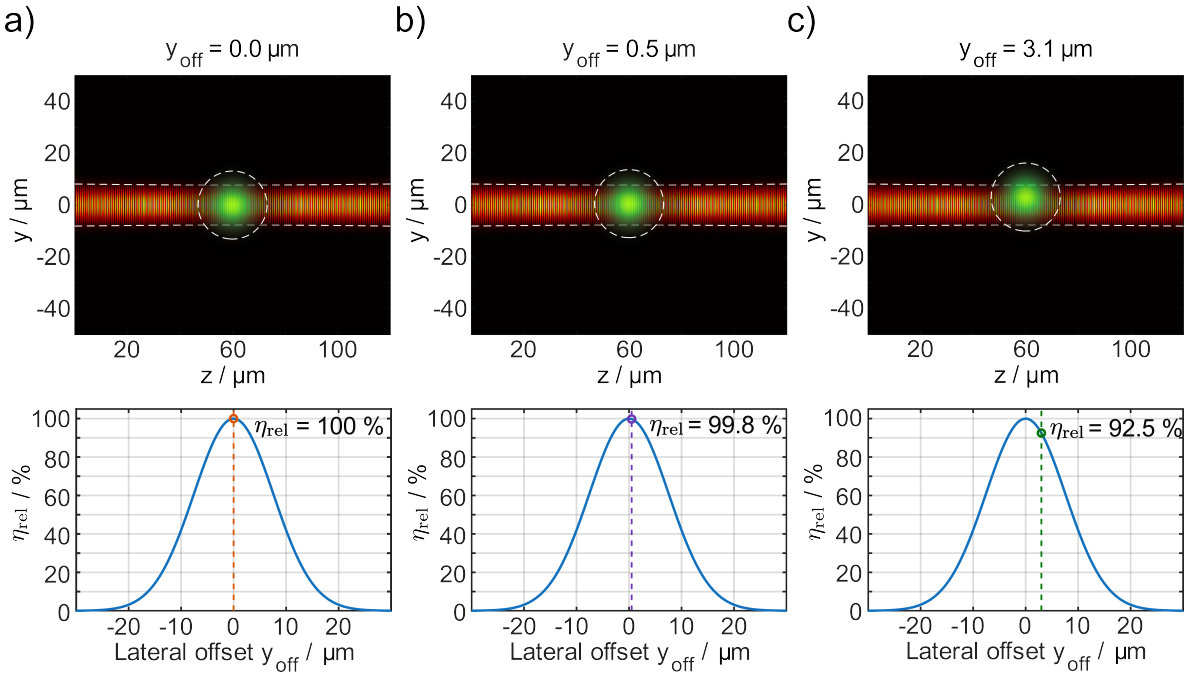


Figure 5.13: Visualization and relative intensity overlap between the pump beam and the cavity field for different lateral offsets. The upper row shows the cavity field together with the propagating pump beam in a cross section along the cavity axis through the mode center for offsets of (a) 0 µm, (b) 0.5 µm, and (c) 3.1 µm. These values represent perfect alignment, a displacement representative of the printed ferrule, and approximately the largest displacement measured for the groove plate, respectively. The cavity field is calculated for a wavelength of 1 550 nm, a cavity length of 120 µm, and mirror radii of curvature of 300 µm. The pump beam propagates over a distance of 80 µm from the pump-fiber end facet to the cavity axis. The corresponding $1/e^2$ intensity boundaries of the cavity field and pump beam are indicated by dotted white lines. The lower panel shows the relative intensity overlap as a function of the lateral pump-beam offset, normalized to 100 % at zero offset. The offsets of 0 µm, 0.5 µm, and 3.1 µm are indicated by vertical lines together with the corresponding overlap values.

experimentally observed displacements. For a displacement of approximately 0.5 µm, representative of the four-channel printed ferrule, the relative intensity overlap reaches 99.8 %. Even for the largest displacement measured with the groove plate, an overlap of 92.5 % is retained, corresponding to only a moderate reduction for the investigated cavity and pump-beam parameters. Both assembly platforms therefore provide sufficient lateral alignment for guiding the pump beam through the cavity interaction region, while the printed ferrules additionally provide considerably more reproducible positioning.

The calculated overlap values should be interpreted as estimates of the sensitivity to lateral displacement rather than as an exact description of the experimental system. The calculation assumes ideal Gaussian beam and cavity-mode distributions and does not include effects such as angular misalignment, deviations from ideal mode shapes, fiber-mirror imperfections, or perturbations of the cavity mode by nearby structures.

Beyond the improved reproducibility, the printed ferrules also offer practical advantages for the realization of a tunable fiber cavity. For the groove plate, further fabrication steps would be required to enable cavity-length tuning, including cutting the ceramic structure between the two cavity-fiber supports. Such processing could introduce an additional relative displacement of the opposing grooves and was not investigated within this work. The printed ferrule, in contrast, already incorporates the mechanical design required for later cavity-length adjustment.

Based on the alignment results and the simpler realization of cavity-length tuning, further development therefore focused on the printed ferrule approach. This choice is also supported by previous demonstrations of fiber cavities aligned and stabilized using ferrule-based assemblies [11, 19, 20, 28]. The groove-plate approach was consequently not pursued further in this work. However, the present results do not exclude its use for a high-finesse, passively stable fiber cavity with an additional pump fiber. Further optimization of the clamping method, together with an evaluation of the additional fabrication steps required for cavity-length tuning, would be necessary to assess its full potential.

CHAPTER 6

Implementation of Crossed Fiber Assemblies

Based on the evaluation of the different assembly platforms, the printed ferrule approach was selected for the realization of the crossed fiber geometries. As a first step, a three-channel T-shaped assembly was prepared in which a fiber Fabry–Pérot cavity is crossed by a pump beam delivered through an additional optical fiber. The implementation of this configuration is described in Section 6.1.

In parallel, the concept was extended towards a more advanced configuration consisting of two orthogonal fiber Fabry–Pérot cavities. In contrast to the three-channel assembly, this configuration requires not only the predefined relative alignment of both optical axes, but also the ability to independently adjust the cavity lengths along both axes. The corresponding concept is introduced in Section 6.2, followed by its mechanical implementation in Section 6.3.

Finally, a method for evaluating the relative alignment of the actual cavity modes was developed. This is necessary because the cavity-mode positions can deviate from the alignment predefined by the ferrule due to the individual properties of the fiber mirrors. The method and first experimental tests are described in Section 6.4.

6.1 Three-Channel Pump–Cavity Assembly

After the printed ferrule approach had been selected for the final implementation, preparations were made for the realization of a crossed fiber assembly using the three-channel T-shaped ferrule. For the pump axis, a single-mode fluoride-glass optical fiber (InF3 Fiber) from Thorlabs [77] was selected according to the requirements of the collaborating group. The fiber is specified for single-mode operation over a wavelength range of 3.2 to 5.5 µm, has a diameter of 125 µm, and a mode-field diameter of approximately 11 µm, which is slightly larger than that of the standard SM fibers used throughout this work.

The ferrule was designed and assembled as described in Subsection 4.2.1. The channels for the coated cavity fibers were designed with a diameter of 154 µm, while the channel for the uncoated 125 µm fluoride pump fiber was designed with a diameter of 144 µm. The exact design is visualized and described in Figure A.7.

After assembly of the mechanical components, the structure was mounted on an additional ceramic base plate to simplify its later integration into the gas-spectroscopy setup of the collaborating group. The electrical wires, which had already been attached to the piezo actuator, were fixed to the ceramic plate. In addition, a small section of the piezo actuator was glued to the plate to improve the mechanical

stability of the assembly. The final assembly, still without the fibers, is shown in Figure 6.1.

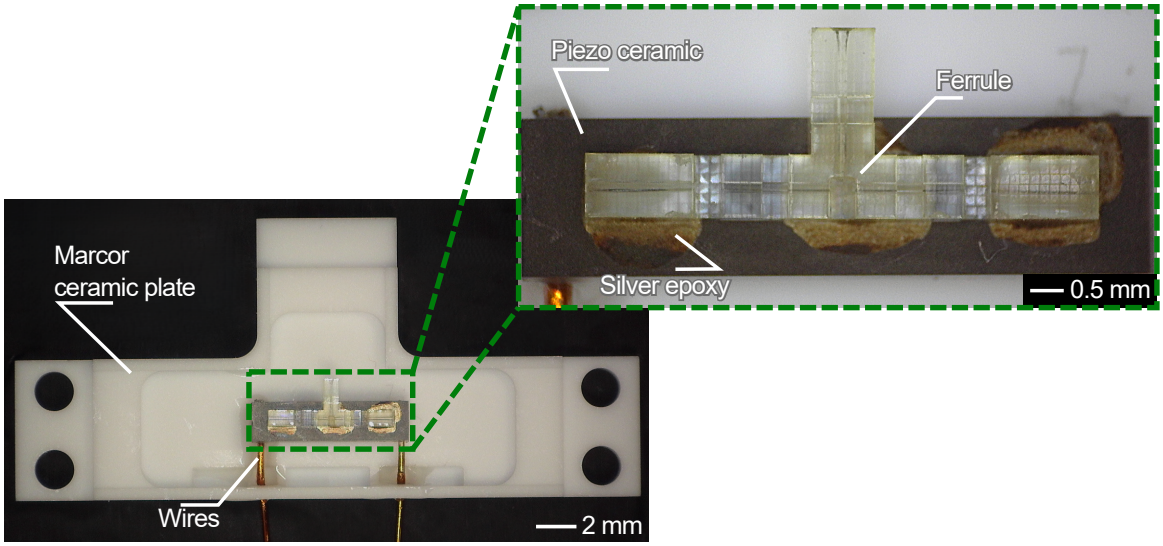


Figure 6.1: Microscope image of the final T-shaped fiber Fabry–Pérot cavity assembly before fiber insertion. An enlarged view of the T-shaped ferrule is shown. The ferrule is fixed to a piezoceramic actuator using silver epoxy. Electrical wires are attached on the opposite side of the piezoceramic actuator, also using silver epoxy. The ferrule–piezo assembly is additionally fixed with UV-curable epoxy to a supporting T-shaped ceramic plate. Only one edge of the ferrule–piezo assembly is fixed to the supporting plate, allowing the piezoelectric actuator to expand and contract freely. Each arm of the support has a width of 9 mm, while the plate thickness is 2 mm. Raised sections at the ends of the arms provide fixation points for the fibers.

Final fiber insertion was postponed until suitable protective storage containers were available, in order to avoid contamination of the exposed fiber end facets after assembly. Since these containers were not available within the remaining project time, the final insertion and alignment of the fibers could not be completed.

In parallel to the preparation of the T-shaped pump–cavity assembly, the four-channel crossed ferrule was considered as a basis for a second configuration in which both orthogonal axes form independent fiber Fabry–Pérot cavities. This geometry extends the concept from a single cavity intersected by a pump beam to two crossed cavity modes and therefore imposes additional requirements on the relative cavity alignment and stabilization.

6.2 Crossed-Cavity Concept

As a more advanced assembly concept, a configuration consisting of two crossed high-finesse cavities was investigated. While such a configuration offers potential for a variety of applications, the focus here is placed on photothermal gas sensing, as this represents the primary objective of the proposed implementation. In this configuration, one cavity serves as the optical readout cavity, while the second cavity enhances the pump field within the sensing volume. This approach is particularly beneficial for weakly absorbing gas species or low target-gas concentrations.

In photothermal gas spectroscopy, the measured signal originates from a modulation of the refractive index caused by local heating of the gas through absorption of the pump beam. The magnitude of this

refractive-index modulation depends on the absorbed optical power and therefore on both the absorption coefficient of the targeted gas species and the incident pump power [22]. For weakly absorbing gases, only a small fraction of the incident pump power is absorbed during a single pass through the sensing region. Consequently, comparatively high pump powers may be required to generate a sufficiently strong refractive-index modulation [22].

Integrating the pump beam into an optical cavity can increase the optical intensity within the sensing region. On resonance, the light undergoes multiple round trips through the gas, resulting in an enhanced intracavity field and increased interaction with the absorbing species. For an ideal Fabry–Pérot cavity under comparable coupling conditions, the resonant intracavity power buildup scales approximately with the cavity finesse [12]. The resulting increase in absorbed optical power can consequently enhance the photothermal signal.

Since the photothermal signal arises from a modulation of the refractive index, the pump power is generally modulated in time [22]. When a resonant pump cavity is used, the modulation frequency should remain small compared with the cavity linewidth such that the intracavity field can follow the modulation quasi-statically [78]. The cavity linewidth is given by Equation 2.7, together with the free spectral range given by Equation 2.4.For a cavity length of 120 µm and a finesse of 1.5×10^5, this yields a linewidth of approximately 8.3 MHz. The modulation frequencies relevant for photothermal sensing are typically well below the characteristic response bandwidth of the cavity and therefore do not constitute a limiting factor in this configuration.

The actual modulation frequency is instead mainly determined by the thermal response of the gas and by the noise characteristics of the measurement. At high modulation frequencies, the thermal response can become reduced, while at very low frequencies the measurement becomes increasingly susceptible to technical and low-frequency noise [79, 80]. As a compromise between these effects, modulation frequencies in the kilohertz range are commonly employed in related photothermal and photoacoustic sensing schemes [80].

An additional limitation arises from the spectral properties of the available fiber mirrors. The mirrors used throughout this work are optimized for operation near 1 550 nm, corresponding to the probe wavelength. According to the manufacturer specifications shown in Figure A.1, the mirror reflectivity decreases outside the designed spectral range, consequently reducing the achievable cavity finesse. The pump wavelength, however, has to be chosen according to an absorption transition of the targeted gas species and will generally differ from the probe wavelength.

For methane, for example, a relevant absorption transition lies at approximately 1 651 nm [28]. Estimated from the plotted reflection spectrum in Figure A.1, the mirror reflectivity at this wavelength is approximately 99.9985 %. Assuming two identical mirrors and neglecting additional intracavity losses, this corresponds to a theoretically achievable finesse of approximately 2.1×10^5, compared with approximately 3.1×10^5 at the probe wavelength.

Nevertheless, even for pump wavelengths further outside the optimized coating range, a cavity with a lower finesse can still provide a significant intracavity intensity enhancement, provided that sufficient mirror reflectivity and suitable coupling conditions are retained.

To further assess the relevance of the measured alignment precision for a crossed-cavity configuration, the relative intensity overlap of two orthogonal Fabry–Pérot cavity modes was calculated according to Equation 5.3 and Equation 5.4. Both intensity distributions are described by Gaussian cavity modes propagating along the two orthogonal cavity axes. The resulting displacement dependence was compared with the previously considered pump-beam–cavity configuration.

A visualization of the transverse overlap at the center of the probe-cavity axis is shown in Figure 6.2

for selected lateral offsets of the pump cavity. Panels (a) and (b) depict the overlap for displacements of 0.5 µm and 3.1 µm, respectively, while panel (c) shows the corresponding dependence of the relative intensity overlap on lateral displacement together with the pump-beam–cavity case.

The comparison shows that the crossed-cavity configuration is more sensitive to lateral displacement than the pump-beam–cavity configuration. For a displacement of 0.5 µm, corresponding approximately to the offset extracted for the printed ferrule, the relative intensity overlap remains very high in both cases, reaching 99.8 % for the pump-beam–cavity case and 99.6 % for the crossed-cavity case. The effect of such a small displacement on the geometric intensity overlap is therefore negligible for the investigated parameters.

For a displacement of 3.1 µm, corresponding approximately to the largest displacement measured for the groove plate, the relative overlap decreases more noticeably. In this case, the overlap remains at 92.5 % for the pump-beam–cavity configuration, but drops to 85.9 % for the crossed-cavity case. This indicates that the crossed-cavity concept imposes somewhat stricter requirements on the alignment precision.

Nevertheless, for the sub-micrometer displacement values achieved with the printed ferrule, the calculated overlap remains essentially maximal. The printed-ferrule platform therefore appears sufficiently precise not only for guiding a pump beam into the cavity region, but also for the realization of two crossed cavity fields.

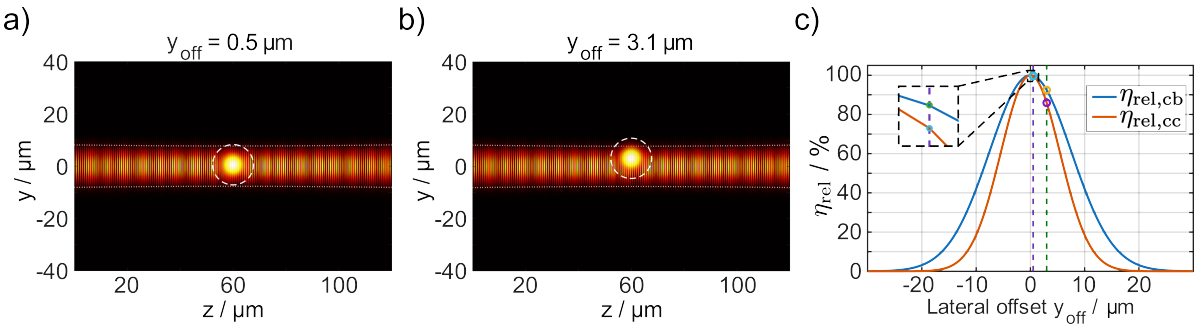


Figure 6.2: Visualization and calculated relative intensity overlap for a pump beam crossing a cavity mode and for two crossed cavity modes with different lateral displacements. Panels (a) and (b) show the crossed-cavity case for lateral offsets of 0.5 µm and 3.1 µm, respectively. These offsets correspond approximately to the displacement extracted for the printed ferrule and to the largest displacement measured for the groove plate. The cavity fields were calculated for a wavelength of 1 550 nm, a cavity length of 120 µm, and mirror radii of curvature of 300 µm. For comparison, the pump beam was assumed to propagate over a distance of 80 µm from the pump-fiber end facet to the cavity axis. The corresponding $1/e^2$ intensity boundaries are indicated by dotted white lines. Panel (c) shows the calculated relative intensity overlap as a function of lateral displacement, normalized to 100 % at zero offset. The pump-beam–cavity case, $\eta_{\mathrm{rel,cb}}$, is shown in blue and the crossed-cavity case, $\eta_{\mathrm{rel,cc}}$, in orange. The offsets of 0.5 µm and 3.1 µm are marked by vertical lines. At 0.5 µm, the relative overlaps are 99.8 % and 99.6 % for the pump-beam–cavity and crossed-cavity cases, respectively. At 3.1 µm, the corresponding values are 92.5 % and 85.9 %.

With these considerations in mind, further work focused on the realization of a crossed fiber Fabry–Pérot configuration in which both orthogonal axes form optical cavities.

6.3 Crossed-Cavity Implementation

For the implementation of a crossed fiber Fabry–Pérot configuration, the final assembly had to differ from the previously discussed ferrule designs in Subsection 4.2.1, since both orthogonal cavity axes now had to allow independent adjustment of the distance between the opposing fiber mirrors. The resulting assembly concept is illustrated in Figure 6.3.

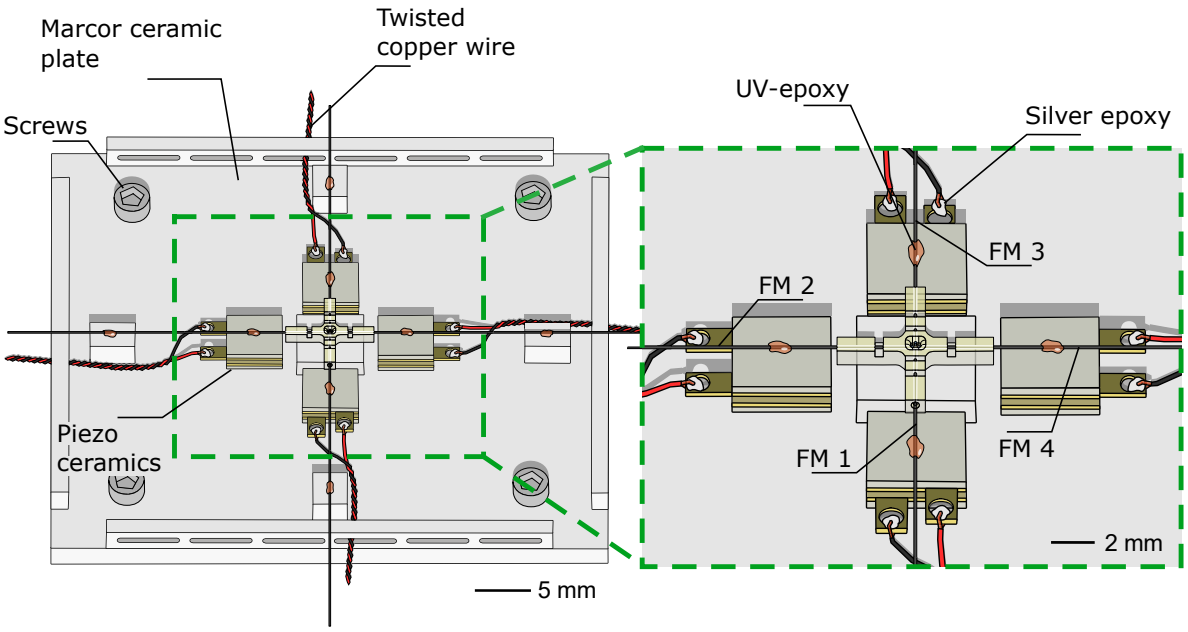


Figure 6.3: Illustration of the final crossed fiber Fabry–Pérot cavity assembly. A ceramic base plate with an area of 44 mm × 44 mm and a thickness of 2 mm supports the complete structure. A central pedestal with a height of 1.5 mm and an area of 6 mm × 6 mm carries the printed crossed ferrule. A through-hole with a diameter of 1 mm provides access from below. Four additional supports are positioned around the central pedestal, while raised structures along the outer edges provide fixation points for the electrical wires. The printed crossed ferrule is glued onto the central pedestal using UV-curable epoxy. Four shear piezoelectric chips are attached around the pedestal using silver epoxy, with their shear directions oriented towards or away from the central interaction region. Twisted electrical wires are connected to the piezoelectric contacts using silver epoxy. Four fiber mirrors, FM1–FM4, are inserted into the ferrule channels and form two orthogonal fiber cavities crossing in the central interaction region. The fibers are fixed to the piezoelectric chips and the outer supports using UV-curable epoxy.

Several modifications were made to the four-channel crossed ferrule design to accommodate this configuration. The additional cuts previously included at the bottom of the cavity arms to ease separation of the printed structure were removed, while the upper openings required for improved removal of unpolymerized resin during development were retained. The length of all four arms was set to 3 mm from the central crossing point in order to preserve symmetry between the two cavity axes.

Openings above and below the central interaction region improve optical access. The upper edges of the central opening were designed with a curved shape to allow observation of the cavity region over a larger angular range. The opening at the bottom was kept smaller in order to reduce the risk of deformation and nonuniform shrinkage during fabrication and post-processing. For the same reason, curved transitions were introduced at the outer connection points between the ferrule arms to provide additional mechanical support. All corresponding curvatures were designed identically in order to

preserve the symmetry of the ferrule.

The final four-channel ferrule design is shown in Figure A.6. Each channel has a nominal diameter of 152 µm. This value is slightly smaller than the previously identified diameter of 154 µm used for coated fibers, since the fibers selected for the crossed-cavity implementation had a thinner coating and were therefore still able to move laterally within a channel with a diameter of 154 µm. Reducing the channel diameter to 152 µm limited the lateral freedom of the fibers while still providing sufficient clearance for axial movement without damaging the fiber coating.

A ceramic base plate was designed to support the ferrule and the individual cavity actuators. A central pedestal provides sufficient space for positioning the ferrule, while a through-hole in the center enables additional access from below. Four shear piezoelectric chips from Thorlabs were arranged around the pedestal and fixed using silver epoxy, with their shear directions aligned along the corresponding cavity axes. This arrangement allows the position of each fiber mirror to be adjusted independently. According to the manufacturer, the shear piezoelectric chips provide a nominal displacement range of 1.3 µm with a tolerance of ±20 % [81]. At a wavelength of approximately 1 550 nm, one longitudinal resonance period corresponds to a cavity-length change of $\lambda/2 \approx 775$ nm. The available piezoelectric displacement should therefore be sufficient to scan over at least one free spectral range.

Low-resistance twisted-pair silver-plated copper wires with Teflon insulation were connected to the piezoelectric contacts using silver epoxy. The printed ferrule was subsequently glued onto the center of the pedestal using UV-curable epoxy, with each ferrule arm aligned towards one piezoelectric chip. The pedestal height of 1.5 mm was chosen such that the ferrule-channel openings are positioned slightly above the top surfaces of the 1.8 mm-high piezoelectric chips. This allows the fibers inserted into the ferrule to be fixed directly onto the piezo surfaces using UV-curable epoxy.

Additional supports with a height of 2 mm were positioned behind the piezoelectric chips, allowing the fibers to be fixed at a second position for increased mechanical stability. The electrical wires were likewise secured to the ceramic base plate using UV-curable epoxy. Microscope images of the fabricated assembly are shown in Figure 6.4(a) and (b).

6.4 Cavity-Mode Alignment Characterization

In contrast to the knife-edge characterization of a freely propagating Gaussian beam, the insertion of an obstruction into a high-finesse cavity modifies the cavity properties themselves. The resulting position-dependent clipping and diffraction losses affect the cavity transmission and finesse, while the circulating field can redistribute around the obstruction over successive round trips. Consequently, the measured transmission no longer corresponds directly to the integrated Gaussian intensity distribution, and the 50 % transmission point does not necessarily coincide with the cavity-mode center [82].

For this reason, the conventional error-function-based knife-edge evaluation used for the freely propagating beams was not considered sufficiently reliable for determining the relative positions of the two high-finesse cavity modes. Instead, an alternative alignment method based on a translating pinhole was investigated, inspired by the approach described in Ref. [82].

6.4.1 Pinhole Method

The pinhole method is based on translating a circular aperture simultaneously through the centers of both cavity modes. The basic measurement principle is therefore similar to the knife-edge method, where an

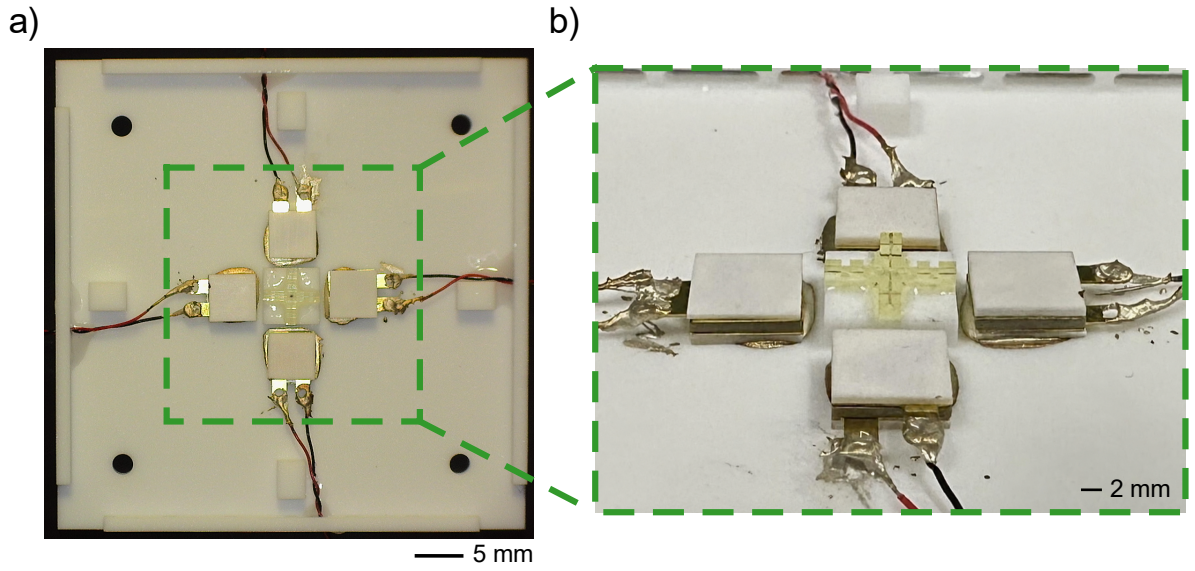


Figure 6.4: Microscope images of the fabricated crossed-cavity assembly prior to insertion of the fiber mirrors. (a) Overview of the complete assembly. (b) Angled close-up view of the central region containing the printed crossed ferrule and the surrounding piezoelectric actuators.

opaque edge is translated through two orthogonally propagating beams. Here, a blocking device with a circular aperture is translated through the crossing region of the cavity fields at an angle of approximately 45° relative to both cavity axes. The position-dependent clipping introduced by the edges of the aperture changes the cavity losses and consequently the depth of the reflected cavity resonance. These effects are considered here primarily as position-dependent clipping losses introduced by the pinhole, without explicitly accounting for diffraction effects.

For a sufficiently symmetric aperture, the induced clipping losses are expected to lead to a maximum resonance depth when the pinhole is centered on the cavity mode. A schematic illustration of this principle is shown in Figure 6.5, where the interaction region and the corresponding reflected resonance signal are displayed for different lateral positions of the pinhole. For simplicity, only a single cavity axis is shown. In the final crossed-cavity implementation, the same principle is applied simultaneously to two orthogonal cavity modes.

To estimate the expected resonance-depth dependence during the pinhole translation, calculations were performed for different cavity finesse values and pinhole diameters for a translation through a single cavity axis. For the cavity field, both mirror radii of curvature were set to 300 µm, the cavity length to 120 µm, and the wavelength to 1 550 nm, assuming perfect alignment. The pinhole was translated through the cavity mode at the beam-waist position.

For a symmetric and otherwise lossless high-reflectivity cavity, the mirror power reflectivity $\mathcal{R}$ corresponding to a selected finesse $\mathcal{F}$ can be estimated from [12]

$$\mathcal{R}_{1,2} = \left(\frac{\sqrt{\pi^2 + 4\mathcal{F}^2} - \pi}{2\mathcal{F}} \right)^2 ,$$

with the corresponding mirror power transmission

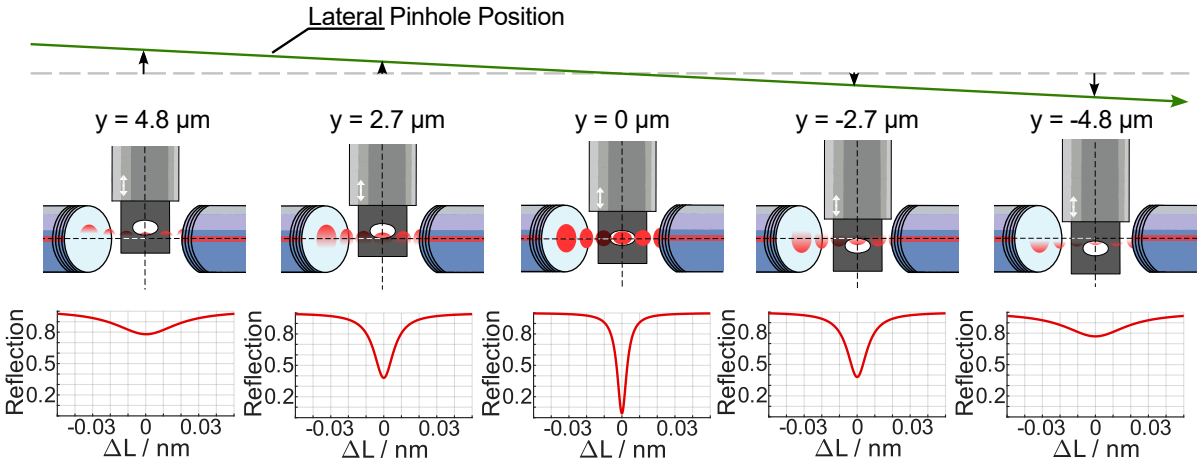


Figure 6.5: Illustration of the pinhole method for different lateral positions of the pinhole relative to a cavity axis. For each position, the interaction region and the corresponding reflected cavity resonance are shown. The cavity is modeled for a wavelength of 1 550 nm, mirror radii of curvature of 300 µm, a cavity length of 120 µm, and a finesse of 1.5×10^5. The pinhole has a diameter of 38 µm and is translated laterally through the cavity mode. As the pinhole moves away from the cavity-mode center, increasing clipping introduces additional round-trip loss and reduces the resonance depth. The corresponding pinhole positions relative to the cavity axis are indicated.

$$T_{1,2} = 1 - \mathcal{R}_{1,2}.$$

The transverse cavity-mode intensity was evaluated on a two-dimensional grid and normalized to unity. The pinhole position is defined as zero when the aperture is centered on the cavity mode, such that the scan position directly represents the lateral displacement relative to the mode center. For each pinhole position, the transmitted fraction of the cavity-mode power was determined by integrating the intensity within the circular aperture. This defines the single-pass pinhole transmission T_{pin}.

Since the intracavity field passes the pinhole twice during one round trip, the corresponding round-trip power transmission is approximated by T_{pin}^2. The corresponding round-trip clipping loss introduced by the pinhole is estimated as [83]

$$\mathcal{L}_{\mathrm{rt,pin}} = 1 - T_{\mathrm{pin}}^2$$

The resulting clipping loss was first included in the approximate expression for the impedance-matching efficiency introduced in Equation 2.9. Since this expression is derived under the assumption of high reflectivity and small additional losses, it becomes increasingly inaccurate when the pinhole introduces strong clipping. For comparison, the reflected cavity field was additionally calculated directly according to Equation 2.5. For each pinhole position, the cavity length was scanned over a small detuning range and the minimum reflected power was determined. The resulting resonance depth was then compared with the impedance-matching approximation.

The calculated resonance depth as a function of pinhole position is shown in Figure 6.6(a) for a fixed pinhole radius of 15 µm and several cavity finesse values. For low-finesse cavities and large pinhole offsets from the cavity axis, resulting in large pinhole-induced losses, noticeable deviations occur between the approximate impedance-matching expression and the directly calculated reflected resonance. In contrast, for high-finesse cavities and around the central pinhole positions relevant for the alignment

measurement, the additional clipping losses remain comparatively small, and both descriptions show good agreement. This is further illustrated in Figure 6.6(b), where the results for a finesse of 1.5×10^5 are compared for several pinhole radii.

The simulations additionally show that the suitable pinhole size depends on the cavity finesse. Since the intrinsic round-trip losses of a high-finesse cavity are very small, additional clipping losses introduced by the pinhole can contribute significantly to the total cavity loss and therefore strongly modify the resonance response. At higher finesse, a larger pinhole is consequently required to retain a clearly detectable resonance over a sufficiently broad range of pinhole positions.

To determine the cavity-mode center, the measured resonance depth should exhibit a clearly identifiable maximum from which the central position can be extracted. Based on the calculation results for a finesse of approximately 1.5×10^5, a pinhole radius of approximately 19 µm was selected as a suitable compromise between spatial sensitivity and measurable resonance contrast, as shown in Figure 6.6(b).

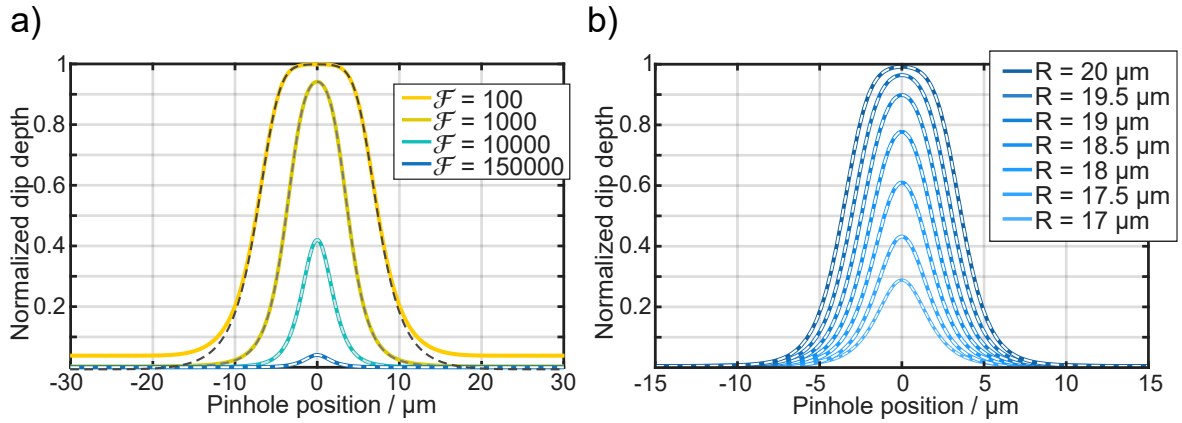


Figure 6.6: Simulated resonance depth as a function of the lateral pinhole position. Solid lines correspond to the results obtained from the impedance-matching approximation, while dotted lines show the resonance depth obtained directly from the calculated reflected cavity field. (a) Resonance depth for a fixed pinhole radius of 15 µm and different cavity finesse values $\mathcal{F}$. At lower finesse and large pinhole offsets, the impedance-matching approximation increasingly deviates from the directly calculated reflected signal. (b) Resonance depth for a fixed finesse of 1.5×10^5 and different pinhole radii. Here, the solid and dotted lines show good agreement. A radius of approximately 19 µm provides a clear central maximum while still maintaining sufficient resonance contrast over the relevant scan range.

Pinhole Fabrication

Since the required pinhole diameter lies in the range of a few tens of micrometers, while the overall structure has to remain sufficiently small to fit into the interaction region, the pinhole was again printed directly onto a cleaved fiber end facet. The fiber carrying the pinhole can then be inserted out of plane into the interaction region, similar to the tungsten wire used for the knife-edge method.

In contrast to the previously investigated pillar, no additional coating was applied to the printed pinhole. For the pinhole method, the absolute resonance depth is not required for determining the cavity-mode center. Instead, only the relative change of the resonance depth as a function of pinhole position is relevant, and the time-consuming coating step was therefore skipped.

The polymer itself was expected to introduce sufficient optical loss when overlapping with the cavity

mode. During several tests throughout this work, polymer residues were found to be easier to remove from the fiber-mirror end facets after accidental contact than metallic coating residues.

The first pinhole was designed with a lateral diameter $d_l = 38\,\mu\text{m}$, based on the initial simulation results. Since the pinhole is inserted into the cavity region at an angle of approximately 45°, the axial diameter was increased to compensate for the projected aperture size and was set to

$$d_a = \frac{d_l}{\cos(45°)}.$$

Microscope images of a printed pinhole and of the pinhole inserted into the cavity region are shown in Figure 6.7(a) and (b), with the pinhole oriented towards the fiber mirrors and towards the microscope, respectively. However, when the first pinhole with a lateral diameter of 38 µm was scanned through a high-finesse cavity, no cavity resonance could be detected near the position of the aperture.

As a methodological check, the same pinhole was therefore tested using a low-finesse fiber pair, which is visible in Figure 6.7(a) and (b). In this case, a clear transition from a blocked signal to a partially transmitted resonance and back to a blocked signal was observed. This indicated that the measurement principle itself worked, but that the aperture diameter of 38 µm was too small for the high-finesse cavity.

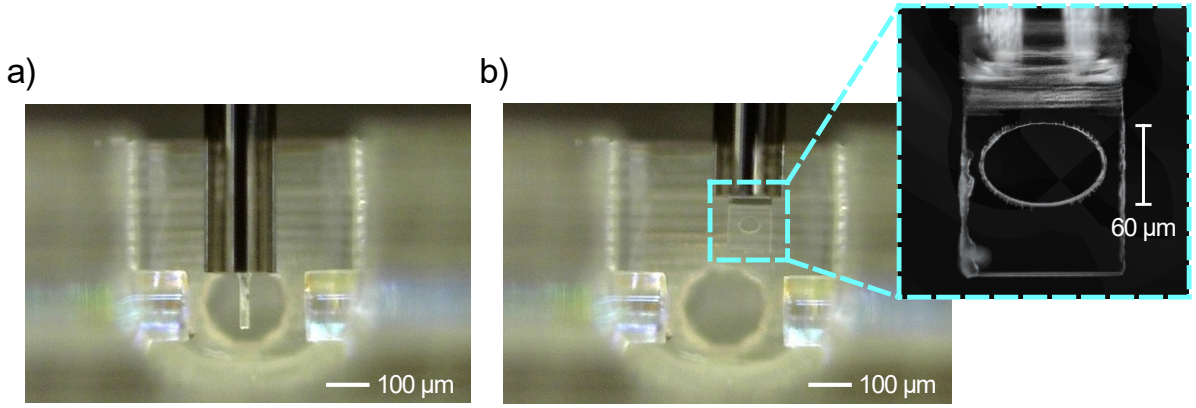


Figure 6.7: Microscope images of a printed pinhole used for the cavity-alignment measurement. The pinhole is printed directly onto a cleaved fiber end facet and inserted into the interaction region between two fiber mirrors. The images show the pinhole oriented towards the fiber mirrors in (a) and towards the microscope in (b). The fiber mirrors are aligned in a printed three-channel T-shaped ferrule and form a low-finesse cavity at a wavelength of 780 nm. The inserted pinhole shown in the setup has a lateral diameter of 38 µm. The enlarged microscope image in (b) shows a separately printed pinhole with a lateral diameter of 60 µm.

To identify a suitable aperture size for the high-finesse cavity, additional pinholes with lateral diameters of 50 µm, 55 µm, and 60 µm were printed and tested using a cavity with a measured finesse of approximately 7×10^4.

The measured resonance depths for different pinhole positions are compared in Figure 6.8. The measurements were performed separately. For each measurement, the relative insertion depth of the pinhole was adjusted in order to make the behavior of the different aperture sizes comparable. The measured resonance depths were additionally normalized to the resonance depth obtained without the pinhole inserted. As shown in Figure 6.8(a), all three measurements exhibit a clear maximum, which can be used to determine the central cavity position. For a rough comparison with the theoretical model, the measured data are overlaid with the calculated resonance-depth curves for a finesse of 7×10^4 in

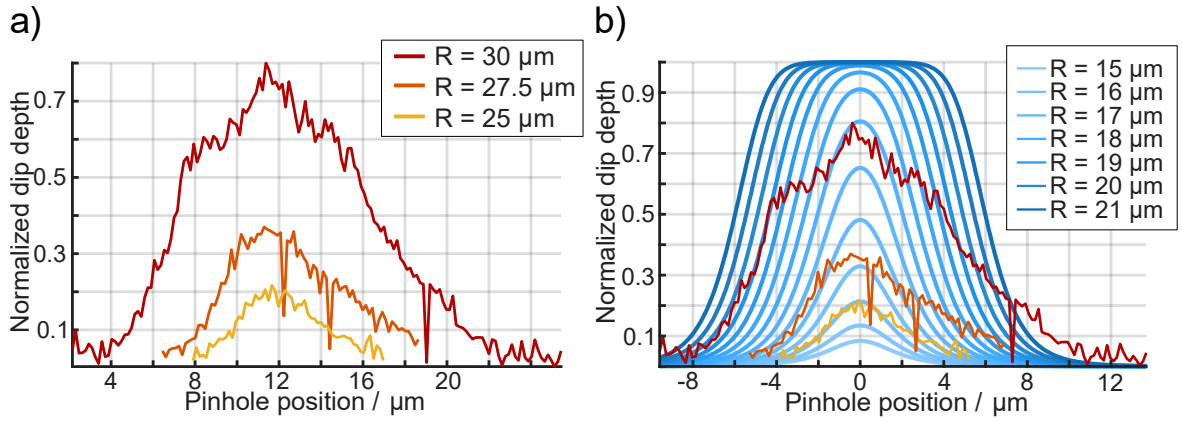


Figure 6.8: Normalized resonance depth as a function of the lateral pinhole position for different pinhole diameters. The resonance depth is normalized to the value measured without the pinhole inserted. Since the measurements were performed separately, the relative insertion depth of the pinhole was adjusted for each measurement to allow comparison of the different aperture sizes. (a) Measured resonance depths for nominal pinhole diameters of 50 µm, 55 µm, and 60 µm. (b) Same measurements overlaid with calculated resonance-depth curves for different modeled pinhole diameters at a finesse of 7×10^4. Only every second modeled pinhole size has an entry in the legend.

Figure 6.8(b). While the absolute values and the exact shape of the measured curves do not agree with the simulation, the increase in slope for larger pinhole diameters follows the predicted trend qualitatively. Since the actual lateral dimensions of the printed pinholes differed from their nominal values by almost 10 µm and the measured curve shapes also deviated from the model, a more detailed comparison using fitted theoretical curves was not considered meaningful.

As expected from the simulations, the measured resonance-depth contrast increases with increasing pinhole diameter. In principle, all tested pinhole sizes provide sufficient variation to identify the maximum and therefore estimate the cavity-mode center. Experimentally, however, the smallest tested pinhole produced a maximum resonance depth of only approximately 5 %. Since resonance depths below approximately 2 % were difficult to identify reliably in the presence of noise on the reflected signal, the larger aperture sizes provided a more robust measurement.

Among the tested pinholes, the 60 µm aperture provided the clearest cavity resonance over the relevant scan range and therefore allowed the cavity-mode center to be identified most reliably. It was consequently selected for the subsequent alignment measurements.

Measurement Procedure and Validation

The general setup of the pinhole method is similar to the one employed for the knife-edge measurements. The fiber carrying the printed pinhole is mounted in a rotational holder, allowing the orientation of the pinhole to be adjusted. The holder is attached to the same motorized translation stage used for the knife-edge method, enabling precise lateral translation through the interaction region.

In contrast to the knife-edge method, the pinhole measurement is applied directly to a cavity mode instead of to a freely propagating beam. Fiber mirrors suitable for forming high-finesse cavities are therefore inserted into the corresponding ferrule channels. In order to scan across the cavity resonance, one fiber mirror of each cavity axis is mounted on a piezoelectric translation stage, allowing the corresponding cavity length to be varied.

The complete measurement setup is shown in Figure 6.9. It is based on the setup used for testing fiber-mirror pairings shown in Figure 3.7, but is extended to two orthogonal cavity axes. Light from the same laser source is divided by a 50/50 fiber-optical coupler and coupled into one fiber mirror of each cavity. The opposing fiber mirrors are each mounted in a rotational holder for signal optimization and subsequently positioned on piezo-driven translation stages. The piezo stages are driven by a waveform-generator signal amplified by a factor of 75, allowing the two cavity resonances to be scanned.

The fiber carrying the pinhole is inserted into the interaction region perpendicular to the plane spanned by the two cavity axes. The motorized translation-stage step size is again set to the minimum available value of 0.156 µm in order to provide the highest possible spatial resolution.

For each pinhole position, the reflected cavity resonance is recorded and fitted according to Equation 3.1. From the fit, the resonance depth and the FWHM are extracted. The resonance depth is then evaluated as a function of the pinhole position. As for the knife-edge measurement, the absolute pinhole position depends only on the chosen starting position of the scan and is therefore not directly comparable between separate measurements.

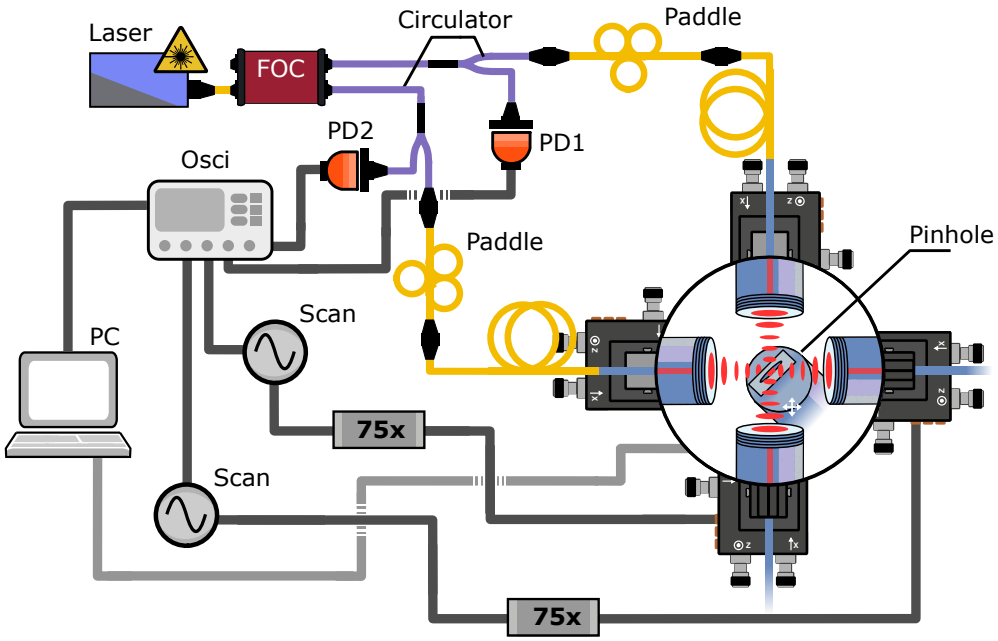


Figure 6.9: Setup used for alignment evaluation with the translated pinhole. Light from a laser operating at 1 550 nm is divided by a 50/50 fiber-optical coupler (FOC) and coupled into one fiber mirror of each cavity axis after passing through a fiber circulator and polarization paddle. The opposing fiber mirror of each axis is mounted on a piezoelectric translation stage driven by a waveform-generator signal (Scan), amplified by a factor of 75. The reflected signal is separated by the circulator, detected by a photodiode, and recorded with an oscilloscope for each cavity axis. The fiber carrying the printed pinhole, shown in the enlarged region, is inserted from below into the interaction region and mounted in a rotational holder on a motorized translation stage, allowing both its orientation and lateral position to be adjusted. Both the motorized translation stage and the oscilloscope are connected to the PC for measurement control and data acquisition. All optical components are fiber-coupled.

Before applying the method to the crossed-cavity alignment, the reproducibility of the measurement procedure was investigated using the previously selected 60 µm pinhole on a single-axis cavity. For this purpose, the measurement was repeated for opposite scan directions and for pinhole orientations

differing by 180°, as shown in Figure 6.10(a) and (b), respectively. The measured resonance depths, also referred to as dip depths, were normalized to the resonance depth measured without the pinhole inserted into the cavity mode.

To investigate a possible dependence on the scan direction, the pinhole was first translated downwards through the cavity mode and subsequently upwards through the same region. These measurements are referred to as the forward and backward scans and are shown at the top and bottom of Figure 6.10(a), respectively. Since the pinhole position is referenced to the first measurement point of each scan, only the relative position within each measurement is relevant. Both scan directions show a similar dependence of the resonance depth on the pinhole position, indicating that no pronounced scan-direction-dependent effect is present. However, an asymmetry of the resonance-depth curve is visible in both measurements.

To investigate whether this asymmetry originates from the pinhole itself, the measurement was repeated after rotating the pinhole by 180°. The corresponding measurements are shown in Figure 6.10(b). The upper measurement was performed with the same pinhole orientation as in Figure 6.10(a) and shows a similar asymmetric trend. After rotating the pinhole by 180°, shown in the lower measurement, the asymmetry is considerably reduced and the measured dependence agrees more closely with the expected symmetric behavior.

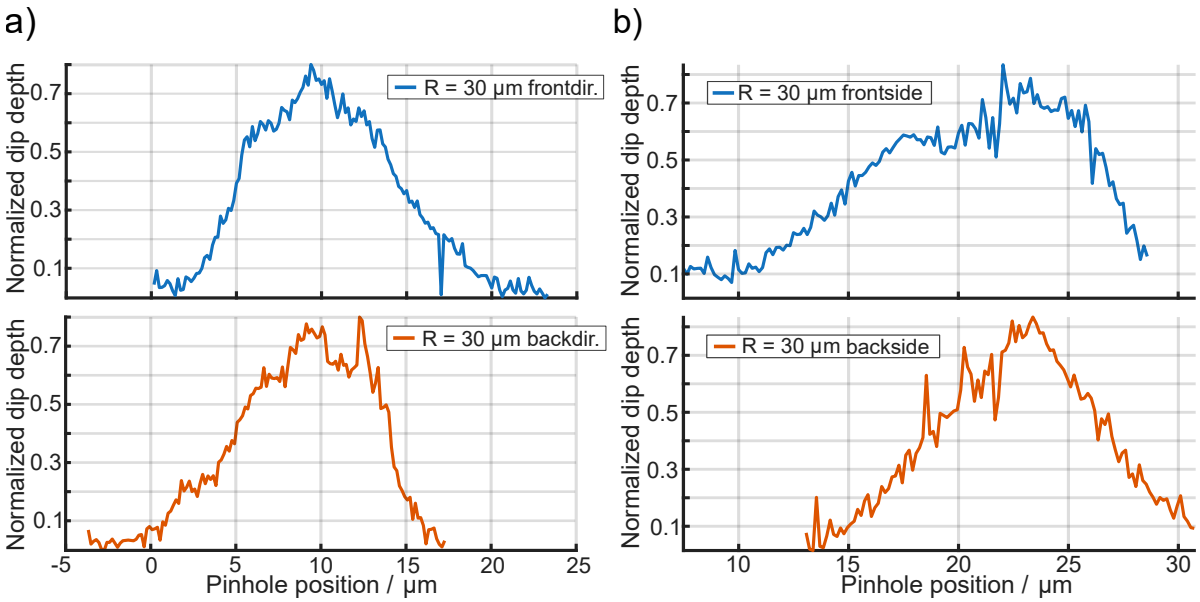


Figure 6.10: Reproducibility measurements of the pinhole method using a pinhole with a lateral diameter of 60 µm. The pinhole position is referenced to the starting position of each measurement. (a) Measurements performed with opposite scan directions. The upper measurement shows the pinhole translated from top to bottom, while the lower measurement shows the scan from bottom to top. Both measurements show a similar trend, indicating no pronounced dependence on the scan direction. An asymmetric resonance-depth dependence is visible in both cases. (b) Measurements performed with the same scan direction but pinhole orientations differing by 180°. The upper measurement was performed with the same orientation as in (a), while the lower measurement was obtained after rotating the pinhole by 180°. The asymmetry is considerably reduced for the rotated pinhole orientation.

The origin of this orientation-dependent asymmetry could not be identified conclusively. One possible explanation is an uneven polymer structure or an asymmetric pinhole geometry resulting from the printing process. Plasma ashing could potentially reduce remaining polymer structures at the pinhole

surface [84], while an additional metallic coating could make the surrounding structure fully opaque. These modifications were not investigated further within the available time.

As an additional consistency check, the FWHM extracted from each fitted resonance was evaluated. Increasing clipping loss introduced by the pinhole increases the total cavity loss and therefore broadens the cavity resonance, consistent with the relation between cavity loss and finesse given in Equation 2.8 and the relation between cavity finesse and linewidth in Equation 2.7. This is illustrated schematically in Figure 6.5. Starting from the central pinhole position, the FWHM is therefore expected to increase as the pinhole is displaced and the cavity mode becomes increasingly clipped.

The extracted FWHM values for the more symmetric measurement shown at the bottom of Figure 6.10(b) are presented in Figure 6.11(b). Around the central region, the linewidth follows the expected increase with increasing displacement from the center. For positions where the resonance depth approaches zero, the extracted FWHM fluctuates strongly and shows large uncertainties, since the resonance can no longer be identified reliably. The observed linewidth behavior therefore provides an additional consistency check for the resonance fits used in the pinhole evaluation.

To evaluate the cavity-mode position, the more symmetric measurement shown at the bottom of Figure 6.10(b) was analyzed further. Around the central maximum, the calculated resonance-depth dependence is approximately Gaussian-like. A Gaussian function according to Equation 5.1 was therefore used as an empirical fit to the measured resonance-depth values in the vicinity of the maximum. The resulting fit is shown in Figure 6.11(a). A reduced chi-squared value of $\chi^2_{\mathrm{red}} = 1.245$ was obtained, and the fitted central position had an uncertainty of 0.12 µm. This indicates that, for a sufficiently symmetric pinhole measurement, the cavity-mode center can be extracted with sub-micrometer fit precision.

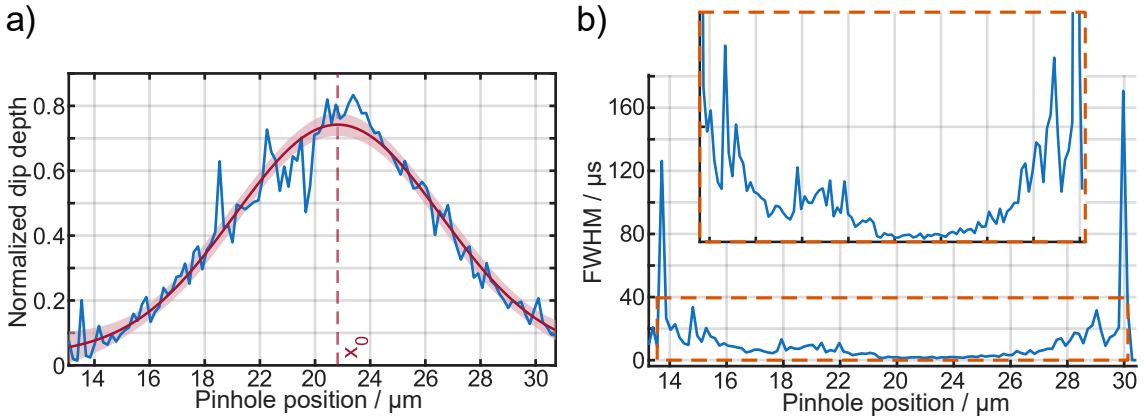


Figure 6.11: Evaluation of the pinhole measurement shown at the bottom of Figure 6.10(b). (a) Gaussian fit applied to the resonance-depth values around the central maximum. The fitted center position x_0 is used to determine the cavity-mode position. The corresponding 95 % confidence interval is indicated. (b) FWHM values extracted from the same resonance fits. Around the central region, the linewidth increases with increasing displacement of the pinhole from the center, as expected from the additional clipping loss introduced by the pinhole. At positions where the resonance becomes weak, the extracted FWHM shows increased fluctuations and uncertainties.

Based on these results, the pinhole method appears suitable for determining cavity-mode positions with sub-micrometer precision, provided that a sufficiently symmetric pinhole orientation is used. The reliability of the resonance identification and fitting could additionally be improved by reducing the noise level, for example by securing all fiber components more thoroughly. Its simultaneous application to two crossed high-finesse cavity modes remains to be demonstrated experimentally.

6.5 Current State and Remaining Challenges

At the end of this work, the mechanical platform, ferrule design, piezoelectric actuation scheme, and alignment procedure required for the crossed-cavity implementation had been prepared, while the final insertion and fixation of the fiber mirrors remained to be completed.

The next step is the insertion of two pairs of fiber mirrors into the crossed ferrule, forming one high-finesse cavity along each of the two orthogonal cavity axes. The cavity length of one axis has to be chosen larger than 120 µm, since the coated fibers have an outer diameter of about 135 µm. A cavity length of approximately 140 µm is therefore planned for the final implementation. The fibers then have to be fixed to the piezoelectric actuators and the additional ceramic supports.

After the two cavities have been formed, their optical performance has to be characterized. In particular, the achievable finesse, the cavity-length tuning range provided by the piezoelectric actuators, and the mechanical stability of the completed assembly remain to be evaluated experimentally.

The relative positions of the two cavity modes then have to be determined using the pinhole method developed above. The pinhole is translated through the central interaction region while the reflected resonance signals of both cavity axes are recorded simultaneously. By extracting the central pinhole position for each cavity mode, the relative displacement between the two cavity axes can be determined. While the method was successfully tested on a single cavity axis, its simultaneous application to two crossed high-finesse cavity modes remains to be demonstrated.

The remaining work therefore consists of completing the fiber insertion and fixation, characterizing the optical and mechanical performance of the two cavities, and finally verifying their relative cavity-mode alignment in the assembled device.

CHAPTER 7

Conclusion and Outlook

Throughout this work, assembly concepts for crossed fiber Fabry–Pérot cavities were developed and evaluated, with a focus on their application in photothermal gas sensing. Different approaches in which the relative fiber alignment is mechanically predefined by the assembly structure were investigated in order to assess whether orthogonal fiber axes can be positioned with sufficient precision and reproducibility.

Among the investigated concepts, the 3D-printed ferrule provided the most promising combination of relative alignment, reproducibility, and practical implementation. The enclosed printed channels provided highly reproducible relative fiber positioning, with measured beam-center displacements on the sub-micrometer scale, while still allowing the geometry to be adapted for optical access and piezoelectric cavity-length tuning. The calculated intensity overlap additionally showed that the remaining measured offsets are sufficiently small for both pump-beam–cavity and crossed-cavity configurations.

Several methods for characterizing the relative alignment were investigated. Conventional knife-edge measurements proved suitable for determining the relative positions of two crossed, freely propagating beams emitted from optical fibers and could in principle be extended to more complex fiber-alignment geometries involving more than two intersecting optical axes. For high-finesse cavity modes, where a conventional knife-edge evaluation is no longer directly applicable, a pinhole-based method was developed. The measurements showed that the cavity-mode center can be extracted with sub-micrometer fit precision under suitable conditions.

Based on these results, a final crossed-cavity platform consisting of a four-channel printed ferrule, four independently actuated fiber mirrors, and a dedicated ceramic base structure was designed and fabricated within this work, while the final insertion and fixation of the fiber mirrors remain to be completed.

Taken together, the results show that the developed assembly concepts are not limited to photothermal gas sensing. The mechanically predefined ferrule geometry provides a general means of defining the relative positions of several fiber axes or cavity modes within a common interaction region. The alignment methods investigated here are likewise applicable to orthogonal freely propagating fiber beams, high-finesse cavity modes, or combinations of both.

The DLW-fabricated ferrules are particularly versatile in this respect, since the number, orientation, and dimensions of the fiber channels can be adapted to the requirements of a specific experiment while retaining mechanically predefined relative alignment. The crossed four-channel ferrule and the T-shaped three-channel ferrule investigated here therefore represent only two possible implementations. More complex structures could combine cavity axes with additional pump or probe fibers or several intersecting optical cavities within a common three-dimensional interaction region.

7.1 Outlook

The most immediate next step is the completion of the three-channel T-shaped pump–cavity assembly. A fiber-mirror pair and the selected pump fiber have to be inserted and fixed within the ferrule. After successful assembly, the pump–cavity system should be characterized with respect to finesse, tuning range, and long-term stability. The relative alignment could additionally be re-evaluated using the pinhole method, with the cavity-mode position determined from the maximum resonance depth and the propagating pump-beam position from the maximum transmitted power. For this to work, a suitable pinhole diameter would have to be found first.

The final crossed-cavity assembly should then be completed. Two pairs of fiber mirrors have to be inserted into the four-channel ferrule and fixed to the piezoelectric actuators and ceramic supports. After forming two stable high-finesse cavities, their finesse, tuning range, long-term stability, and relative cavity-mode positions have to be evaluated. The latter can be determined by applying the pinhole method developed in this work simultaneously to both cavity modes.

Further optimization of the pinhole fabrication could focus on reducing the orientation-dependent asymmetry observed during the measurements. Improvements of the printing and post-processing procedure through plasma ashing and subsequent coating could provide a more symmetric aperture as well as a fully opaque pinhole for the operating wavelength and thereby increase the reproducibility of the extracted cavity-mode position.

For photothermal sensing, the three-channel pump–cavity configuration, in which a high-finesse cavity is used for optical readout and a freely propagating pump beam crosses the interaction region, is intended to be tested by the collaborating group. Mid-infrared specialty fibers could be used for pump delivery in order to address absorption transitions of atmospherically relevant gas species such as CO or nitrogen oxides [85]. In a subsequent crossed-cavity implementation, the second cavity could resonantly enhance the pump field. The resulting increase in intracavity pump intensity could increase the absorbed optical power and thereby enhance the photothermal signal, particularly for weakly absorbing species or low gas concentrations, for example methane, which exhibits absorption features near 1.6 µm.

Beyond photothermal sensing, the crossed-cavity geometry could also provide a valuable platform for experiments in atomic and molecular physics. A particular advantage is that the two resonators can be optimized independently for different functions. One cavity could be optimized for strong light–matter interaction with a selected atomic transition, while the perpendicular cavity provides a second independently tunable optical interface for excitation, state-dependent photon emission, heralding, or photon collection.

This provides an additional degree of freedom compared with a conventional single-cavity arrangement, where one resonator provides the cavity-enhanced light–matter interaction while additional optical fields are commonly introduced in free space. In the crossed configuration, the same emitter can instead interact with two independently tunable cavity modes. Such crossed cavities have already been demonstrated for coupling a single atom to two separate optical resonators [7].

As a concrete example, previous work at our institute has demonstrated fiber mirrors with radii of curvature down to approximately 40 µm [40]. For a symmetric cavity with $R = 40\,\mu\text{m}$, $L = 60\,\mu\text{m}$, and $\mathcal{F} = 1.5 \times 10^5$, the ideal single-atom cooperativity for the D_2 transition of ^{87}Rb is on the order of $C \approx 3.2 \times 10^3$, indicating strong coupling under ideal conditions (see Appendix A.6). The perpendicular cavity would require a larger mirror separation, but could still reach comparatively high cooperativity; for example, $L = 150\,\mu\text{m}$, $R = 300\,\mu\text{m}$, and the same finesse yield $C \approx 4 \times 10^2$. This allows the two cavities to be optimized independently for different wavelengths, transitions, linewidths, or mode sizes.

Beyond coupling to atomic or molecular transitions, the strongly confined optical field in the central interaction region could also be exploited for other light–matter interactions requiring high optical intensity within a small volume. Near-concentric Fabry–Pérot cavities have, for example, been used to generate very high continuous-wave intensities in a tightly confined interaction region and to manipulate electron waves through the resulting ponderomotive interaction [86, 87]. A crossed fiber-cavity platform could provide a miniaturized implementation of a related concept, in which a second optical or particle beam passes through the strongly enhanced field near the cavity center. The mechanically predefined crossing geometry could thereby be advantageous for compact experiments requiring strong and spatially localized field interactions.

A similar crossed-cavity approach could potentially be applied in molecular spectroscopy, where one cavity is optimized for excitation of a molecular transition while the second provides an independently optimized optical probe of the same interaction region.

This combination of adaptable 3D-printed ferrules, mechanically predefined relative alignment, and independently tunable cavity axes provides a promising basis for future compact experiments requiring several optical fields to interact within a common microscopic volume.

Bibliography

[1] A. Reiserer and G. Rempe,
Cavity-Based Quantum Networks with Single Atoms and Optical Photons,
Reviews of Modern Physics **87** (2015) 1379.

[2] T. E. Northup and R. Blatt, *Quantum Information Transfer Using Photons*,
Nature Photonics **8** (2014) 356, ISSN: 1749-4893.

[3] A. Kuhn, M. Hennrich and G. Rempe,
Deterministic Single-Photon Source for Distributed Quantum Networking,
Physical Review Letters **89** (2002) 067901.

[4] A. Reiserer, S. Ritter and G. Rempe, *Nondestructive Detection of an Optical Photon*,
Science **342** (2013) 1349, ISSN: 1095-9203.

[5] B. Hacker, S. Welte, G. Rempe and S. Ritter,
A Photon–Photon Quantum Gate Based on a Single Atom in an Optical Resonator,
Nature **536** (2016) 193, ISSN: 1476-4687.

[6] S. Ritter et al., *An Elementary Quantum Network of Single Atoms in Optical Cavities*,
Nature **484** (2012) 195, ISSN: 1476-4687.

[7] M. Brekenfeld, D. Niemietz, J. D. Christesen and G. Rempe,
A Quantum Network Node with Crossed Optical Fibre Cavities, Nature Physics **16** (2020) 647,
ISSN: 1745-2481.

[8] T. Steinmetz et al., *Stable Fiber-Based Fabry-Pérot Cavity*,
Applied Physics Letters **89** (2006) 111110, ISSN: 0003-6951.

[9] D. Hunger et al., *A Fiber Fabry–Perot Cavity with High Finesse*,
New Journal of Physics **12** (2010) 065038, ISSN: 1367-2630.

[10] D. Hunger, C. Deutsch, R. J. Barbour, R. J. Warburton and J. Reichel,
Laser Micro-Fabrication of Concave, Low-Roughness Features in Silica, 2011,
arXiv: 1109.5047 [physics.optics], (visited on 16/09/2026).

[11] J. Gallego et al.,
High-Finesse Fiber Fabry–Perot Cavities: Stabilization and Mode Matching Analysis,
Applied Physics B **122** (2016) 47, ISSN: 1432-0649.

[12] H. Pfeifer et al., *Achievements and Perspectives of Optical Fiber Fabry–Perot Cavities*,
Applied Physics B **128** (2022) 29, ISSN: 1432-0649.

[13] L. Tenbrake et al.,
Direct Laser-Written Optomechanical Double Membranes in an Optical Microcavity, 2026, arXiv: 2609.01145 [physics.optics], (visited on 18/09/2026).

[14] L. Tenbrake, A. Faßbender, S. Hofferberth, S. Linden and H. Pfeifer,
Direct Laser-Written Optomechanical Membranes in Fiber Fabry-Perot Cavities, Nature Communications **15** (2024) 209, ISSN: 2041-1723.

[15] R. Gehr et al., *Cavity-Based Single Atom Preparation and High-Fidelity Hyperfine State Readout*, Physical Review Letters **104** (2010) 203602.

[16] J. Gallego et al., *Strong Purcell Effect on a Neutral Atom Trapped in an Open Fiber Cavity*, Physical Review Letters **121** (2018) 173603, ISSN: 1079-7114.

[17] M. Steiner, H. M. Meyer, C. Deutsch, J. Reichel and M. Köhl,
Single Ion Coupled to an Optical Fiber Cavity, Physical Review Letters **110** (2013) 043003.

[18] F. Rochau et al., *Dynamical Backaction in an Ultrahigh-Finesse Fiber-Based Microcavity*, Physical Review Applied **16** (2021) 014013.

[19] C. Saavedra, D. Pandey, W. Alt, D. Meschede and H. Pfeifer,
Spectroscopic Gas Sensor Based on a Fiber Fabry-Perot Cavity,
Physical Review Applied **18** (2022) 044039.

[20] C. Saavedra, D. Pandey, W. Alt, H. Pfeifer and D. Meschede,
Tunable Fiber Fabry-Perot Cavities with High Passive Stability, Optics Express **29** (2021) 974, ISSN: 1094-4087.

[21] J. Hodgkinson and R. P. Tatam, *Optical Gas Sensing: A Review*,
Measurement Science and Technology **24** (2012) 012004, ISSN: 0957-0233.

[22] K. Krzempek, *A Review of Photothermal Detection Techniques for Gas Sensing Applications*, Applied Sciences **9** (2019) 2826, ISSN: 2076-3417.

[23] W. Jin et al.,
Recent Advances in Spectroscopic Gas Sensing With Micro/Nano-Structured Optical Fibers, Photonic Sensors **11** (2021) 141, ISSN: 1674-9251.

[24] Y. Lin et al., *Pulsed Photothermal Interferometry for Spectroscopic Gas Detection with Hollow-Core Optical Fibre*, Scientific Reports **6** (2016) 39410, ISSN: 2045-2322.

[25] Z. Li, Z. Wang, F. Yang, W. Jin and W. Ren,
Mid-Infrared Fiber-Optic Photothermal Interferometry, Optics Letters **42** (2017) 3718, ISSN: 1539-4794.

[26] J. P. Waclawek, C. Kristament, H. Moser and B. Lendl,
Balanced-Detection Interferometric Cavity-Assisted Photothermal Spectroscopy,
Optics Express **27** (2019) 12183, ISSN: 1094-4087.

[27] D. Pinto et al., *Wavelength Modulated Diode Probe Laser for an Interferometric Cavity-Assisted Photothermal Spectroscopy Gas Sensor*, Sensors and Actuators B: Chemical **377** (2023) 133061, ISSN: 0925-4005.

[28] K. Krzempek et al., *Photothermal Gas Detection Using a Miniaturized Fiber Fabry-Perot Cavity*, Sensors and Actuators B: Chemical **401** (2024) 135040, ISSN: 09254005.

[29] Y. Yan et al., *Nanoliter-Scale Light–Matter Interaction in a Fiber-Tip Cavity Enables Sensitive Photothermal Gas Detection*, Laser & Photonics Reviews **18** (2024) 2400907, ISSN: 1863-8899.

[30] G. Malvicini et al., *Balanced-Detection Interferometric Cavity-Assisted Photothermal Spectroscopy via Collimating Fiber-Array Integration*, Sensors and Actuators B: Chemical **412** (2024) 135766, ISSN: 0925-4005.

[31] T. He, W. Wang, B.-G. He and J. Chen, *Review on Optical Fiber Sensors for Hazardous-Gas Monitoring in Mines and Tunnels*, IEEE Transactions on Instrumentation and Measurement **72** (2023) 1, ISSN: 1557-9662.

[32] Y. Tan, W. Jin, F. Yang, Y. Jiang and H. L. Ho, *Cavity-Enhanced Photothermal Gas Detection With a Hollow Fiber Fabry-Perot Absorption Cell*, Journal of Lightwave Technology **37** (2019) 4222, ISSN: 1558-2213.

[33] A. E. Siegman, *Lasers*, University Science Books, 1986, ISBN: 978-0-935702-11-8.

[34] J. C. Gallego, *Strong Coupling between Small Atomic Ensembles and an Open Fiber Cavity*, PhD thesis: University of Bonn, 2017.

[35] C. A. S. Salazar, *Development of Tunable Fiber Fabry-Pérot Micro-Resonators with High Passive Stability: A Demonstration for Molecular Oxygen Gas Spectroscopy*, PhD thesis: Universidad De Guanajuato, 2022.

[36] W. B. Joyce and B. C. DeLoach, *Alignment of Gaussian Beams*, Applied Optics **23** (1984) 4187, ISSN: 2155-3165.

[37] J. Schwab et al., *Coupling Light Emission of Single-Photon Sources into Single-Mode Fibers: Mode Matching, Coupling Efficiencies, and Thermo-Optical Effects*, Optics Express **30** (2022) 32292, ISSN: 1094-4087.

[38] R. Director, *Specialty Optical Fibers & Custom Manufacturing | IVG*, https://www.ivgfiber.com/, (visited on 02/10/2026).

[39] M. Uphoff, M. Brekenfeld, G. Rempe and S. Ritter, *Frequency Splitting of Polarization Eigenmodes in Microscopic Fabry–Perot Cavities*, New Journal of Physics **17** (2015) 013053, ISSN: 1367-2630.

[40] J. D. Spanier, *A Fiber-Based Microcavity for Strong Coupling of Excitons*, MA thesis: University of Bonn, 2026.

[41] *Bonn FiberLab*, https://www.physik-astro.uni-bonn.de/fiberlab/en, (visited on 02/10/2026).

[42] M. A. Scharfstaedt, *Implementation of a Micro-Mirror Production Setup for Quantum Information Applications*, MA thesis: University of Bonn, 2022.

[43] S. Kobayashi, N. Otsu, T. Kikuta and T. Hayashi, *Handheld Angle Fiber Cleaver*, 2011.

[44] *LAYERTEC: Your Partner for Optical Components for Laser Applications*, https://www.layertec.de/en/, (visited on 21/09/2026).

[45] T. Kawanishi, *Electro-Optic Modulation for Photonic Networks: Precise and High-Speed Control of Lightwaves*, Textbooks in Telecommunication Engineering, Cham: Springer International Publishing, 2022, ISBN: 978-3-030-86719-5 978-3-030-86720-1.

[46] J. Blechmann, *A Fiber Fabry-Perot Cavity for Photothermal Gas Detection*, BA Thesis: University of Bonn, 2024.

[47] *Nanoscribe GmbH & Co. KG*, https://www.nanoscribe.com/en/, (visited on 05/10/2026).

[48] *Nanoscribe - Nanoguide*, https://support.nanoscribe.com/, (visited on 20/07/2026).

[49] H.-B. Sun and S. Kawata, "Two-Photon Photopolymerization and 3D Lithographic Microfabrication", *NMR • 3D Analysis • Photopolymerization*, ed. by N. Fatkullin et al., Berlin, Heidelberg: Springer, 2004 169, ISBN: 978-3-540-40000-4.

[50] D. Stachanow, *Manufacturing Q-Optimized Polymer-Based Mechanical Resonators for Cavity Optomechanics with 3D Direct Laser Writing*, MA thesis: University of Bonn, 2024.

[51] *Carl ROTH Deutschland | Startseite*, https://www.carlroth.com/de/de, (visited on 10/10/2026).

[52] D. C. Meisel et al., *Shrinkage Precompensation of Holographic Three-Dimensional Photonic-Crystal Templates*, Advanced Materials **18** (2006) 2964, ISSN: 1521-4095.

[53] "Fiber Optic Measurement Techniques", Elsevier, 2009, ISBN: 978-0-12-373865-3.

[54] A. D. Rakić, A. B. Djurišić, J. M. Elazar and M. L. Majewski, *Optical Properties of Metallic Films for Vertical-Cavity Optoelectronic Devices*, Applied Optics, Vol. 37, Issue 22, pp. 5271-5283 (1998).

[55] C. Jäger, T. Henning, R. Schlögl and O. Spillecke, *Spectral Properties of Carbon Black*, Journal of Non-Crystalline Solids **258** (1999) 161, ISSN: 0022-3093.

[56] *Carbon black, 10 g, CAS Nr. 1333-86-4 &#11166 Carlroth SPA - Deutschland*, https://www.carlroth.com/de/de/p/21LP.1, (visited on 17/09/2026).

[57] A. Paliwal et al., *Efficient Semitransparent Perovskite Solar Cells Based on Thin Compact Vacuum Deposited CH3NH3PbI3 Films*, Advanced Materials Interfaces **9** (2022) 2201222, ISSN: 2196-7350.

[58] X. M. Dong et al., *Effects of Processing on Electric Response of Carbon Black Filled Poly(Methyl Methacrylate) Composites against Organic Solvent Vapors*, Polymer Journal **35** (2003) 1003, ISSN: 1349-0540.

[59] E. A. Sousa, A. Gonçalves Junior, E. P. S. Arlindo and G. C. Fuzari Junior, *Electrical Conduction Mechanisms of Poly(Methyl Methacrylate) Conductive Composite Films with Carbon Black Conductive Particles*, Results in Materials **31** (2026) 100994, ISSN: 2590-048X.

[60] P. Eze-Idehen and K. Persaud, *Design, Fabrication and Validation of Chemical Sensors for Detecting Hydrocarbons to Facilitate Oil Spillage Remediation*, Chemosensors **13** (2025) 140, ISSN: 2227-9040.

[61] P. Bevington and D. K. Robinson, *Data Reduction and Error Analysis for the Physical Sciences*, McGraw-Hill Education, 2003, ISBN: 978-0-07-247227-1.

[62] Y. Suzaki and A. Tachibana, *Measurement of the μm Sized Radius of Gaussian Laser Beam Using the Scanning Knife-Edge*, Applied Optics, Vol. 14, Issue 12, pp. 2809-2810 (1975).

[63] D. R. Skinner and R. E. Whitcher,
Measurement of the Radius of a High-Power Laser Beam near the Focus of a Lens,
Journal of Physics E: Scientific Instruments **5** (1972) 237, ISSN: 0022-3735.

[64] H. R. Bilger and T. Habib, *Knife-Edge Scanning of an Astigmatic Gaussian Beam*,
Applied Optics **24** (1985) 686, ISSN: 2155-3165.

[65] M. González-Cardel, P. Arguijo and R. Díaz-Uribe, *Gaussian Beam Radius Measurement with a Knife-Edge: A Polynomial Approximation to the Inverse Error Function*,
Applied Optics **52** (2013) 3849, ISSN: 2155-3165.

[66] J. L. Carthy, P. C. Gow, S. A. Berry, B. Mills and V. Apostolopoulos,
Terahertz Focusing and Polarization Control in Large-Area Bias-Free Semiconductor Emitters,
Journal of Infrared, Millimeter, and Terahertz Waves **39** (2018) 223, ISSN: 1866-6906.

[67] C. Huber, S. Orlov, P. Banzer and G. Leuchs,
Corrections to the Knife-Edge Based Reconstruction Scheme of Tightly Focused Light Beams,
Optics Express **21** (2013) 25069, ISSN: 1094-4087.

[68] *Thorlabs · WC100 Clean-Out Wires, Ø110 µm (8 Per Vial)*,
https://www.thorlabs.com/item/WC100, (visited on 17/09/2026).

[69] *Linear Motor Positioning Stage - Motorized Positioners & Controllers - Catalog - Opto-Mechanical Products - Standa*,
https://www.standa.lt/products/catalog/motorised_positioners?item=63, (visited on 17/09/2026).

[70] D. J. Merthe et al.,
"An Experimental Apparatus for Diffraction-Limited Soft x-Ray Nano-Focusing",
SPIE Optical Engineering + Applications, ed. by C. Morawe, A. M. Khounsary and S. Goto, San Diego, California, USA, 2011 813907.

[71] R. Zameroski, M. Gomez and T. Schmitz,
Geometry-Based, Gaussian Profile Model for Optical Knife-Edge Displacement Sensor,
Precision Engineering **73** (2022) 470, ISSN: 01416359.

[72] *How to Model Angle-Cleaved Fibers*, https://optics.ansys.com/hc/en-us/articles/42661821960851-How-to-model-angle-cleaved-fibers, (visited on 02/09/2026).

[73] *CT50-Data-Sheet*,
https://www.europe.fujikura.com/wp-content/uploads/2026/03/CT50-data-sheet.pdf,
(visited on 16/09/2026).

[74] M. Saravanan, *Mode-Matched Fiber Fabry-Pérot Cavities for Quantum Technologies*,
MA thesis: University of Bonn, 2020.

[75] T. B. Beck, *Design and Fabrication of Microscopic 3D Printed Fiber Tip Lenses for Atomic Quantum Technology*, MA thesis: University of Bonn, 2025.

[76] M. Tanzer, B. Lang and A. Bergmann, *Collinear Photothermal Gas Sensing With a Custom-Made Dichroic and Fiber-Coupled Fabry-Pérot Etalon*, IEEE Sensors Journal **25** (2025) 24257,
ISSN: 1530-437X, 1558-1748, 2379-9153.

[77] *Thorlabs · IRFS32 Single Mode InF3 Fiber, 3.2 - 5.5 µm, 0.26 NA, 11.0 µm MFD*,
https://www.thorlabs.com/item/IRFS32, (visited on 18/09/2026).

[78] D. Hils and J. L. Hall, *Response of a Fabry–Perot Cavity to Phase Modulated Light*, Review of Scientific Instruments **58** (1987) 1406, ISSN: 0034-6748.

[79] C. C. Davis and S. J. Petuchowski, *Phase Fluctuation Optical Heterodyne Spectroscopy of Gases*, Applied Optics, Vol. 20, Issue 14, pp. 2539-2554 (1981).

[80] K. Krzempek et al., *Multi-Pass Cell-Assisted Photoacoustic/Photothermal Spectroscopy of Gases Using Quantum Cascade Laser Excitation and Heterodyne Interferometric Signal Detection*, Applied Physics B **124** (2018) 74, ISSN: 1432-0649.

[81] *Thorlabs · PL5FBP3 Shear Piezo Chip, ±200 V, 1.3 µm Displacement, 5.0 × 5.0 × 1.8 Mm, Flat End Plates*, https://www.thorlabs.com/item/PL5FBP3, (visited on 17/09/2026).

[82] A. Heinz et al., *Crossed Optical Cavities with Large Mode Diameters*, Optics Letters **46** (2021) 250, ISSN: 1539-4794.

[83] W. J. Hughes, T. H. Doherty, J. A. Blackmore, P. Horak and J. F. Goodwin, *Mode Mixing and Losses in Misaligned Microcavities*, Optics Express **31** (2023) 32619, ISSN: 1094-4087.

[84] J. M. Elorrieta et al., *Influence of Oxygen Plasma on the Material Properties of Two-Photon Polymerized Microstructures*, Materials & Design **261** (2026) 115357, ISSN: 0264-1275.

[85] Q. Nie et al., *Sub-Ppt Level Detection of Carbon Monoxide and Nitrous Oxide Enabled by Mid-Infrared Doubly Resonant Photoacoustic Spectroscopy*, Optics Letters **49** (2024) 3648, ISSN: 1539-4794.

[86] O. Schwartz et al., *Near-Concentric Fabry-Pérot Cavity for Continuous-Wave Laser Control of Electron Waves*, Optics Express **25** (2017) 14453, ISSN: 1094-4087.

[87] O. Schwartz et al., *Laser Phase Plate for Transmission Electron Microscopy*, Nature Methods **16** (2019) 1016, ISSN: 1548-7105.

[88] *IKA RCT basic IKAMAG safety control universal hot plate magnetic stirrer, 20 L, 1500 rpm, 230 V, 1/cs lab stirrers*, https://www.sigmaaldrich.com/DE/de/product/aldrich/z645060, (visited on 24/07/2026).

[89] *Alkali D Line Data - Rubidium87numbers.Pdf*, https://steck.us/alkalidata/rubidium87numbers.pdf, (visited on 18/09/2026).

APPENDIX A

Appendix

A.1 Optical Mode Matching

One key factor influencing the intensity of the detected reflection signal is the spatial overlap between the electric field emerging from the incoupling fiber and the cavity field. The degree to which both field distributions match can be quantified using the spatial mode-overlap integral [36, 37]:

$$\eta_{\mathrm{MM}} = \frac{\left| \iint_{\mathbb{R}^2} E_{\mathrm{f}}^*(x,y) E_{\mathrm{c}}(x,y)\, \mathrm{d}x\, \mathrm{d}y \right|^2}{\left(\iint_{\mathbb{R}^2} \left| E_{\mathrm{f}}(x,y) \right|^2 \mathrm{d}x\, \mathrm{d}y \right) \left(\iint_{\mathbb{R}^2} \left| E_{\mathrm{c}}(x,y) \right|^2 \mathrm{d}x\, \mathrm{d}y \right)}, \tag{A.1}$$

where $E_{\mathrm{f}}(x,y)$ and $E_{\mathrm{c}}(x,y)$ denote the electric-field distributions of the incoupling fiber mode and the cavity mode, respectively. The normalization is chosen such that perfect mode matching corresponds to $\eta_{\mathrm{MM}} = 1$, while any imperfect overlap results in $0 \leq \eta_{\mathrm{MM}} < 1$. The quantity η_{MM} is referred to as the mode-matching efficiency.

The spatial mode overlap depends on several properties of the fiber mode, the cavity mode, and their relative alignment. To estimate the influence of the individual contributions, the mode-matching efficiency can be approximated as the product of separate factors. This factorization is sufficient for the estimates presented here. However, the complete overlap integral in Equation A.1 must generally be evaluated when an exact description is required.

The approximate factorized mode-matching efficiency is written as [11, 37]

$$\eta_{\mathrm{MM}} \approx \eta_0\, \eta_\theta\, \eta_d \tag{A.2}$$

where η_0 describes the overlap for perfect lateral and angular alignment, η_d accounts for a lateral displacement between the fiber and cavity modes, and η_θ accounts for an angular mismatch between their propagation axes. The individual contributions are discussed below.

Beam-Shape Mismatch

The factor η_0 describes the mode-matching efficiency for perfect lateral and angular alignment, corresponding to $d = 0$ and $\theta = 0$. Under these conditions, the overlap depends only on the beam sizes and

wavefront curvatures of the fiber and cavity modes and the mode-matching efficiency in case of a fiber cavity can be expressed as [9]

$$\eta_0 = \frac{4}{\left(\frac{w_\mathrm{f}}{w_{\mathrm{m},1}} + \frac{w_{\mathrm{m},1}}{w_\mathrm{f}}\right)^2 + \left(\frac{k w_\mathrm{f} w_{\mathrm{m},1}}{2R_1}\right)^2}, \tag{A.3}$$

where $w_\mathrm{f} = \mathrm{MFD}/2$ is the mode radius of the field emerging from the incoupling fiber and $w_{\mathrm{m},1}$ is the cavity-mode radius at the incoupling mirror. Furthermore, R_1 is the radius of curvature of the incoupling mirror and $k = 2\pi/\lambda$ is the wave number. The first term in the denominator accounts for the mismatch in beam radii, while the second describes the mismatch in wavefront curvature.

The cavity-mode radius at the first mirror is given by

$$w_{\mathrm{m},1}^2 = \frac{\lambda}{\pi}\sqrt{\frac{L R_1^2 \left(R_2 - L\right)}{\left(R_1 - L\right)\left(R_1 + R_2 - L\right)}}, \tag{A.4}$$

where L is the cavity length and R_1 and R_2 are the radii of curvature of the two cavity mirrors. While w_f is determined by the optical fiber, $w_{\mathrm{m},1}$ depends on the cavity geometry. The mode-matching efficiency therefore increases when both the beam radius and wavefront curvature of the cavity mode approach those of the fiber mode.

Angular Mismatch

For an angular mismatch $\theta \neq 0$, the cavity-mode axis is tilted relative to the axis of the incoupling mode. Such a mismatch can arise, for example, when the fiber end facet has a nonzero cleave angle and the laser-machined mirror depression is oriented relative to this tilted surface, as illustrated in Figure 3.2(d). The resulting efficiency factor can be written as [37]

$$\eta_\theta = \exp\left[-\frac{\theta^2 \eta_0}{2}\left(\frac{\pi^2}{\lambda^2}\left[w_{0,\mathrm{f}}^2 + w_{0,\mathrm{c}}^2\right] + \frac{z_\mathrm{f}^2}{w_{0,\mathrm{f}}^2} + \frac{z_\mathrm{c}^2}{w_{0,\mathrm{c}}^2}\right)\right], \tag{A.5}$$

where θ denotes the angle between the fiber-mode and cavity-mode axes. The quantities $w_{0,\mathrm{f}}$ and $w_{0,\mathrm{c}}$ are the corresponding waist radii, while z_f and z_c denote the distances between the respective waist positions and the alignment plane.

Lateral Mismatch

A lateral displacement of the cavity-mode axis relative to the incoupling-mode axis introduces an additional reduction in mode-matching efficiency. Such a displacement can result from an offset between the center of the laser-machined mirror depression and the fiber core, as illustrated in Figure 3.2(c). This offset occurred frequently during the fabrication run of the fibers used in this work. The corresponding efficiency factor is given by [37]

$$\eta_d = \exp\left[-\frac{d^2 \eta_0}{2}\left(\frac{1}{w_{0,\mathrm{f}}^2} + \frac{1}{w_{0,\mathrm{c}}^2}\right)\right], \tag{A.6}$$

where d is the lateral displacement between the fiber-mode and cavity-mode axes. As an example, the mode-matching efficiency is estimated for a cavity geometry representative of this work.

The cavity and fiber parameters are

$$\begin{aligned} R_1 &= 290\,\mu\text{m}, \quad R_2 = 310\,\mu\text{m}, \\ L &= 120\,\mu\text{m}, \quad \lambda = 1.55\,\mu\text{m}, \\ w_\text{f} &= 4.5\,\mu\text{m}, \quad \theta = 0.5^\circ. \end{aligned}$$

Using the cavity geometry introduced above, the corresponding cavity waist, mode radii at the two mirrors, and distances between the cavity waist and the mirrors are

$$\begin{aligned} w_0 &= 7.689\,\mu\text{m}, \quad w_{\text{m},1} = 8.697\,\mu\text{m}, \quad w_{\text{m},2} = 8.505\,\mu\text{m}, \\ z_{\text{c},1} &= 63.333\,\mu\text{m}, \quad z_{\text{c},2} = 56.667\,\mu\text{m}. \end{aligned}$$

Using Equation A.3, with the indices exchanged accordingly for coupling through mirror 2, the mode-matching efficiencies for perfect lateral and angular alignment are

$$\eta_{0,1} = 0.6582, \qquad \eta_{0,2} = 0.6763.$$

For the angular contribution, the fiber-mode waist is assumed to be located at the fiber facet, such that $z_\text{f} = 0$ and $w_{0,\text{f}} = w_\text{f}$. Using Equation A.5 for an angular mismatch of $\theta = 0.5^\circ$ gives

$$\eta_{\theta,1} = 0.99018, \qquad \eta_{\theta,2} = 0.99025.$$

The lateral contribution is calculated using Equation A.6. Combining the beam-shape, angular, and lateral contributions according to Equation A.2 gives the total mode-matching efficiencies summarized in Table A.1.

Table A.1: Combined spatial mode-matching efficiencies for an angular mismatch of $\theta = 0.5^\circ$ and different lateral displacements d.

d	$\eta_{\text{MM},1}$	$\eta_{\text{MM},2}$
0 µm	0.6517	0.6697
1 µm	0.6376	0.6548
2 µm	0.5972	0.6122
3 µm	0.5355	0.5473
5 µm	0.3777	0.3824

A.2 Mirror Coating

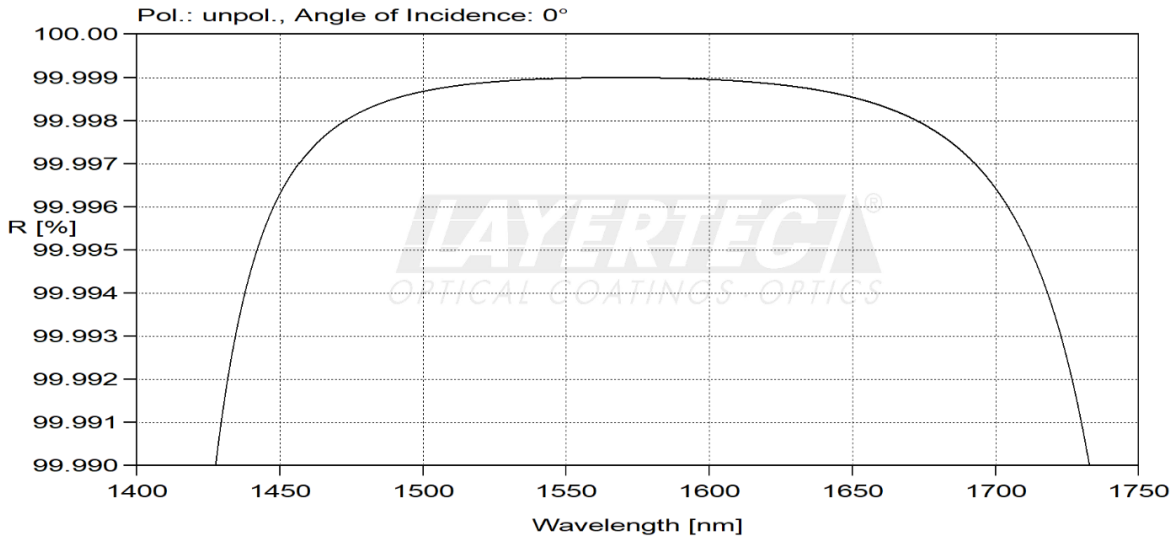


Figure A.1: Reflection percentage of the coating for different wavelengths under normal incidence, specified by the manufacturer Layertec [44].

A.3 Additional Printing Images

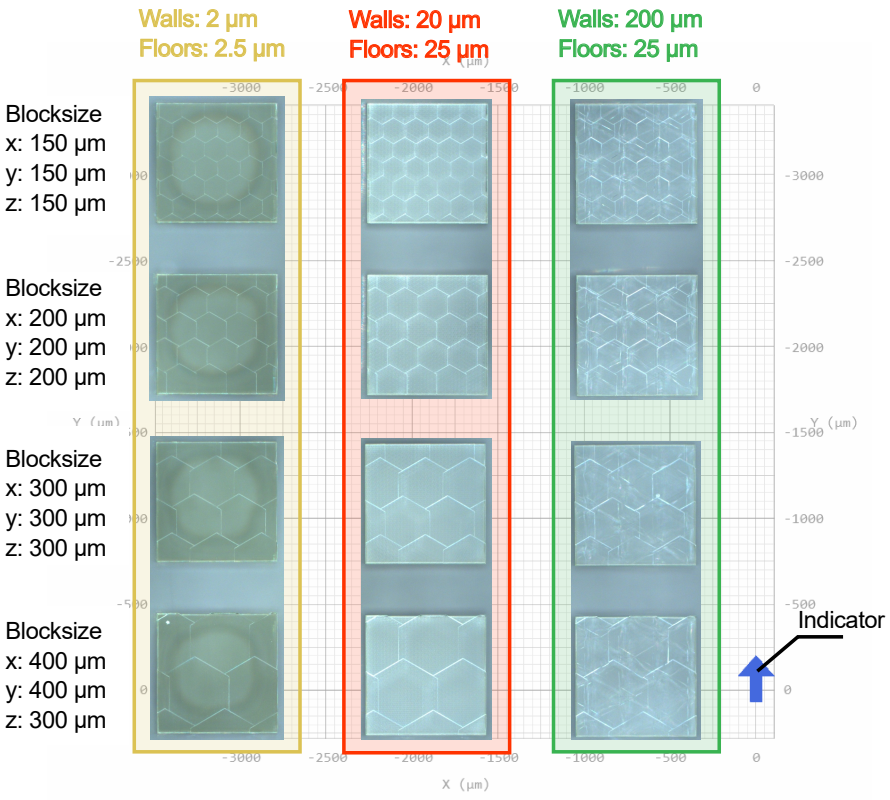


Figure A.2: Top view of the block-size and scaffold-setting sweep. Each column corresponds to a different block size, indicated on the left. Each row corresponds to a different scaffold spacing. The wall spacing denotes the distance between the vertical scaffold lines, while the floor spacing denotes the distance between the horizontal scaffold lines. An orientation arrow is included for reference.

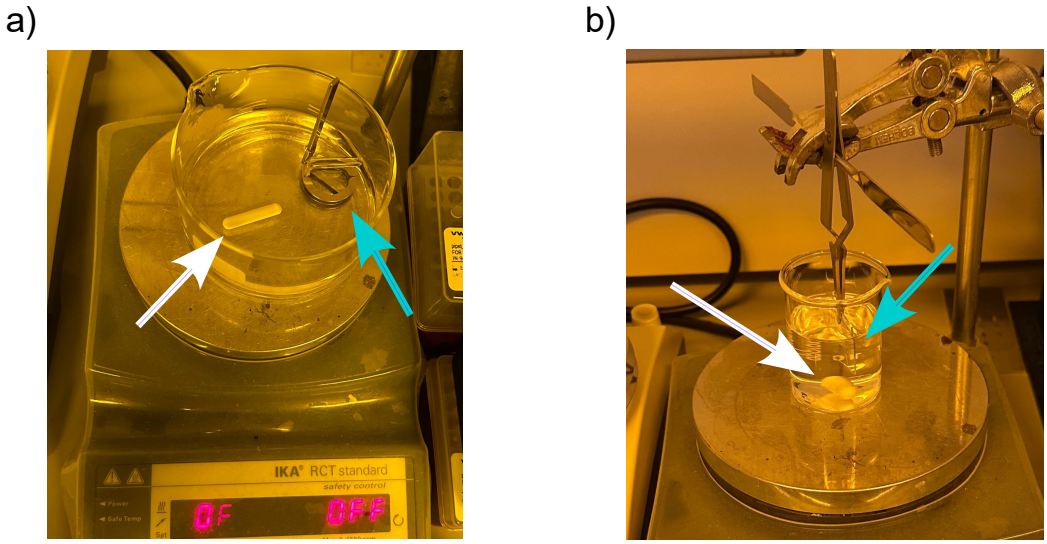


Figure A.3: Development setups using a magnetic stirring bar [88]. (a) The magnetic stirring bar, indicated by the white arrow, is positioned next to the print, indicated by the blue arrow. (b) The magnetic stirring bar is positioned beneath the print.

A.4 Engineering Drawings

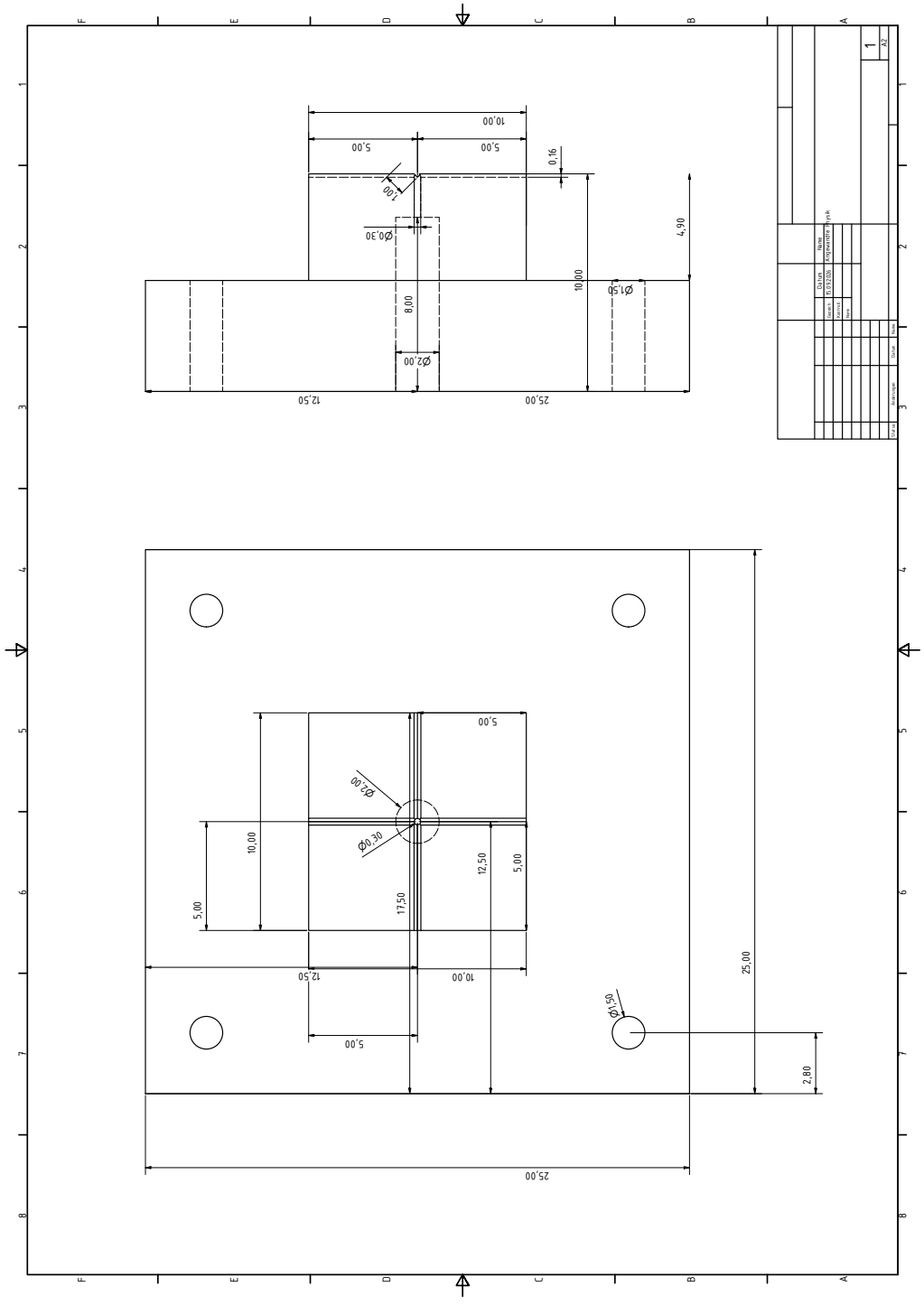


Figure A.4: Engineering drawing of the grooved ceramic block including the relevant dimensions. The block has a footprint of 25 mm × 25 mm. A centered pedestal with an area of 10 mm × 10 mm and a height of 4.9 mm is located on the top surface. The fiber grooves are 160 µm deep and have an opening angle of 90°. A centered through-hole is introduced from the bottom side. Over the first 2 mm, the hole has a diameter of 2 mm; above this section, the diameter is reduced to 300 µm and the hole continues through the grooved top surface.

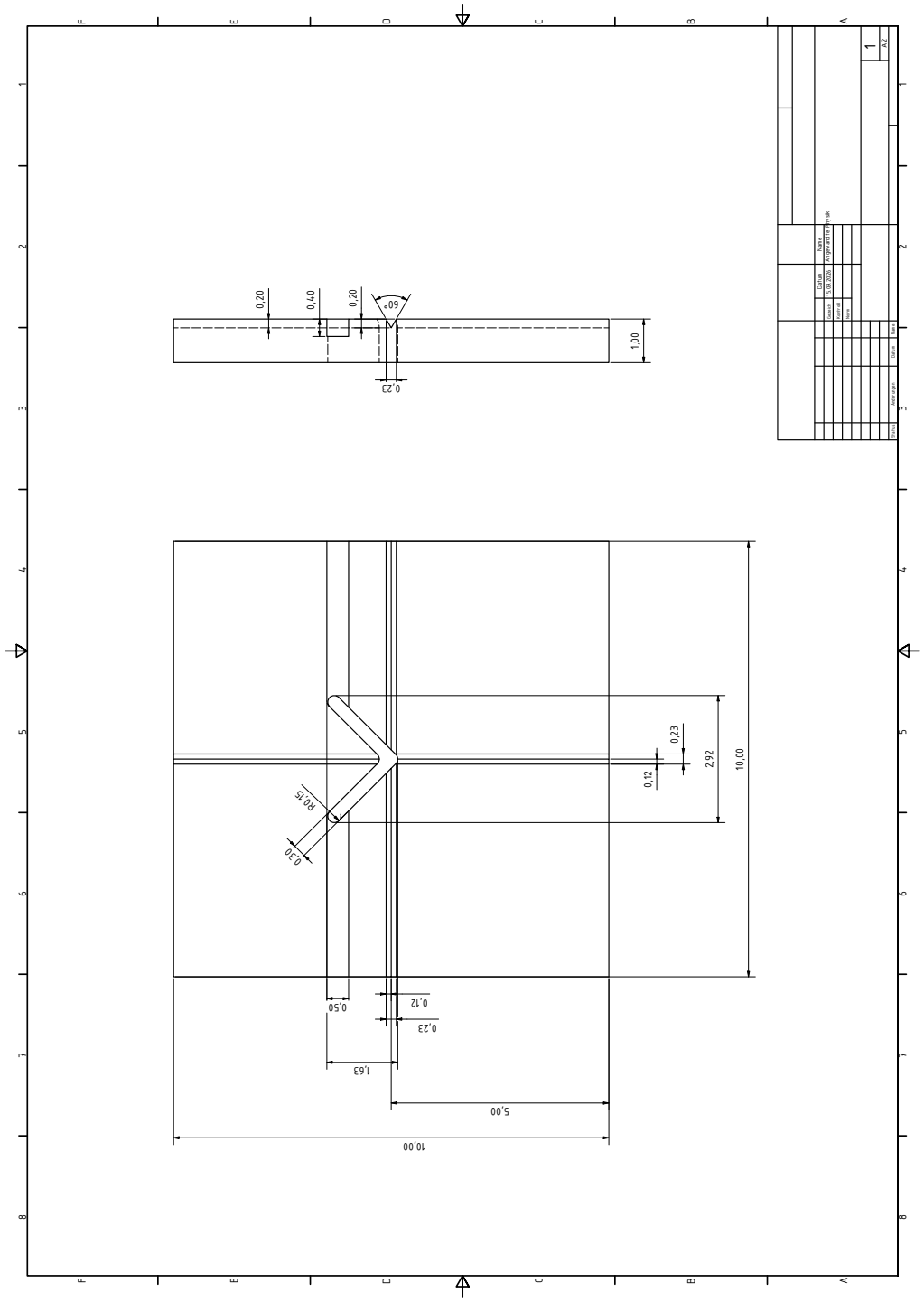


Figure A.5: Engineering drawing of the grooved ceramic plate including the relevant dimensions. The plate has a footprint of 10 mm × 10 mm and a thickness of 1 mm. The fiber grooves are 200 µm deep and have an opening angle of 60°. A V-shaped opening is introduced through the center of the plate to facilitate later separation. The opening has a minimum width of 300 µm and increases to a width of 2.92 mm. From both sides of the opening, recesses with a width of 0.5 mm and a depth of 0.4 mm extend towards the outer edges of the plate.

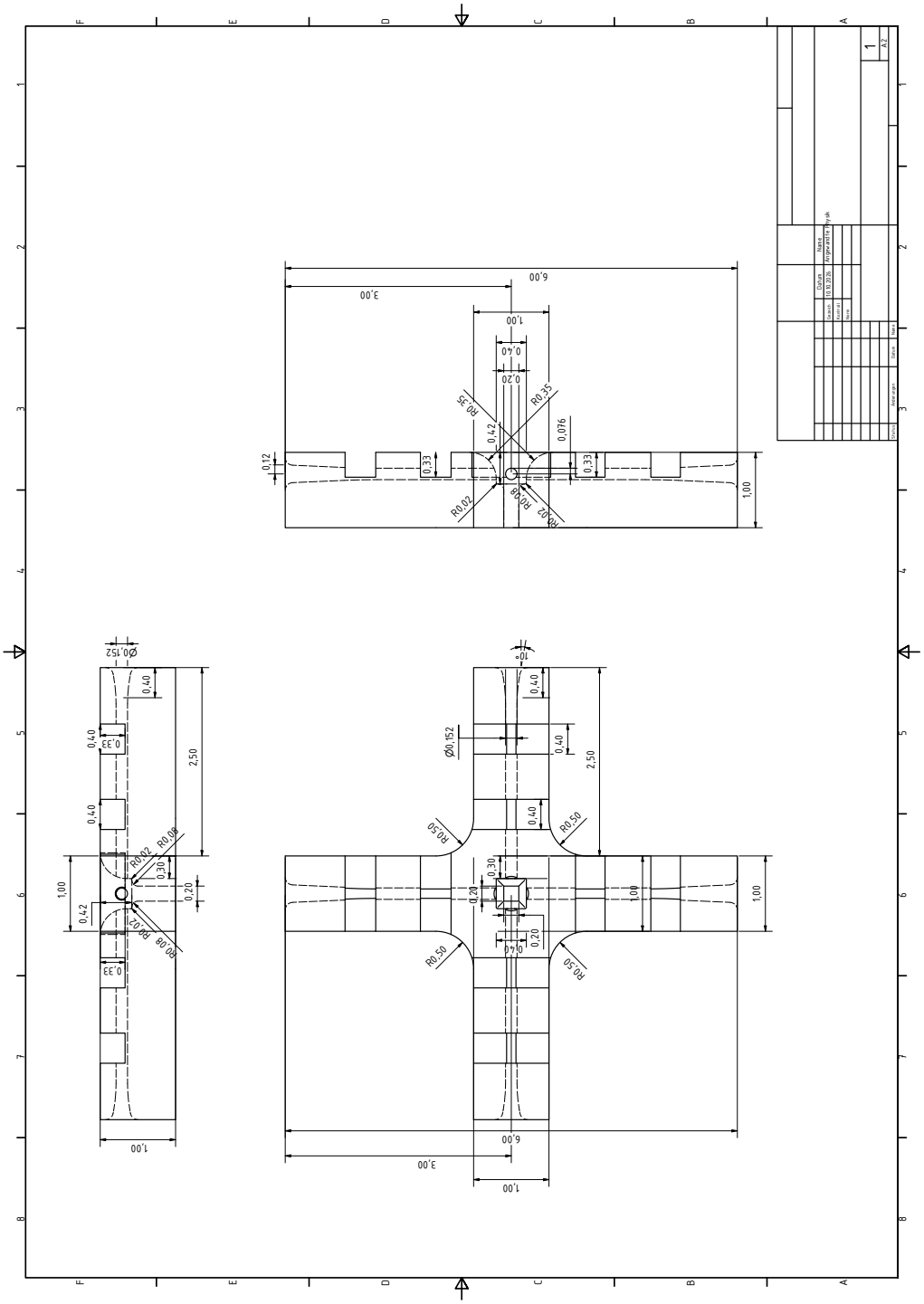


Figure A.6: Engineering drawing of the final four channel cross ferrule including all specific dimensions. Each channel extends 3 mm from the central cavity region and has a diameter of 152 µm. The channels are supported by printed arms with a cross section of 1 mm × 1 mm. Additional openings with a width of 0.4 mm extend into the channels to improve the accessibility of the developer during flushing. The central cavity region has the same width. An additional opening with a cross section of 0.2 mm × 0.2 mm provides out-of-plane optical access to the cavity region. Curved transitions at the upper cavity opening increase the accessible observation angles, while identical reinforcing curvatures at the outer arm connections improve mechanical stability and preserve the symmetry of the ferrule.

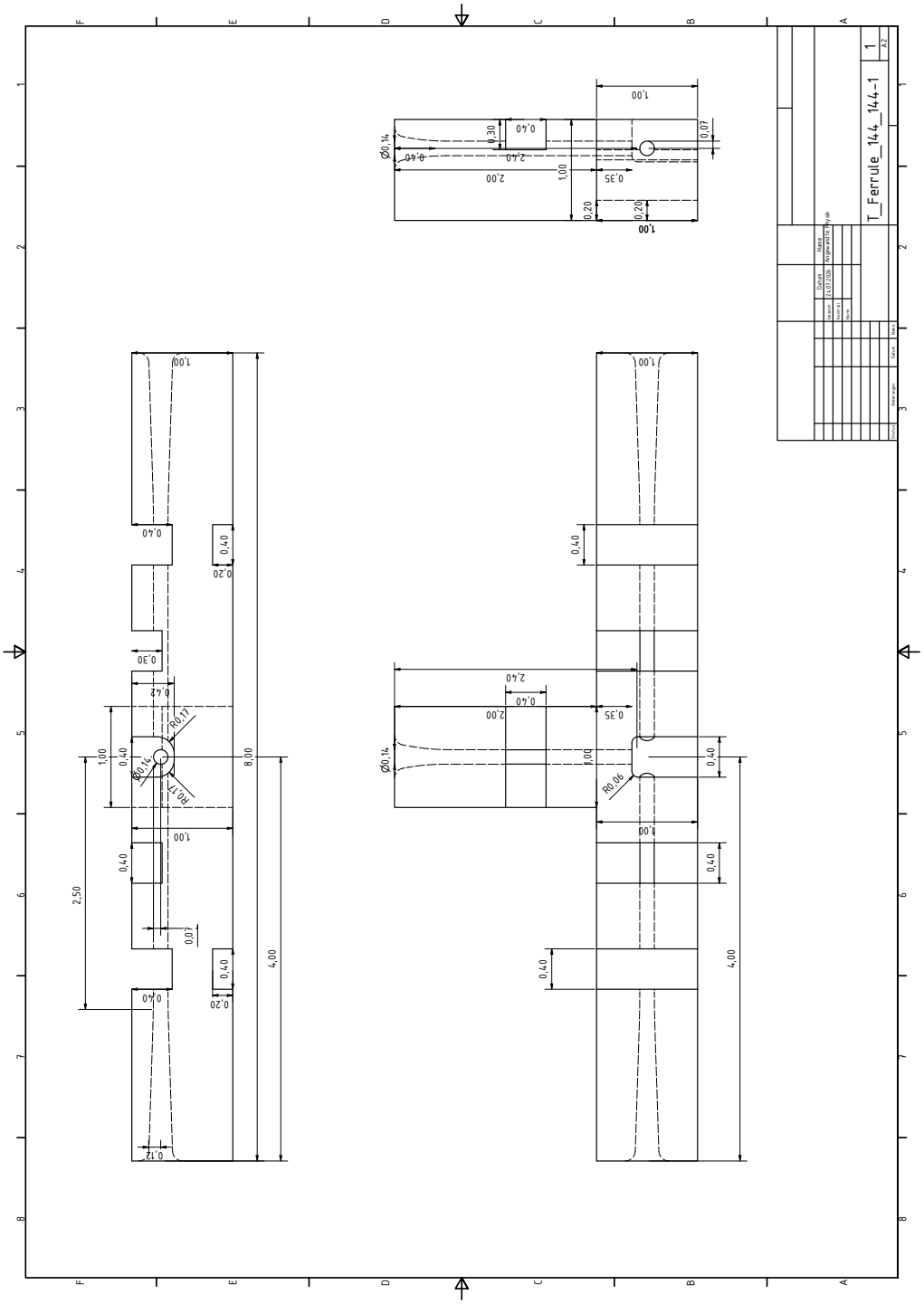


Figure A.7: Engineering drawing of the final three channel T-shaped ferrule including all specific dimensions. Each cavity axis channel extends 4 mm from the central cavity region, while the pump-fiber channel extends 3 mm. The two cavity channels have a diameter of 154 µm, while the pump-fiber channel has a diameter of 144 µm. The channels are supported by printed arms with a cross section of 1 mm × 1 mm and include 0.4 mm-wide openings to improve flushing. The pump-fiber channel extends further into the central cavity region, terminating at a distance of 0.15 mm from the central cavity point, compared with 0.2 mm for the cavity channels. Detailed dimensions are provided.

A.5 Beam Profile Centering

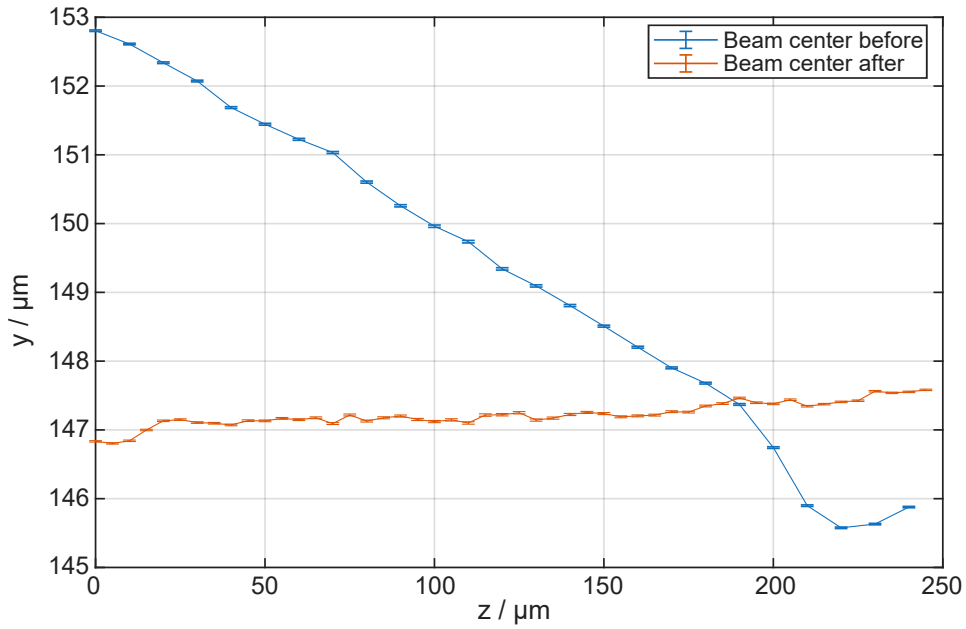


Figure A.8: Evolution of the beam-center position of the three-channel T-shaped ferrule with increasing propagation distance from the cleaved fiber facet from which the beam is emitted. The blue trajectory corresponds to a relative angle of $(1.588 \pm 0.004)^\circ$ between the beam-center trajectory and the optical axis of the beam profiler. The orange trajectory corresponds to the optimized tilt setting of the platform, for which the relative angle is reduced to $(-0.171 \pm 0.004)^\circ$. This optimized setting was used for the subsequent measurement.

A.6 Crossed FFPCs for CQED

A symmetric cavity with $R = 40\,\mu\text{m}$, $L = 60\,\mu\text{m}$, and a finesse of $\mathcal{F} = 1.5 \times 10^5$ can be considered for the D_2 transition of ^{87}Rb near 780 nm. These parameters correspond to a mode waist of approximately 2.1 µm after Equation 2.3. For this cavity, the intensity linewidth is approximately $\Delta\nu_{\text{FWHM}} = 16.7\,\text{MHz}$, corresponding to a cavity-field decay rate of $\kappa/2\pi = \Delta\nu_{\text{FWHM}}/2 \approx 8.3\,\text{MHz}$ [12]. Using the ideal single-atom cooperativity, an idealized value of approximately [12]

$$C = \frac{\sigma}{\pi w_0^2}\mathcal{F} \approx 3.2 \times 10^3$$

is obtained.

Using

$$C = \frac{g^2}{2\kappa\gamma},$$

together with $\gamma/2\pi \approx 3.0\,\text{MHz}$ [89] and a cavity-field decay rate [12] of $\kappa/2\pi \approx 8.3\,\text{MHz}$, this corresponds to an ideal atom–cavity coupling strength of approximately $g/(2\pi) \approx 400\,\text{MHz}$.

Under these idealized conditions, the resulting hierarchy $g \gg \kappa, \gamma$ therefore lies well within the strong-coupling regime. This value should be understood as an idealized estimate, since the experimentally

achieved coupling additionally depends on the atomic position, dipole orientation, spatial mode overlap, and the selected atomic transition.

Acknowledgements

First of all, I would like to thank Sebastian and Hannes for giving me the opportunity to work on this project during my Master's thesis. I already enjoyed working on this topic during my Bachelor's thesis, but throughout my Master's thesis this grew even further. I especially valued the freedom to develop my own ideas and the support I received in exploring and applying them. This made it possible for me to dive deeply into the topic and become genuinely passionate about it, even beyond the scope of this thesis. I am already looking forward to the next planned measurements!

I would also like to thank Prof. Stefan Linden, not only for agreeing to be my second supervisor for both my Bachelor's and Master's theses, but also for allowing me to use the various experimental systems available in his labs. In this context, I would also like to thank Paul for showing me how to use the different systems and for always helping when needed.

I would like to thank Wolfgang and Hannes for their valuable input and for helping me understand many aspects of the project in much greater detail.

I also want to thank all members of NQO for the great times at conferences, during Feierabendbier & table tennis, and many other activities, as well as Daniil for providing the best shelter during the hot, and later colder, days.

Lastly, I would like to thank all members of the FCO lab, Lukas, Daniel, Florian, and Julia, who made every moment, whether good or bad, as enjoyable as it could possibly be, both within and outside the context of physics.